

# Warming of Greenland Sea Deep Water Induced by Abyssal Mixing

Vom Fachbereich für Physik und Elektrotechnik  
der Universität Bremen

zur Erlangung des akademischen Grades

Doktor der Naturwissenschaften (Dr. rer. nat.)

genehmigte Dissertation

von

Dipl. Oz. Maren Walter  
aus Ströhen (Hann.)

1. Gutachter: Prof. Dr. M. Rhein  
2. Gutachter: Prof. Dr. D. Olbers

Eingereicht am: 11.12.2003  
Tag des Promotionskolloquiums: 04.02.2004



## ZUSAMMENFASSUNG

Während der 1980er und 90er Jahre, als keine tiefreichende Konvektion in der Grönlandsee stattfand, wurde eine langsame aber signifikante Erwärmung des Tiefenwassers der Grönlandsee beobachtet. Die Änderungen der Tiefenwassereigenschaften können durch erhöhte vertikale Vermischung erklärt werden, allerdings sind die dafür benötigten Vermischungsraten am oberen Ende der Spanne bisheriger Beobachtungen in anderen Ozeangebieten anzusetzen. Ziel der vorliegenden Arbeit ist es daher, die Stärke der diapyrnischen Vermischung in der Grönlandsee an Hand von Beobachtungen zu bestimmen.

Als Maß für die Vermischung wird die Stärke und räumliche Verteilung des vertikalen Austauschkoeffizienten untersucht. Die Berechnung erfolgt über die Energiedissipationsrate, die wiederum durch zwei verschiedene Methoden bestimmt wird. Aus Instabilitäten in Profilen der Dichte werden Thorpe Skalen berechnet, welche auf Grund ihres linearen Zusammenhanges mit der Ozmidov Skala eine direkte Bestimmung der Dissipation ermöglichen. Als zweiter Ansatz werden stellvertretend für den Energiegehalt des internen Wellenfeldes spektral die Varianzen der vertikalen Scherung der horizontalen Geschwindigkeit und der Dehnung des Dichtefeldes berechnet, und daraus die Gleichgewichtsdissipationsrate bestimmt. Die verwendeten Daten stammen von einer *FS Polarstern* Expedition im Sommer 1998, und umfassen Strömungsmessungen aus der zentralen Grönlandsee und den umgebenden untermeerischen Rückensystemen mittels eines gefierten akustischen Doppler Profilstrommessers (LADCP) sowie ergänzende Temperatur- und Salzgehaltmessungen.

Die so berechneten Austauschkoeffizienten sind hoch genug, um die beobachteten Trends im Tiefenwasser verursacht zu haben. Der mittlere Austauschkoeffizient in 2000 m Tiefe beträgt  $K_\rho = 1.2 \times 10^{-3} \text{ m}^2 \text{ s}^{-1}$ , zwei Größenordnungen über typischen Werten für den tiefen Ozean. Die höchsten Werte treten im tiefen Becken auf; in mittleren Tiefen ist ein leichter Anstieg in der Nähe rauher Topographie zu beobachten. In der Oberflächenschicht finden sich die höchsten Koeffizienten an den Fronten der Randströme. Erhöhte Vermischung in der Tiefe wird nicht nur nahe rauher Topographie, sondern im gesamten Becken beobachtet. Da die kritischen Breiten der meisten halbtägigen Gezeiten in der Grönlandsee liegen, kann diese Verteilung als Resultat des Zusammenbruches der Gezeitenwellen auf Grund von Resonanz interpretiert werden. In den tiefsten Becken der Grönlandsee führt die Annahme einer konstanten Vermischungseffizienz trotz schwacher Ausgangsschichtung zu einem unrealistisch hohen Anstieg des Austauschkoeffizienten.



## ABSTRACT

In the absence of deep convection, the Greenland Sea Deep Water has experienced a slow but significant warming during the 1980s and '90s. Enhanced vertical mixing can explain the observed trends of several properties including anthropogenic tracers, but the necessary mixing rates are at the higher end of those observed elsewhere in the ocean. The aim of this work is to use observations to quantify the strength of diapycnal mixing in the Greenland Sea.

The mixing is studied by means of the spatial distribution and strength of eddy diffusivities. These are calculated from energy dissipation rates, which in turn are estimated with two complementary methods. Thorpe scales, which are determined from overturns in density profiles are linearly related to the Ozmidov scale, and therefore provide a direct estimate of the dissipation. The second method uses a spectral estimate of the variances of the vertical shear of the horizontal velocity and the strain of the density field as proxies for the energy content of the internal wave field, and the equilibrium energy dissipation rate. Both methods are applied on a data set obtained during a *FS Polarstern* cruise in summer 1998, comprising lowered Acoustic Doppler Current Profiler (LADCP) measurements of the velocity field in the central Greenland Sea and near the surrounding ridge systems, as well as supplementary temperature and salinity measurements.

The diapycnal diffusivities observed in the Greenland Sea are high enough to account for the changes in deep water. The mean diffusivity across the 2000 m isobath is  $K_\rho = 1.2 \times 10^{-3} \text{ m}^2 \text{ s}^{-1}$ , which is two orders of magnitude larger than the typical deep ocean background. The highest values occur in the deep basin, with a moderate amplification in the vicinity of rough topography at mid depth. In the upper layer, the locations of strongest mixing are close to the fronts of the boundary currents. Enhanced mixing in the deeper layers is not confined to rough topography, but occurs throughout the whole basin. The critical latitudes of most semidiurnal tides are located in the Greenland Sea, therefore this distribution is interpreted as a result of the resonant breakdown of the tidal waves. In the deepest parts of the Greenland Basin, the assumption of a constant mixing efficiency in spite of weak initial stratification leads to an unrealistic strong increase of the diapycnal diffusivities.



## CONTENTS

|   |    |
|---|----|
| <i>Introduction</i> . . . . .                         | 1  |
| <i>1. The Greenland Sea</i> . . . . .                 | 5  |
| 1.1 Bathymetry . . . . .                              | 5  |
| 1.2 Hydrography & Circulation . . . . .               | 6  |
| 1.3 Deep Water Formation . . . . .                    | 13 |
| 1.3.1 The Warming of the Deep Greenland Sea . . . . . | 13 |
| 1.3.2 Models for Deep Water Renewal . . . . .         | 16 |
| <i>2. Mixing and Internal Waves</i> . . . . .         | 21 |
| 2.1 The Internal Wave Field . . . . .                 | 22 |
| 2.2 Finescale Parameterizations . . . . .             | 26 |
| 2.3 Observational Methods . . . . .                   | 29 |
| <i>3. Data</i> . . . . .                              | 31 |
| 3.1 LADCP . . . . .                                   | 31 |
| 3.2 CTD and Bottle Data . . . . .                     | 34 |
| 3.3 Moorings . . . . .                                | 34 |
| <i>4. Mixing in the Greenland Sea</i> . . . . .       | 37 |
| 4.1 Topography . . . . .                              | 37 |
| 4.2 Stratification . . . . .                          | 38 |
| 4.3 Richardson Numbers . . . . .                      | 40 |
| 4.4 Density Inversions and Thorpe Scales . . . . .    | 42 |
| 4.5 Shear Calculated from ADCP Measurements . . . . . | 49 |
| 4.5.1 Processing of the Lowered ADCP Data . . . . .   | 49 |
| 4.5.2 Shear Spectra . . . . .                         | 54 |
| 4.5.3 Shear Variances $\langle S^2 \rangle$ . . . . . | 59 |
| 4.6 Shear/Strain Ratios . . . . .                     | 68 |
| 4.6.1 Strain Spectra . . . . .                        | 68 |
| 4.6.2 Ratios . . . . .                                | 73 |

|       |   |     |
|-------|---|-----|
| 4.7   | Dissipation and Turbulent Diffusivity . . . . .                               | 76  |
| 4.7.1 | Dissipation Estimates from Shear Variances & Inferred Diffusivities . . . . . | 76  |
| 4.7.2 | Spatial Variability . . . . .   | 78  |
| 5.    | <i>Discussion</i> . . . . .   | 93  |
| 5.1   | The Role of Vertical Mixing in Deep Water Formation . . . . .                 | 93  |
| 5.2   | Sources and Distribution of Energy . . . . .                                  | 103 |
| 6.    | <i>Summary and Conclusions</i> . . . . .                                      | 111 |
|       | <i>Appendix</i> . . . . .   | 115 |
| A.    | <i>The Garrett and Munk Spectrum of Internal Waves</i> . . . . .              | 117 |
| B.    | <i>List of Abbreviations</i> . . . . .  | 121 |
|       | <i>Bibliography</i> . . . . .   | 123 |

## INTRODUCTION

*“The formation of cold, heavy bottom-water was here (75°N, 0°) directly observed on the very sea-surface.”*

*“The question of the process of its formation is thus finally settled beyond all doubt.”*

— Helland-Hansen and Nansen (1909), THE NORWEGIAN SEA

The polar oceans have been the object of scientific curiosity since the early days of modern oceanography. From the second half of the 19th century onwards, several expeditions have been carried out with the Nordic Seas as a destination. The pioneering work of those early explorers allowed Helland-Hansen and Nansen (1909) to compile a first description of the current system and water masses of that area, including maps of the surface circulation and the above cited comment concerning the deep water formation in the part of the Nordic Seas which is nowadays commonly referred to as the Greenland Sea. The assumption that gelid surface waters in the polar regions may get dense enough during winter to sink into the interior and form deep and bottom waters was already hypothesised some years earlier (e.g. Nansen, 1906) on grounds of the observed water mass properties. This process, termed open ocean convection, was for a long time thought to be the only direct way of deep water formation affecting the characteristics of the abyssal waters in the Nordic Seas. That hypothesis was questioned when the first winter observations from the area gave no proof of the existence of homogeneous water columns (Metcalf, 1955), and double diffusion came into consideration as additional possible formation process (Carmack and Aagaard, 1973; Clarke et al., 1990).

The incorporation of transient and radioactive tracers in oceanographic research in the 1970s allowed for the first time to study the ventilation and formation processes of deep water directly, because it was now possible to track the paths of water parcels from surface contact down to the abyss by their tracer content, and to thus determine ventilation timescales. From the observational programmes in the Greenland Sea, two results emerged: Firstly, open ocean convection was the major ventilation mechanism for the deep water during the first half of the twentieth century (Peterson and Rooth, 1976). But, and that was the surprising new discovery, the deep water renewal by deep convection had ceased since the end of the 1970s (Rhein, 1991; Schlosser et al., 1991).

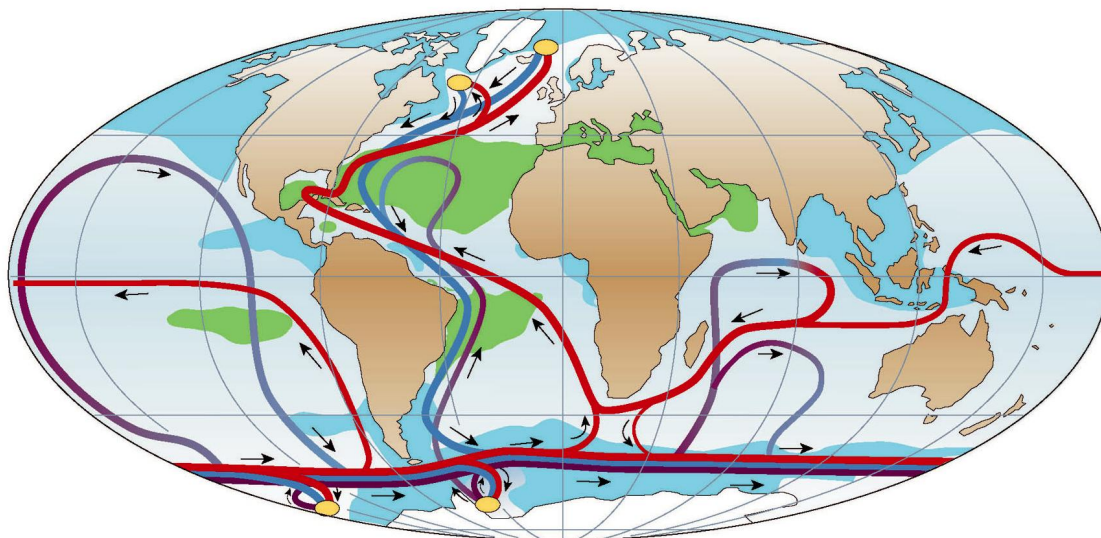


*Fig. 1.0:* Schematic sketch of the global thermohaline circulation (THC, Figure taken from Rahmstorf, 2002). Regions of deep water formation are indicated by yellow circles; the different branches of the THC are colour coded according to their temperature: the warm surface water is marked in red, deep water in blue and bottom water in purple.

Instead, the deep and bottom waters of the Greenland Sea had experienced a small but significant increase in temperature, salinity, and concentration of man-made tracers like CFCs from then on (Bönisch et al., 1997). Since the increase in tracer concentration excludes lateral advection from the adjacent basins (which are less well ventilated than the Greenland Sea) as the dominant source of the alterations, the changes had to involve vertical exchange with the overlying intermediate water masses. The evolution of the parameters (especially the decrease of density at any given isobath) contradict a ventilation by deep convection or double diffusion, but point towards an amplification of turbulent mixing in the basin as the main cause of the observed changes (Visbeck and Rhein, 2000).

Munk (1966) attempted a first estimate of the strength of turbulent vertical mixing with the use of a one-dimensional advection-diffusion balance applied to measured profiles of several parameters. The eddy diffusivity he came up with ( $\approx 1 \times 10^{-4} \text{ m}^2 \text{ s}^{-1}$ ) represented a mean for a steady state ocean. Still, actual measurements in the interior of the ocean failed to confirm this finding; the measured eddy diffusivities were typically an order of magnitude smaller than predicted (e.g. Ledwell et al., 1993; Kunze and Sanford, 1996). This apparent gap was bridged when large-scale experiments revealed areas of elevated mixing close to rough submarine topography like the Mid-Atlantic Ridge (Polzin et al., 1997). The existence of mixing hot spots linked to topography together with boundary mixing may suffice to close the energy balance of the ocean and maintain the stratification by horizontal advection (Munk and Wunsch, 1998). A significant energy source of such an elevated mixing in the abyss is thought to be tidal: internal tides excited at the

rough topography transfer their energy via breaking of internal waves into the small scale turbulent stirring.

The observational data base of mixing rates is still small, but has expanded in recent years. Namely since the magnitude of thermal dissipation and turbulent diffusivity has been linked to finescale properties of the water like vertical shear of velocity and strain of the density field (Gregg, 1989; Polzin et al., 1995), measuring diapycnal mixing is no longer confined to dye and tracer release experiments or high-end microstructure profilers, but can be attempted with more standard shipboard equipment, for example with Conductivity Temperature Depth probes (e.g. Ferron et al., 1998) or finescale-corrected Lowered Acoustic Doppler Current Profilers (Polzin et al., 2002).

The role of diapycnal mixing in the ocean's circulation in general is still poorly understood. The concepts underlying our grasp of the deep ocean flow field imply a uniform distribution of the vertical velocity (Stommel and Arons, 1960). In a steady state ocean, this would require an equally uniform distribution of mixing coefficients, which is not consistent with the observations. Yet, state of the art ocean and climate models operate with very simplified distributions of vertical mixing or even assume a constant mixing rate everywhere in the ocean interior. The intensification of turbulent mixing at the ocean boundaries and the existence of hot spots may have significant impact of the strength and location of the meridional overturning circulation in the world ocean (Marotzke, 1997; Samelson, 1998; Hasumi and Sugimoto, 1999). It is therefore highly desirable to implement accurate vertical and horizontal distributions of mixing coefficients to improve the representation of the thermohaline circulation in climate models.

The Greenland Sea as part of the Nordic Seas plays an important role in the global thermohaline circulation. It is one of the few areas in the world ocean where deep water formation takes place (Figure 1.0). The densification of the formerly warm water masses in the Nordic Seas and Arctic Ocean occurs partly by events intermittent in space and time (like open ocean convection), and partly by slower, continuing heat loss (Mauritzen, 1996b). The newly formed dense intermediate water masses leave the Arctic domain via several overflows across the Greenland-Iceland-Scotland Ridge to form the densest, coolest parts of the North Atlantic Deep Water. While the deep and bottom water masses of the Greenland Sea are not directly involved in the meridional overturning circulation, it is nevertheless important to understand the mechanisms which govern the processes in the Nordic Seas: The overall decrease of density in the Greenland Sea Gyre may lead to an alteration of the density of the water masses crossing the overflows, and in consequence reduce the equilibrium depth of those water masses downstream. There is evidence from modeling that a significant lowered density may weaken or even cause a total breakdown of the thermohaline circulation by inhibited open ocean convection and/or altered freshwater fluxes in a modified hydrographic regime (Delworth et al., 1993, 1997; Otterå et al., 2003).

The interest in diapycnal mixing in the Greenland Sea is therefore twofold: On the one hand, it is important to understand and quantify the processes which are responsible for the deep water

modifications in the Greenland Sea Gyre with regard to the impact on the properties of the water masses of the Atlantic and the effect on the global thermohaline circulation; on the other hand is the Greenland Sea a good “laboratory” for a better understanding of mixing processes in general in the ocean because of its isolation in terms of horizontal exchange with the surrounding abyssal basins. The scope of the study presented here is to derive a picture of the vertical and horizontal distribution of diapycnal mixing in the Greenland Sea Gyre and to quantify its effect on the water mass structure of the gyre, especially the properties of the Greenland Sea Deep Water. It employs hydrographic measurements from Conductivity Temperature Depth (CTD) probes and Lowered Acoustic Doppler Current Profilers (LADCP) to infer the dissipation rates and turbulent diffusivities from finestructure profiles of temperature, salinity and horizontal velocity. The work is organised as follows:

A general overview over the bathymetric and hydrographic conditions in the Greenland Sea is given in Chapter 1, and the different conceptual models for deep water production are presented and discussed. In Chapter 2, the parameterisations for turbulent mixing, their theoretical background and their application in deep ocean environments are described. Chapter 3 introduces the different data used in this study and deals with their accuracy. The strength of the turbulent mixing and its spatial variability as derived from hydrographic data with different methods is presented in Chapter 4. The causes and implications of those distributions and their role in the modification and ventilation of the deep and bottom waters are discussed in Chapter 5. Finally, the results and future prospects are summarised in Chapter 6.

## 1. THE GREENLAND SEA

### *1.1 Bathymetry*

The Greenland Sea forms together with the Iceland, Norwegian and Barents Seas the Arctic Mediterranean Sea (Sverdrup et al., 1942), also referred to as the Nordic Seas (Hurdle, 1986). Itself, it is situated between 70° and 80°N and 15°W and 10°E, covering an area of approximately  $1.2 \times 10^6 \text{ km}^2$  (Figure 1.1).

It consists of two major basins, divided by the Greenland Fracture Zone. The Greenland Basin in the south is the larger and almost bowl-shaped, with a diameter of approximately 400 km. Northward follows the shallower Boreas Basin, which covers only a quarter of the horizontal extent of the Greenland Basin. The eastern boundary of the Boreas Basin is formed by another oceanic ridge, the Knipovitch Ridge. Between the Knipovitch Ridge and the Svalbard shelf there is a small, deep trench, in the following referred to as the Deep Eastern Basin, which is a northward extension of the Lofoten Basin, and therefore part of the Norwegian Sea. The maximum depth of the Greenland Sea of about 3800 m is reached in the Greenland Basin. The Boreas and the Deep Eastern Basins have a depth of 3200 m and 3500 m, respectively.

The Greenland Sea is confined by the Greenland continental shelf to the west and Svalbard and the Siberian shelf with the Barents Sea to the east. The northern passage to the Arctic Ocean is the Fram Strait, with a maximum sill depth of 2600 m. The island of Jan Mayen and the Jan Mayen Fracture Zone separate the Greenland Sea from the Iceland Sea in the south. The Mohns Ridge in the southeast is the boundary between the Greenland Basin and the Lofoten Basin. The sill depths towards the Iceland and Norwegian Seas are approximately 2200 m and 2000 m, respectively.

These sill depths, especially towards the Norwegian Sea, are not well-established, because of the highly variable topography of that area: There are numerous oceanic ridge systems and fracture zones, which are northward extensions of the Mid Atlantic Ridge and constitute the most outstanding bathymetric features in the Nordic Seas. These ridges are characterised by steep topography, deep gaps and narrow trenches, and they amount to a large portion of the total area of the sea bed of the Greenland Sea.

In the southeast, there also is a chain of extinct volcanoes, Vesteris Banken, an isolated seamount in the southern part of the Greenland Basin ( $\approx 73^\circ 30' \text{ N}, 9^\circ \text{ W}$ ), being the largest and northernmost. It rises from the ground depth of 3000 m to 600 m below the surface.

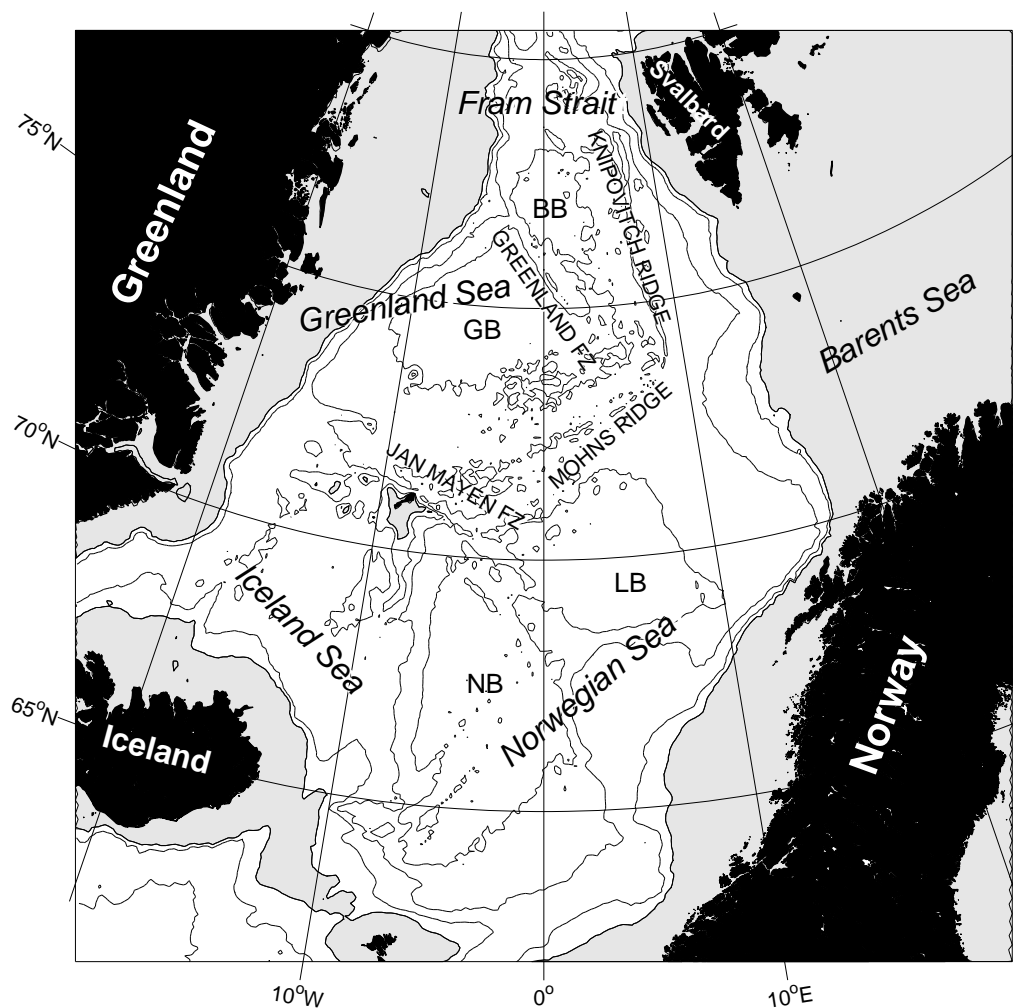


Fig. 1.1: Topographic map and names of the Greenland Sea area. Oceanic basins are denoted by the following abbreviations: BB for Boreas Basin, GB for Greenland Basin, LB for Lofoten Basin and NB for Norwegian Basin. Depths shallower than 500 m are shaded. Topographic data set is ETOPO-2 (IBCAO, 2000; National Geophysical Data Center, 2001).

## 1.2 Hydrography & Circulation

To cite Swift and Aagaard (1981), “*The water mass terminology for the entire area is rich and often confusing*”. However, in the following a short overview over the general hydrography and the main water masses in the Greenland Sea will be given. The ranges given for temperature and salinity are based on the literature (e.g. Carmack and Aagaard, 1973; Swift and Aagaard, 1981; Aagaard et al., 1985).

Since especially the deep water properties are subject to ongoing changes, adjustments have been made to fit the current conditions. Namely for the Greenland Sea Deep Water (GSDW), the

|                           | Temperature [°C]      | Salinity            |
|---------------------------|-----------------------|---------------------|
| Polar Water               | $\theta < 0.0$        | $S < 34.4$          |
| Atlantic Water            | $\theta > 3.0$        | $S > 34.9$          |
| Return Atlantic Water     | $\theta > 0.0$        | $34.9 < S < 35.0$   |
| Arctic Intermediate Water | $2.0 > \theta > -1.0$ | $34.7 < S < 34.9$   |
| Greenland Sea Deep Water  | $\theta > -0.9$       | $34.88 < S < 34.91$ |
| Eurasian Basin Deep Water | $\theta > -0.9$       | $S > 34.91$         |

Tab. 1.1: Water masses of the Greenland Sea and their  $\theta$ - $S$  properties

temperature range was extended to a higher upper limit compared to the  $-1.2^\circ\text{C}$  of Aagaard et al. (1985), which was a typical value for the GSDW observed before 1990, but is not found anymore in 1998 (cf. Figures 1.2 and 1.7). For an overview of the  $\theta$ - $S$  properties see Table 1.1.

Two hydrographic transects of a recent summer situation (1998, see Chapter 3 for details), one from Fram Strait ( $79^\circ\text{N}$ ) and the other from the central Greenland Sea along  $75^\circ\text{N}$ , are depicted in the Figures 1.2 and 1.3 to illustrate the general conditions.

The water mass properties of the Nordic Seas are closely tied to the current system. Due to weak stratification (and consequential weak horizontal density gradients), currents in subpolar and polar regions are predominantly barotropic. In the Greenland Sea, the circulation is dominated by a mean cyclonic flow on all depth levels (e.g. Clarke et al., 1990). The meridional currents, i.e. the exchange flows between the Arctic Ocean and the North Atlantic, are far more pronounced than the zonal ones (Figure 1.4); especially the East Greenland Current in the west flows with a speed of 20 to 40 cm/s (Figure 1.5, cf. Strass et al., 1993; Woodgate et al., 1999). Direct current measurements show that the mean circulation is often masked by tidal motions and eddylike structures which exhibit velocities of the same order of magnitude (a few cm/s) as the mean flow (Figure 1.5).

#### *Upper Layer (Surface — 1500 m)*

Warm saline water of Atlantic origin enters the Nordic Seas with the Norwegian Atlantic Current (NAC). On  $75^\circ\text{N}$ , it is found between the Barents Sea shelf break and Mohns Ridge from the surface to depths up to 800 m (Figure 1.2). The NAC follows the Norwegian coast and then splits into two branches: one easterly branch which enters the Arctic Ocean via the Barents Sea, and the West Spitsbergen Current. While some of the water of the West Spitsbergen Current recirculates in the Fram Strait, the greater part passes the Fram Strait on the eastern side and proceeds into the Arctic Ocean (e.g. Mauritzen, 1996; cf. Figures 1.2, 1.3).

The southward outflow from the Arctic Ocean is confined to the western margin of the Fram Strait and the Greenland shelf. On the shelf, there is the very cold and fresh Polar Surface Water (PW). The East Greenland Current flows along the shelf slope with a core near the surface. In its upper part it carries a mixture of the Atlantic Water recirculated in Fram Strait and the water masses

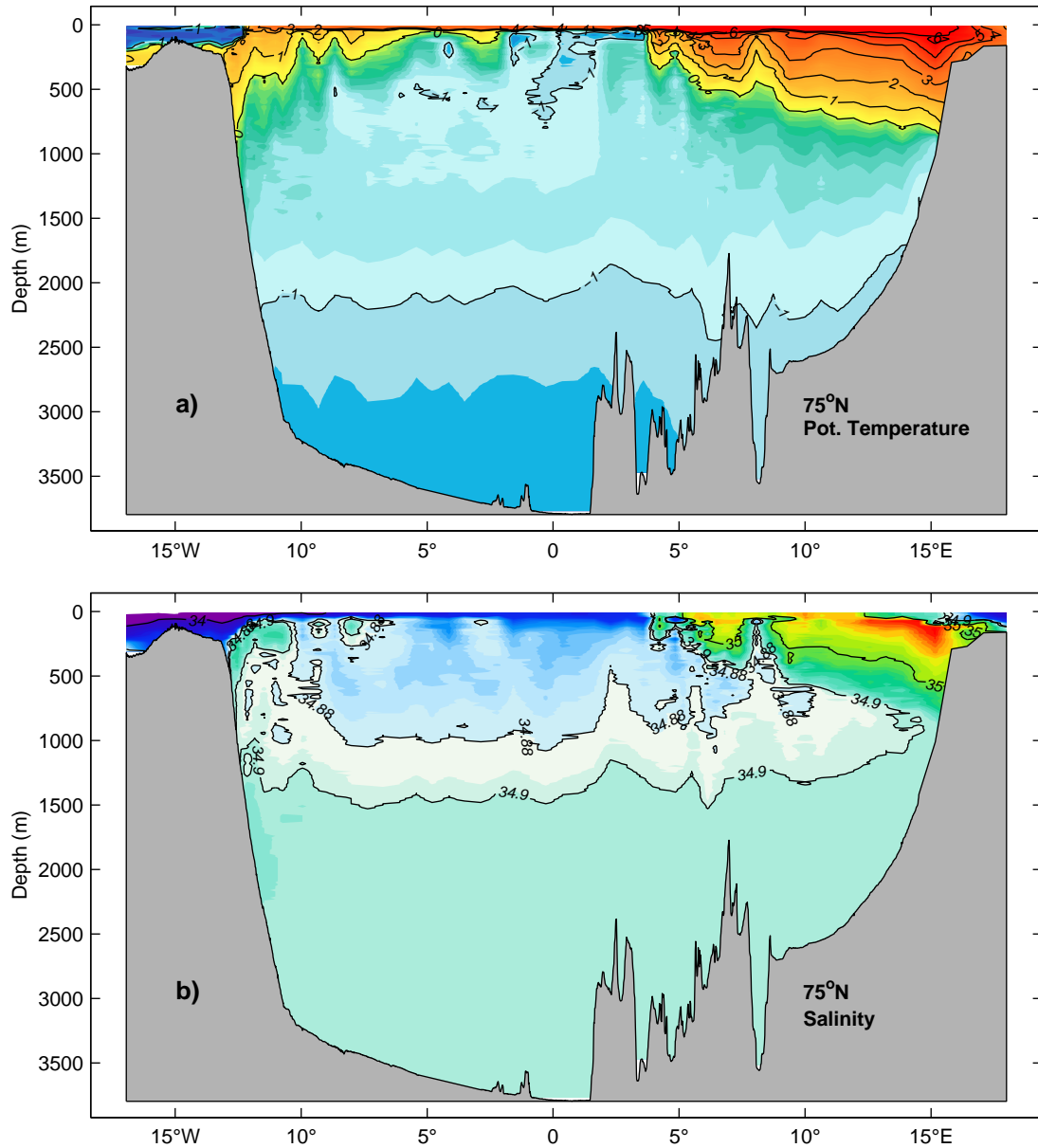
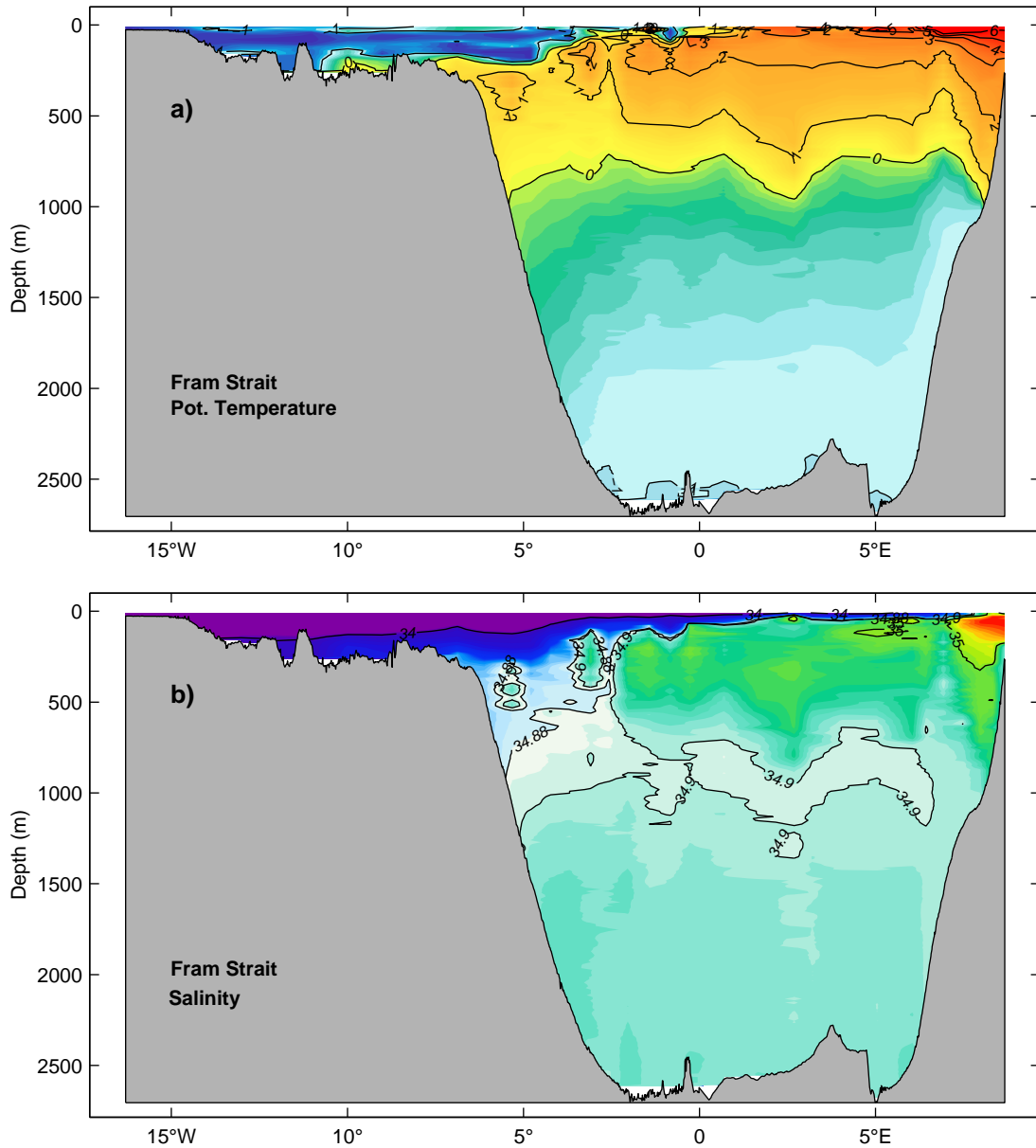


Fig. 1.2: Transect along 75°N crossing the central Greenland Sea (see Figure 3.1 for exact position); shown are:  
a) potential temperature  $\theta$  in °C (contour interval 0.1) and b) salinity (contour interval 0.01). CTD data from *FS Polarstern* cruise ARK XIV/2 (Aug. — Oct. 1998) (Courtesy of E. Fahrbach and G. Budéus).



*Fig. 1.3:* Transect across Fram Strait (approximately 79°N, see Figure 3.1):  
 a) potential temperature  $\theta$  in °C and b) salinity. Contouring intervals and colour range are the same as in Figure 1.2 for the purpose of comparison. CTD data from ARK XIV/2.

of Atlantic origin which have travelled through the Arctic Ocean and experienced cooling from the atmosphere.

This returned Atlantic Water has a history of atmospheric cooling and freshening due to ice melt, precipitation and river runoff, and is therefore slightly colder and fresher than the source water mass (cf. Figures 1.2, 1.3, Table 1.1).

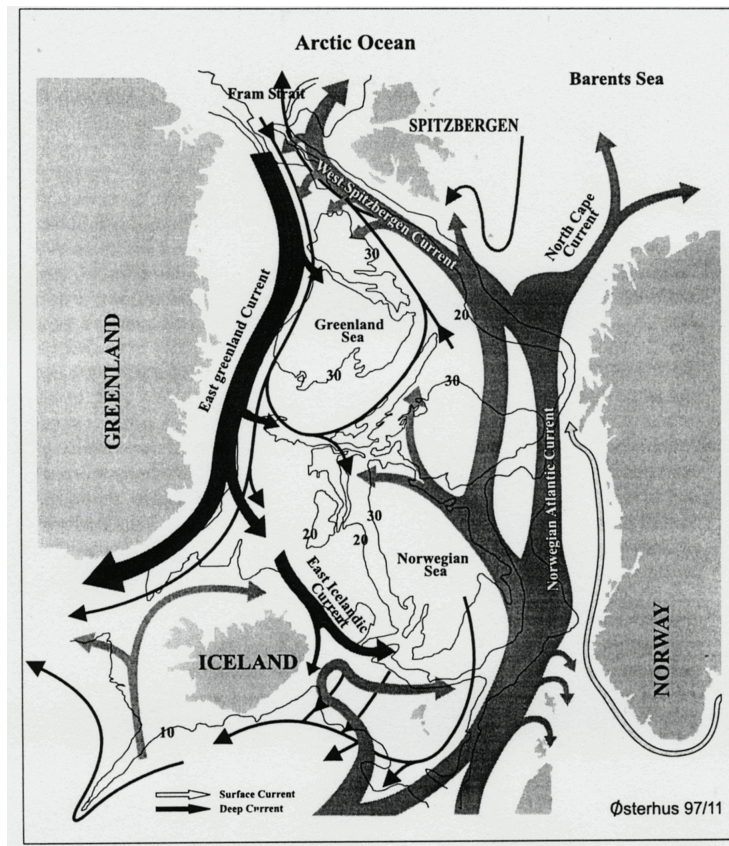


Fig. 1.4: Schematic sketch of the general circulation in the Nordic Seas. Figure by Østerhus, modified from Dickson et al. (1996).

The water in the centre of the Greenland Sea Gyre, away from the boundaries, is affected mainly by convection down to intermediate depth, i.e. cooling and vertical mixing in late winter (Figure 1.6). The resulting water is called Arctic Intermediate Water (AIW). The actual penetration depth of the convection varies from year to year (e.g. Budéus et al., 1998); the vertical extension of this water body is bounded by an intermediate salinity maximum and can thus be identified in the lower panel of Figure 1.2. This salinity maximum is accompanied by a maximum of potential temperature, and stems from a spreading of Atlantic Water towards the interior of the gyre below the newly formed AIW.

#### *Deep Sea (1500 m — Sea Bed)*

Below 1500 m, the central gyre is filled with Greenland Sea Deep Water (GSDW), the coldest and densest water mass of the Nordic Seas, formed by deep-reaching convection. This water mass is very homogeneous in salinity, and weakly stratified by a temperature gradient (Figure 1.2). Historically, it has been reported to have potential temperatures as low as  $-1.3^{\circ}\text{C}$ , but has become

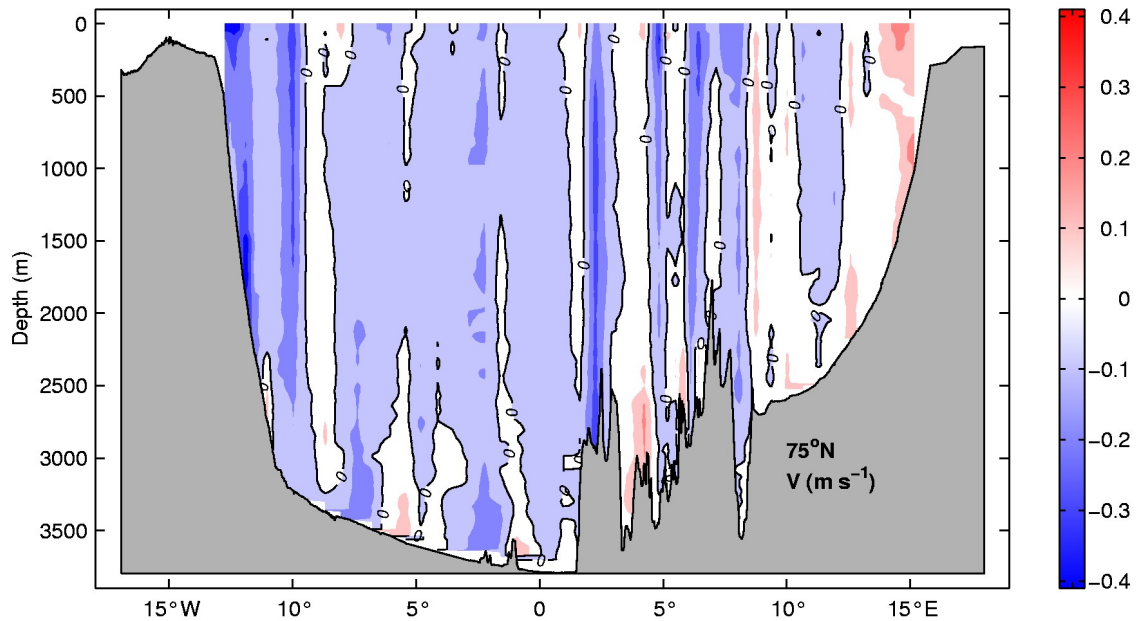


Fig. 1.5: Currents across 75°N (see Figure 3.1 for exact position of transect) from direct measurements with a lowered ADCP; shown is the northward component of flow  $v$  ( $\text{m s}^{-1}$ ) with a contour interval of 0.1. Data from *FS Polarstern* cruise ARK XIV/2 (Aug. — Oct. 1998).

gradually warmer since the late 1970s; in 1998, the coldest part of the GSDW was about  $-1.16^\circ \text{C}$  (Figure 1.6). The warming is discussed in more detail in the next section. With the deeper part of the East Greenland Current, a core of Eurasian Basin Deep Water (EBDW) from the Arctic Ocean flows southward. This core at a density of  $37.44 \leq \sigma_2 \leq 37.45$  carries a higher salinity than the surrounding GSDW, and is easily identified in a  $\theta$ - $S$  diagram (Figure 1.6, inset).

### Exchange Flows

Exchange flows with the Greenland Sea are limited to the North Atlantic (via Norwegian and Iceland Seas) and the Arctic Ocean. While the Fram Strait is deep enough to allow a deep water inflow from the Arctic, the shallower sills in the south practically exclude an effective exchange of deep water with the North Atlantic and isolates the deep basins of the Greenland Sea.

At the surface, the northward flowing West Spitsbergen Current is ultimately a northward extension of the Gulf Stream via the North Atlantic and the Norwegian Atlantic Currents. Direct measurements at the inflow of the NAC between Iceland and Scotland show a total volume transport of 7 Sv ( $1 \text{ Sv} = 10^6 \text{ m}^3/\text{s}$ ), with an associated heat transport of 250 TW and a salt flux of 245 kT/s (for details, see Hansen and Østerhus (2000) and references therein). It is therefore the main source of salt and heat for the Nordic Seas and the Arctic.

Freshwater enters the area mainly from the Arctic via Fram Strait, and is chiefly found on the

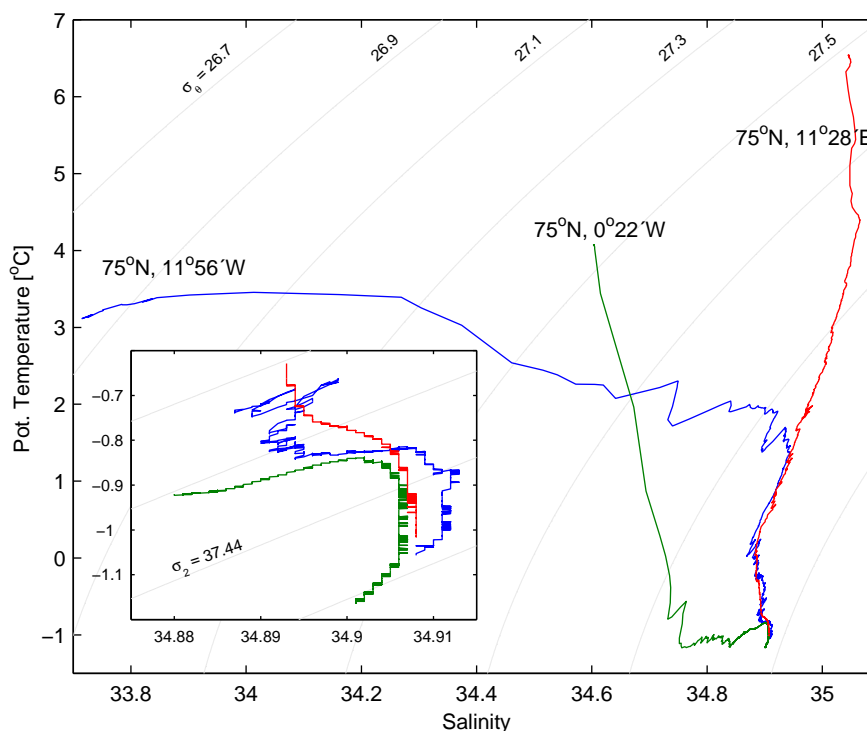


Fig. 1.6:  $\theta$ - $S$  diagram of three profiles along the  $75^\circ\text{N}$  transect (Data from *FS Polarstern* ARK XIV/2, Aug. — Oct. 1998). The easternmost profile (red) shows the highest salinities due to the inflow from the Atlantic. The profile from the Greenland shelf (blue) displays also a significant portion of Return Atlantic Water in intermediate depth, while the influence of low saline polar water masses dominates near the surface. The profile from the central Greenland Sea Gyre (green) has in contrast a substantial water body with relatively low salinities at intermediate depths. This is due to convective activity in this region. In the deep water (inset), the inflow of saline Eurasian Basin Deep Water along the western boundary is clearly visible in the western profile.

Greenland shelf. The East Greenland Current on the Greenland shelf break is flowing southward and feeding the Denmark Strait overflow (Strass et al., 1993; Mauritzen, 1996a), carrying some of this fresh water towards the North Atlantic. The transport associated with the EGC is approximately 3 Sv in Fram Strait (Foldvik et al., 1988) and about the same (2.7 Sv, Dickson et al., 1990) in the Denmark Strait overflow.

Both meridional currents have only limited exchange with the water in the interior of the Greenland Sea Gyre, as was demonstrated by the spreading of a dye ( $SF_6$ ) patch (Watson et al., 1999).

Deep inflow into the Greenland Sea is more or less restricted to the aforementioned EBDW, which enters the Greenland Sea via Fram Strait from the north, with a transport between 0.8 and 2 Sv (Smethie, Jr. et al., 1988; Aagaard et al., 1991). It is at first confined to the East Greenland shelf as the western boundary and subsequently follows the slow cyclonic flow until finally the largest portion of the EBDW leaves the gyre east of Jan Mayen. The remaining rest slowly dilutes

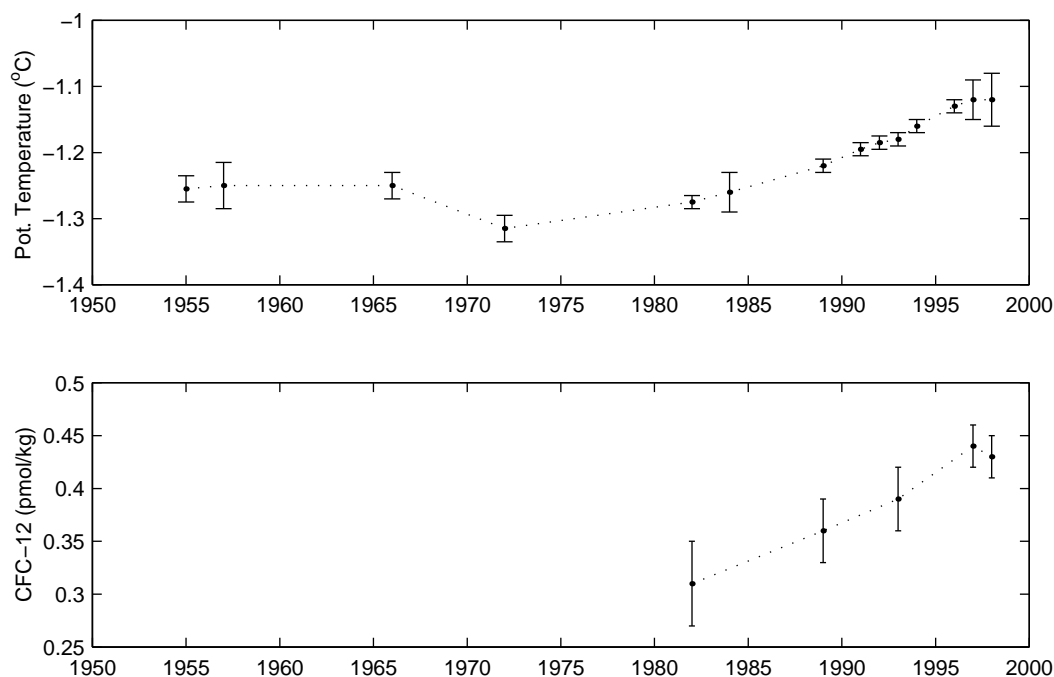


Fig. 1.7: Timeseries of potential temperature  $\theta$  and CFC-12 below 2500 m in the Greenland Sea; the error-bars denote the standard deviation over the included profiles. Figure updated from Visbeck and Rhein (2000).

in the GSDW, partaking in the deep cyclonic flow (Mauritzen, 1996a).

The overflow of GSDW mixed with EBDW spilling over Mohns Ridge through the Jan Mayen Channel (and possibly other, shallower passages) contributes a major part of the source water masses of the Norwegian Sea Deep Water (Aagaard et al., 1985; Rhein, 1991). Likewise, some of the warmer NSDW penetrates into the deep Greenland Basin over the ridges in exchange.

### 1.3 Deep Water Formation

#### 1.3.1 The Warming of the Deep Greenland Sea

Since the early days of research in the north polar regions, the deep water masses of the Greenland Sea are known to be well ventilated (Mohn, 1887; Nansen, 1902, 1906). The apparent homogeneity in temperature and density from the surface to the seabed in those observations led to the concept of deep convection: Vigorous cooling at the surface during winter causes water to sink down; it is then replaced by warmer water from below, which also gets cooled and sinks. This process repeats itself until vertical homogenization is established (e.g. Helland-Hansen and Nansen, 1909).

This convective mixing is most likely to occur in so-called “chimneys”, small regions where

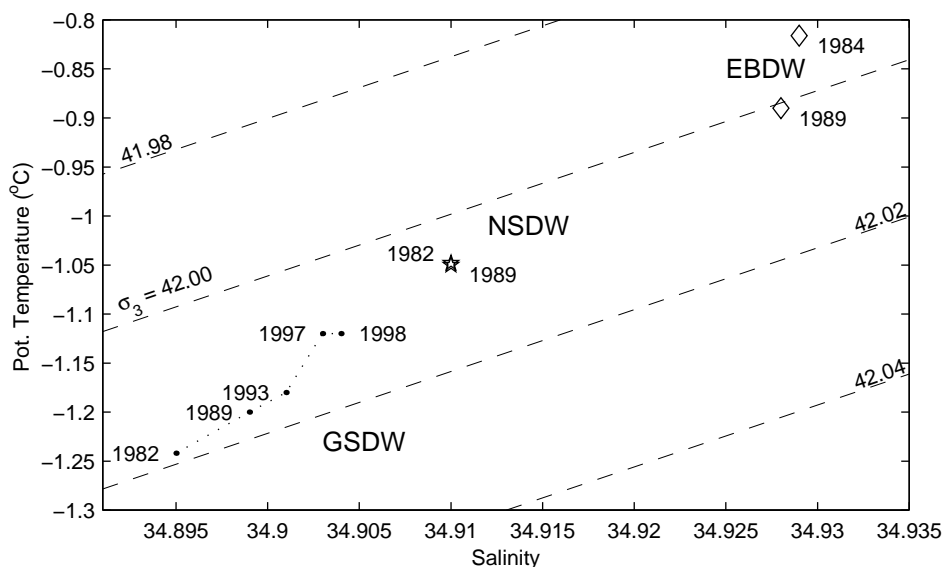


Fig. 1.8:  $\theta$ - $S$  diagram of the temporal development of mean deep water properties. Dots denote Greenland Sea Deep Water, asterisks Norwegian Sea Deep Water and diamonds Eurasian Basin Deep Water. Superimposed are lines of constant potential density relative to 3000 m. Data for Figures 1.8 and 1.9 are taken from: 1982 – Bullister and Weiss (1983); 1984 – Smethie, Jr. et al. (1988); 1989 – Valdivia87, Rhein (1991); 1993 – *Polarstern ARK9/1*, Rhein (1996); 1997 – *Valdivia166*; 1998 – *Polarstern ARK14/2*.

initial weak stratification favours the homogenization. For a larger region like the Greenland Sea, several chimneys are required to account for the ventilation of the entire deep water (Killworth, 1979).

While open-ocean deep convection occurred from time to time in the past (Peterson and Rooth, 1976; Swift and Aagaard, 1981), the presumption that it regularly takes place in the Greenland Sea is questionable. In spite of a growing number of field measurements, bottom-reaching convection was not directly observed up to the present day.

In the 1980s, several investigations showed a change in hydrographic conditions and a reduction of deep water formation (Clarke et al., 1990; Schlosser et al., 1991; Rhein, 1991). Closer inspection of time series of various hydrographic parameters showed different regimes throughout the past couple of decades (Aagaard, 1968; Clarke et al., 1990; Rhein, 1996; Bönisch et al., 1997; Østerhus and Gammelsrød, 1999): There were periods when the water column was relatively homogeneous and cold; this was the case in the late 1960s and the early 1980s. On the other hand, there were extended periods of warming, accompanied with an increase in salinity. Such a period lasted approximately from 1955 to 1965; the recent warming began in the middle of the 1980s (Figure 1.7).

In the period of this warming falls the Greenland Sea Project (GSP), an international programm

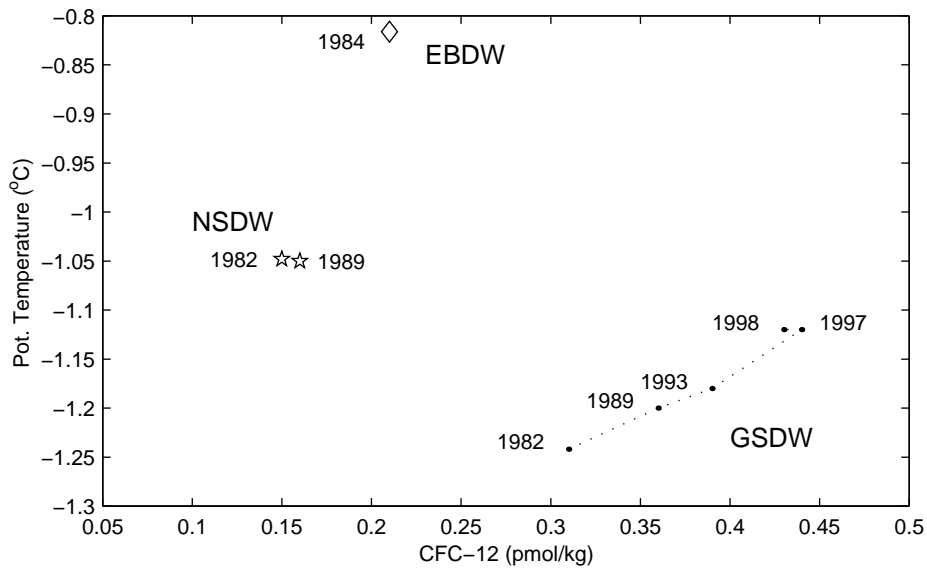


Fig. 1.9: Same as Figure 1.8, for the relation between potential temperature and CFC-12 content in the deep water masses.

aimed at the better understanding of the hydrography, circulation and deep water formation in the Greenland Sea, that lasted from 1987 to 1993 (GSP Group, 1990). The GSP included major field work: high resolution CTD surveys (e.g. Budéus et al., 1993), convection moorings (e.g. Schott et al., 1993; Visbeck et al., 1995) and measurement and analysis of anthropogenic tracers (Rhein, 1991), providing a detailed insight in the evolution of various water mass properties during that time.

Convection was only sporadically observed, and mostly confined to the upper 1000 m of the water column. Occasionally, maximum depth of 2000 m are reached, for example in the winters of 1987/88 and 1988/89 (Rudels, 1990; Pawlowicz et al., 1995). This lack of deep reaching convection means a reduction of heat loss to the atmosphere and therefore a warming of the water column, first in the upper layers and then penetrating downward. Additionally, the total freshwater flux into the ocean is reduced, although the ongoing shallow convection restricts the increase of salinity to the depths below 1500 m. The result of these two effects is a steady decrease in density, a deepening of isopycnals. This again impedes convection, and is therefore a reinforcing feedback.

At the same time, observations of anthropogenic tracers (chlorofluorocarbons (CFCs), helium/tritium and others) show, despite a decline in deep water renewal, that there is still some kind of ventilation beyond the convectively mixed layers (Smethie, Jr. et al., 1986; Bönisch et al., 1997). For example, the concentration of the CFC component CFC-12, which has an increasing input function at the surface since the 1940s, displays an almost linear rise below 1500 m (Figure 1.7).

When only considering density and “classical” hydrographic properties such as temperature

and salinity, the most likely reason for the warming of the deep water seems to be lateral advection of water masses coming from the Norwegian Sea and Eurasian Basin of the Arctic Ocean (Figure 1.8). But, even with having the appropriate  $\theta$ - $S$  properties, the neighbouring basins of the Greenland Sea cannot be solely responsible for changing properties of the deep water: The water bodies of those basins, the NSDW and the EBDW, are even less well ventilated and consequently lower in CFC content (Peterson and Rooth, 1976; Smethie, Jr. et al., 1988). Lateral advection and consecutive mixing would therefore shift the CFC concentrations towards the lower values of EBDW and NSDW. This is clearly not the case (Figure 1.9). While there might be a reasonable contribution of those water masses towards the properties of the Greenland Sea Deep Water (Aagaard et al., 1991), the tracer observations point into a different direction. Intermediate layers, where the water has been in recent contact with the surface, must play some role in the renewal processes of the deep and bottom waters.

### 1.3.2 Models for Deep Water Renewal

#### *Double-Diffusion*

Prompted by the (albeit sparse) data from the warming period in the late 1950s and early 1960s which apparently excluded deep convection as a means of deep water formation, Carmack and Aagaard (1973) were the first to propose an alternative scenario for the deep water renewal. They concluded from observations of density and oxygen content that the formation of deep water takes place without surface interaction. The mechanism invoked for the production of dense water was double-diffusion in the layer of Atlantic Water.

The different turbulent diffusivities for heat and salt could cause a loss of buoyancy to the cooler and fresher water above. While spreading towards the centre of the gyre, the Atlantic layer thus becomes colder, fresher and denser, and gradually sinks. Finally, some sort of sub-surface convection would take place in the centre of the gyre.

The feasibility of this concept was further explored by McDougall (1983), who set up a relatively simple idealised model including a balance between advection of Atlantic Water and double-diffusive convection. His calculations yielded a deep water formation rate in agreement with the value obtained earlier by the volumetric census conducted by Carmack and Aagaard (1973).

The case was revisited by Clarke et al. (1990), when a new and extensive set of winter hydrographic data from the Greenland Sea was available. In addition to temperature and salinity, they considered the distribution and gradients of oxygen. The result was that double diffusion alone is not sufficient to explain the observed patterns in the absence of deep convection, and that there must be at least one other mixing process present.

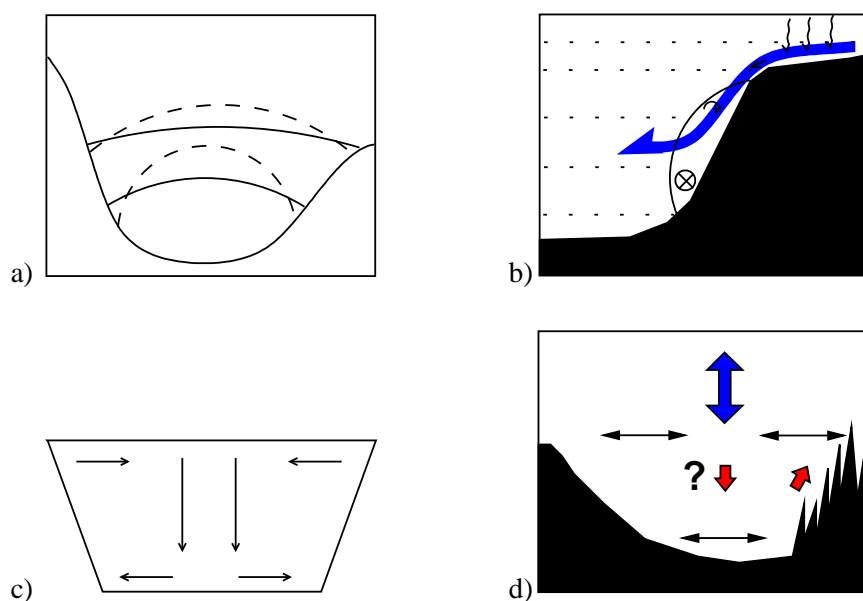


Fig. 1.10: Conceptual sketches of different models for deep water renewal: a) Collapsing dome; b) Slope convection; c) Large-scale downwelling; d) Enhanced turbulent mixing.

Figures adapted from a,b) Meincke and Rudels (1995), c) Budéus et al. (1998) and d) Visbeck and Rhein (2000).

### Dome Collapse

In the following years, a few other processes have been proposed, all of them including the warmer and saltier upper layers of the Greenland Sea. The first was the a so-called “dome collapse” (Figure 1.10a). The barotropic rotation of the Greenland Sea Gyre is forced by the curl of the wind stress, and leads to a geostrophic “doming” in the interior of the gyre.

A weakening of the wind stress curl would result in a reduced cyclonic circulation, and subsequently lead to a flattening of the isopycnal surfaces, i.e. deepening of the isopycnals in the centre of the gyre (Meincke and Rudels, 1995; Dickson et al., 1996). Additionally, this flattening would permit an isopycnal penetration of EBDW from the Fram Strait into the centre of the gyre, leading to a further warming therein (but in consequence also decreasing the CFC content).

While there is some evidence that the wind stress curl weakened during the 1980s –possibly in connection with a positive phase of the North Atlantic Oscillation, Jónsson (1991); Dickson et al. (1996)–, a collapsing dome in accordance with missing convective activity is not apparent in observations, in spite of a considerable number of hydrographic surveys since the early 1980s. Instead, repeated hydrographic surveys along 75°N even reveal warming on isopycnal surfaces (Budéus et al., 1998) and an overall increase in tracer content (Figure 1.7).

Summarizing, it can be said that while some of the observational evidence point towards the larger impact of the warmer and more saline Arctic waters masses on the GSDW properties, the

concept of a “collapsing dome” is not well supported by observations. Furthermore, other effects must counteract the Arctic inflow to produce the observed build-up in anthropogenic tracers.

### *Shelf Convection*

A somewhat different approach is the ventilation by shelf convection. This process is reported to take place in Antarctica in the formation of the Antarctic Bottom Water (e.g. Foster and Carmack, 1976) and also plays a role in the ventilation of deep waters in the Arctic Ocean (Aagaard et al., 1985). Cooling and freezing in winter leads to ice formation on the shelf. During the freezing process, the salt is discharged. The resulting brine forms very cold, saline and therefore dense water masses on the shelves. Occasionally, plumes of this dense water are being swashed over the shelfbreak by tidal currents or storms, and move down the slope like an avalanche. On its way down, a plume increases its volume by entrainment of the less dense surrounding water masses by up to 500%. Through this mixing, it becomes subsequently lighter and finally reaches an equilibrium depth (Figure 1.10b).

The development and subsequent descent of such plumes of dense, saline water have been observed in Storfjorden, at the southern tip of Svalbard (Quadfasel et al., 1988; Schauer, 1995). However, these “Storfjord–Plumes” are steered by topography, and, while mixing with the Norwegian Sea Deep Water east of Knipovich Ridge, they exit through the Fram Strait into the Arctic Ocean and thus take no part in the formation of Greenland Sea Deep Water.

It is still an open question, whether a similar process may take place on the western rim of the Greenland and Boreas Basins, the Greenland shelf. The water on that shelf is relatively fresh, and while there might be formation of denser waters through brine release in winter, the Greenland Sea Deep Water is so dense that the mere enrichment of salt would not yield a sufficient density gain for the shelf water to penetrate into the appropriate depths. An additional modification of the plumes has to be invoked if they should be able to reach greater depths. This modification may be entrainment of sediment whilst moving downslope. Although numerical studies show its possibility as a matter of principle (Fohrmann et al., 1998; Kämpf et al., 1999), observational evidence for this kind of deep water renewal is still lacking.

### *Large-Scale Downwelling*

Another proposed means of deep water ventilation is downward vertical advection, apparent in the mean motion of isotherms in the central Greenland Sea Gyre (Budéus et al. (1998), Figure 1.10c). The observed movement of isotherms is consistent with a vertical transport of 0.6 Sv. Whereas a downward shift of properties in the upper water column is clearly evident, the mechanism behind that shift is still unidentified.

If it were pure advection, the conservation of mass poses a few implications: Firstly, there

should be a horizontal flow at the surface or in shallower depths, to feed the downwelling. Secondly, a compensating flow must also be induced at depth. The second claim is difficult to solve especially in depths of 2500 m or more, since a lateral compensating flow is barred below the sills. The only possible pathway would be an upward flux confined to the bottom boundary layer; however, up to the present date, there is no direct evidence for the existence of such an upward transport. Moreover, the fate and physical impetus of such balancing flows is not satisfactorily resolved.

### *Enhanced Turbulent Mixing*

One of the most straightforward ways to transport heat and other properties downward in the ocean would be turbulent vertical mixing. However, the magnitude of such a diapycnal mixing typically found in the open ocean is with eddy diffusivities of  $K_\rho$  in the order of  $10^{-5} \text{ m}^2 \text{ s}^{-1}$  or below (e.g. Ledwell et al., 1998) far too small to account for the observations in the Greenland Sea.

However, in the 1990s the first observations in the Brazil Basin near the Mid Atlantic Ridge and in the Romanche Fracture Zone showed values of vertical diffusivity which were two to three orders of magnitude higher than typical deep ocean values (e.g. Toole et al., 1996; Polzin et al., 1996; Ferron et al., 1998). This led to the idea that vertical mixing in the ocean may be strongly elevated near and above rough topography, e.g. ridges and fracture zones (Polzin et al., 1997; Ledwell et al., 2000).

Encouraged by these findings, Visbeck and Rhein (2000) presented a conceptual model for the deep water ventilation in the Greenland Sea based on enhanced mixing above topography (Figure 1.10d): The Greenland Sea as a small, bowl-shaped basin, is surrounded by several submarine ridges and fracture zones (see Figure 1.1), and therefore favourable for such topographic induced mixing.

Starting from the tracer tendency equation, the authors employed a one dimensional model of vertical advection and diffusion (neglecting horizontal fluxes) to use the temporal change in deep water temperature, salinity and CFC-12 (cf. Figure 1.7) to derive an estimate for the *average* diapycnal diffusivity required if the difference is solely due to vertical mixing. (Likewise, due to the nature of the balance, it could be attributed to vertical advection as described above, with all the limitations and implications mentioned.)

The corresponding eddy diffusivity between 1500 and 2500 m water depth would amount to  $K_\rho$  of the order  $2 - 3 \times 10^{-3} \text{ m}^2 \text{ s}^{-1}$ . This is two orders of magnitude higher than the typical open ocean values, but not unfeasible in the light of the results cited above. Moreover, if the mixing was confined to a 150 m thick bottom boundary layer, a diffusivity of  $10^{-2} \text{ m}^2 \text{ s}^{-1}$  within this layer would be sufficient to produce the observed temporal evolution.

### *Summary and Conclusions*

All the observations presented in the literature concerning the development of deep water properties lead to the conclusion that the deep Greenland Sea in the absence of deep convection is not in an equilibrium state. Either, such a state does not exist for the present conditions, or it is not yet reached. The decision between the two possibilities would be a task for modelers. The observational challenge is to identify the partaking processes and to determine as accurate as possible the contribution of each towards the observed net result.

The goal of the work presented here is to explore the role and magnitude of turbulent exchanges in the environment, and to quantify the effect of the mixing. The best way to determine the diapycnal diffusivity with field measurements would be either the use of a dye, e.g. a tracer release, for basin wide averages, or microstructure measurements to study the temporal and spatial variability. Lacking this kind of precise information, in this study the eddy diffusivities in the Greenland Sea are determined from standard hydrographic and profiling current measurements, which, while not that accurate, are available from a wide range of locations.

## 2. MIXING AND INTERNAL WAVES

*“One man’s noise is another man’s signal”*

— Garrett and Munk (1975)

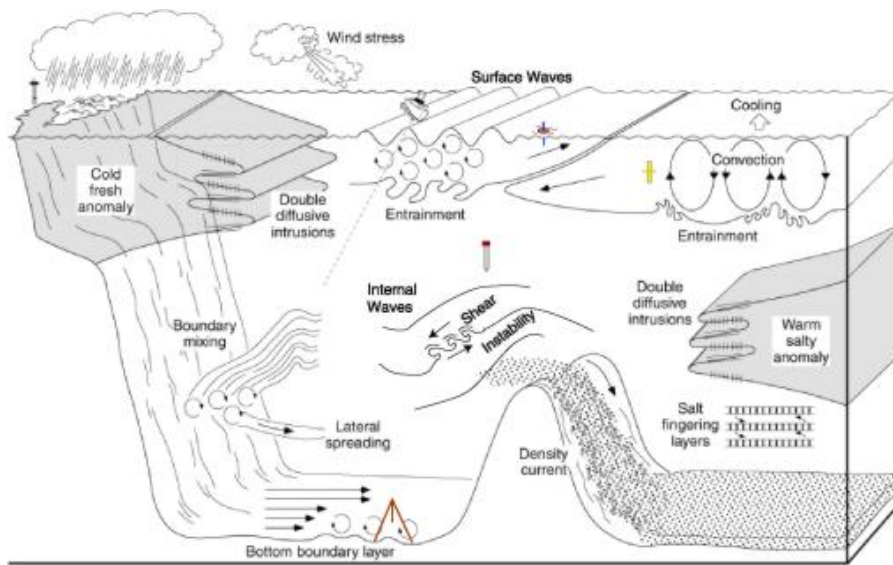


Fig. 2.1: Schematic drawing depicting the various processes which affect mixing in the ocean. Figure taken from the web site of the University of Washington (2002).

Mixing in the ocean occurs on a variety of temporal and spatial scales. It can be divided into boundary and open water processes: Some of the diapycnal fluxes depicted in Figure 2.1 are emanating from the upper boundary or the surface mixed layer, such as small scale turbulence by breaking surface waves or convective mixing. These processes are driven by surface buoyancy fluxes and wind stirring.

Boundary mixing also occurs in the deep ocean in the bottom boundary layer (BBL) at the ocean floor and the lateral rims; the BBL is a turbulent layer comparable to the surface mixed layer, only that the energy source is not the wind, but the ocean currents. Turbulent motion is induced by friction of currents with the roughness of the topography.

Away from the boundaries, cross isopycnal fluxes can be caused by turbulence and or by molec-

ular double diffusive processes. Double diffusion is only of importance in very few areas of the world ocean (for a discussion regarding the Greenland Sea, see Section 1.3); the main source of diapycnal mixing in the deep ocean is thought to be turbulence caused by shear instabilities (e.g. Gregg, 1987).

The mixing in the ocean interior is of a great variability, both in time and space, and therefore difficult to study and not well understood. Molecular diffusivities for salt and heat are so small that they can be neglected compared to turbulent fluxes. The scale of turbulent motions is the so-called microscale with length scales below 1 cm.

Turbulent motion acts in general as a means of ‘creating’ potential energy by extracting kinetic energy from the large scale motions. It counteracts the vertical advection and thus maintains the stratification in the ocean. Without deep mixing, the ongoing sinking of cold dense water in high latitudes would result in a homogeneous cold water pool in the interior of the ocean with a shallow warm surface layer.

Elevated levels of turbulent mixing have been observed to correspond with elevated energy in the vertical shear of the horizontal flow field on the scales from tens to hundreds of meters, the so-called finestructure (Gregg, 1989; Polzin et al., 1995). Oceanic currents and tidal flows constitute the sources which provide the energy required for the mixing in the interior. The energy cascades from large scale motions/currents to smaller features like fronts, eddies and waves, and ultimately to turbulent motions until it finally is dissipated on molecular scales. The link between the different scales are internal waves, which are excited by interaction with the topography at different wavelengths (Bell, 1975), and lose their kinetic energy through instability and breaking to small scale turbulence.

In the following, an overview will be given over the general properties of internal waves and their frequency distribution as described by a parametric model. The mechanisms presumably responsible for the energy transfer towards smaller scales will be briefly introduced. Subsequently, the parameterisations used to estimate turbulent dissipation rates and eddy diffusivities from finescale measurements of velocity (shear) and stratification (strain) will be described and discussed. In the last part of this chapter, the observational techniques available to measure those finestructure properties and their applicability are reviewed.

### 2.1 *The Internal Wave Field*

Internal waves are propagating disturbances in the ocean’s interior, causing simultaneous oscillations in the velocity and density field. They can be viewed analogous to surface waves, in that they are best described in a spectral way, not focussing on single waves. They are visible as vertical and/or horizontal fluctuations in oceanographic records and occur everywhere in the ocean; since they were first recognised by Ekman, they have made the transition from being a mere nuisance to

oceanographers interested in the large scales to a phenomenon of interest in itself.

According to linear theory, internal waves must obey the dispersion relation

$$\frac{N^2(z) - \omega^2}{\omega^2 - f^2} = \left(\frac{\beta}{\alpha}\right)^2 \quad (2.1)$$

where  $\alpha$  and  $\beta$  are the horizontal and vertical wavenumbers, respectively. That is, the waves can only exist if their intrinsic frequency,  $\omega$ , falls in the range between the local Brunt–Väisälä (or buoyancy) frequency,  $N$ , and the Coriolis (or inertial) frequency,  $f$ . This normally means  $f < \omega < N$ , but in high latitudes, where  $f$  is large and the stratification occasionally very weak, sometimes the order is reversed.

The buoyancy frequency is determined by the density gradient as

$$N^2 = -\frac{g}{\bar{\rho}} \frac{\partial \rho}{\partial z}, \quad (2.2)$$

with density  $\rho$  and gravitational acceleration  $g$ , and is a measure for the stability of the stratification. The  $f$ -bounding can be affected by the local vorticity, and is more accurately described by an effective Coriolis frequency,  $f_{eff} = f + \zeta/2$  (Kunze, 1985), where  $\zeta$  is the vertical component of the relative vorticity. The intrinsic frequency of a traveling wave is affected by background shear flow, where it experiences Doppler shift, and gradients in the stratification, which also alter the group velocity.

The scales of internal waves in the horizontal span the range between tens of meters and kilometers, in the vertical they range from meters to a few hundred meters. The group velocity of waves is orthogonal to the wavenumber vector, and the propagation direction dependent on the frequency. The closer the intrinsic frequency of the wave to the local inertial frequency, the more horizontal is the propagation. Waves with frequencies which approach the buoyancy frequency on the other hand propagate more or less vertically. For extensive reviews of properties and behaviour of internal waves in the ocean see, e.g., Thorpe (1975) and Olbers (1983).

A special case are the internal (or baroclinic) tides, which are excited by interaction of the barotropic tidal currents with the topography (Bell, 1975). They have been thought to be of no or little relevance for ocean mixing in the past because of their long wavelengths and low vertical modes, but have recently been identified as the most probable energy source for deep diapycnal mixing (Munk and Wunsch, 1998; Wunsch, 2002; St. Laurent and Garrett, 2002).

### *The Garrett and Munk Model*

The propagation and shape of individual waves depends on their physical environment, namely on the structure of the background flow, and stratification. Despite the large variations of those in space and time, the shape of observed wavenumber/frequency spectra seems to be surprisingly

universal.

This has prompted Garrett and Munk (1972) to develop a semi-empirical model on the basis of linear theory and a fit to existing data which described the energy content of the internal wave field in dependence on frequency and wavenumber. The initial model was later adapted as measurements deemed it necessary (Garrett and Munk, 1975; Cairns and Williams, 1976; Munk, 1981), and in doing so, evolved into a relatively universal description of the oceanic wave field (Levine, 2002), which is commonly referred to as the Garrett-Munk (or GM) model.

Although the GM spectrum represents a synthesis of various independent datasets, most of its detailed features were confirmed by the Internal Wave Experiment (IWEX), a three-dimensional moored array designed to monitor the wave number-frequency spectrum of the internal wave field with a minimum number of assumptions (Briscoe, 1975). The spectral model derived from the IWEX data set by inverse analysis was generally in agreement with the GM model; the main deviations being contamination by finestructure (both for current and temperature spectra) and a spectral peak at low wavenumbers. While the GM formulation turned out to be a rather smooth description of the internal wave field, the main assumptions of horizontal isotropy and vertical symmetry were confirmed except for inertial and tidal frequencies (Müller et al., 1978).

The energy content of the wave field in the GM formulation is dependent on the stratification and therefore allows comparison between data sets from different environments. Of course, there are exceptions from such universality, namely regions of energetic mixing, where the energy content of the spectrum must be elevated compared to a GM spectrum (Gregg, 1989; Polzin et al., 1995).

In the context of this study, the wavenumber spectra of shear and strain are employed in the version of GM76 (Cairns and Williams, 1976). For details of the formulation, see Appendix A.

### *Shear and Strain Spectra*

The vertical wavenumber spectra of shear and of strain (fluctuations of the vertical displacement of isopycnals) are of special interest when calculating turbulent diffusivities on the grounds of density and velocity finestructure measurements.

The general shape of the power spectrum of the vertical shear of the horizontal velocity in the ocean as composed from several microstructure measurements (Garrett et al., 1981) is schematically depicted in Figure 2.2:

At vertical wavenumbers larger than a cutoff of approximately 10 m, the spectrum is dominated by internal wave motions and essentially white. For wavenumbers in the range between 10 m and  $10^{-2}$  m, the finestructure, it shows a linear drop inverse with wavenumber, the “roll-off range”. In the microstructure range below  $10^{-2}$  m, the spectrum becomes turbulent and shows a Gaussian shape.

The transition between the  $k^{-1}$  slope and the turbulent motion is marked by a minimum in

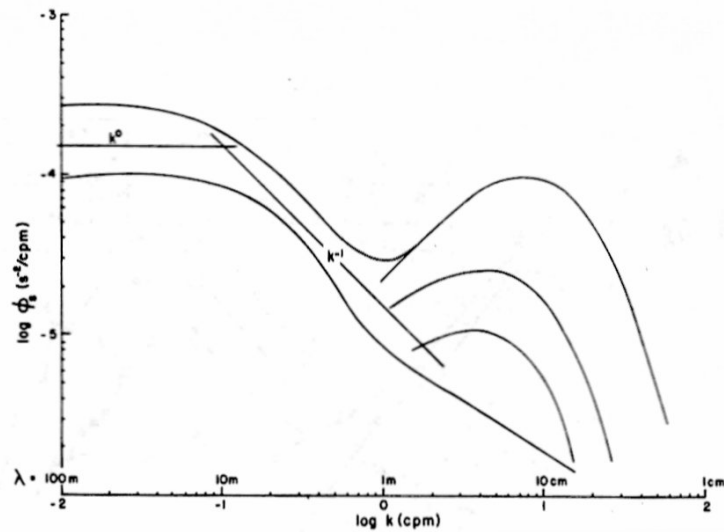


Fig. 2.2: Schematic composite spectrum of vertical shear of horizontal velocity; the spectrum is flat ( $k^0$ ) for wavelengths larger than 10 m, and falls as  $k^{-1}$  below that. Figure taken from Gargett et al. (1981).

spectral energy, at a buoyancy wavenumber determined by the average turbulent dissipation rate and the buoyancy frequency (Gargett et al., 1981). The shape of the spectrum, especially the cutoff wavenumber  $k_c$ , in energetic conditions above the GM levels is still subject to ongoing discussion. There is some evidence in microstructure data that instead of steepening the slope of the spectral roll-off,  $k_c$  shifted towards smaller wavenumbers in environments with elevated levels of turbulence and internal wave activity, e.g. Gregg et al. (1993), Polzin et al. (1995).

Strain is the vertical derivative of the vertical displacement just as the shear is that of the horizontal velocity. Since internal wave motions affect the velocity just as the density, it is clear that the shape of both shear and strain spectra should be comparable for a GM wave field (see Appendix A).

### *Energy Transfer to Small Scales*

The apparent universality of the spectral distribution of the internal wave field raised the question of which processes are responsible for those observations. Within the framework of the GM spectral model, four dynamical models of energy transfer within the internal wave range have been developed which also provide estimates for the dissipation rate  $\epsilon$  depending on stratification, energy and Coriolis parameter.

Two of them assume that energy transfer within the spectrum is due to wave-wave interactions; the first was proposed by McComas and Müller (1981):

Energy is transferred from the low wavenumber energy-containing scales to the high wavenumber cutoff by the action of two mechanisms: Waves having a wavenumber between two and four

times the inertial frequency decay from parametric subharmonic instability (PSI). This results in two waves of higher wavenumbers, each having half the original frequency. The other process, induced diffusion (ID), describes scattering of a high wavenumber/high frequency wave by a low wavenumber/low frequency wave.

The added flux of those wave-wave interactions is independent of wavenumber; thus, assuming a steady state balance, it can be equated with the dissipation rate :

$$\epsilon_{MM} = (2.1 \times 10^8 \text{ m}^2) f E^2 N^2 \quad (2.3)$$

where  $f$  and  $N$  are the inertial and buoyancy frequencies, respectively, and  $E$  is the dimensionless spectral energy level.

The above hinges on the validity of weak resonant interaction theory; an alternative approach was followed by Henyey et al. (1986): They used a ray-tracing approach to derive an analytical model, which can be argued to be valid also when nonlinear interactions are strong. The result is an expression similar in form to McComas and Müller (1981), except for an additional  $\cosh^{-1}(N/f)$  term:

$$\epsilon_{HWF} = (1.9 \times 10^7 \text{ m}^2) f E_{GM}^2 N^2 \cosh^{-1} \left( \frac{N}{f} \right) \quad (2.4)$$

A completely different concept was explored by Munk (1981): He related the dissipation rate  $\epsilon$  to the probability of wave breaking; this results in the following proportionality:

$$\epsilon_M \sim f^{1/2} N^{3/2} E^2 \quad (2.5)$$

The last prediction relates  $\epsilon$  solely to the stratification; internal wave scaling was applied to turbulent kinetic energy (TKE) equation (Gargett and Holloway, 1984; Gargett, 1990), and resulted in

$$\epsilon_{GH} \sim EN^{3/2}. \quad (2.6)$$

The latter two models have since been refuted by model-data comparison (see below).

## 2.2 *Finescale Parameterizations*

### *Thermal Dissipation*

In order to find a scaling for the thermal dissipation rate  $\epsilon$ , Gregg (1989) evaluated the predictions made by the models described above for the dependence of  $\epsilon$  on stratification, shear, and latitude, and compared the results to actual microstructure turbulence measurements from diverse locations in mid and low latitudes.

This comparison gave the best results for the functional dependencies proposed by McComas and Müller (1981) and Henyey et al. (1986); it indicated that the energy density of the internal

wave spectrum ( $E_{IW}$ ) can be related to the variance of finestructure vertical shear (wavelengths  $> 10$  m) of the horizontal velocity  $S_{10}^2$  in relation to the appropriate values from the GM model (see Appendix A) as

$$E_{IW}/E_{GM} = S_{10}^2/S_{GM}^2. \quad (2.7)$$

Thus, in analogy to the  $E^2N^2$  dependence of the scalings 2.3 and 2.4, the fourth moment of shear  $S_{10}^4$  can be used to express a parameterisation for the dissipation rate. In practice, the measured quantity is the variance of shear  $\langle S_{10}^2 \rangle$ , which translates, under the assumption of a Gaussian distribution, into  $\langle S_{10}^4 \rangle = 2 \langle S_{10}^2 \rangle^2$ . The resulting parameterisation

$$\epsilon = \epsilon_0 \frac{N^2}{N_0^2} \left[ \frac{|f|}{|f_0|} \right] \frac{\langle S_{10}^2 \rangle^2}{\langle S_{GM}^2 \rangle^2}, \quad (2.8)$$

can be used to calculate the dissipation rate from measurements of the buoyancy frequency  $N$  and the shear variance for wavelengths greater than 10 m,  $\langle S_{10}^2 \rangle = \langle (\partial u/\partial z)^2 + (\partial v/\partial z)^2 \rangle$ , with  $u, v$  the  $x$ - and  $y$ -components of the horizontal velocity.  $N_0, f_0$  and  $\langle S_{GM}^2 \rangle$  denote the GM reference specifications of buoyancy frequency, inertial frequency and 10 m-shear variance, respectively;  $\epsilon_0$  is a constant.

The best agreement between the different measurements occurred for a value of  $\epsilon_0 = 7 \times 10^{-10} \text{ W kg}^{-1}$  (Gregg, 1989). The scaling with the Coriolis parameter stems from the GM formulation, but whether it is appropriate in the parameterisation was not clear from that data set; therefore the  $f$ -term is bracketed in Equation 2.8.

While the model (2.8) worked well for data from locations with internal wave energy more or less in the range of the GM76 model, it apparently failed in regions where the frequency content of the wave field deviated significantly from the canonical values, e.g. near the equator (Peters et al., 1995) or in the Arctic (Wijesekera et al., 1993). In the latter case, in a region of energetic mixing, it was possible to remedy the underestimation of the dissipation by a factor of 10 by the use of a different parameterisation based on the vertical strain of the density field only (Wijesekera et al., 1993).

This inconsistency was resolved when Polzin et al. (1995) did a model–data comparison with an expanded data base comprising a greater range of different stratifications and data sets from non-GM environments. The parameterisation of Gregg (1989) was generally confirmed; however, the agreement between scaling and direct measurements for the non-GM data improved when Equation 2.8 was scaled with the local frequency content of the wave field. This frequency content is in most cases not known, but can be approximated by the use of the ratio of vertical shear to vertical strain,  $R_\omega$ , which corresponds to the average aspect ratio  $\alpha = k_h/k_z$  of the local wave field.

$$R_\omega = \frac{\Phi_s(\beta)}{N^2 \Phi_\lambda(\beta)} = \frac{(N^2 - \omega^2)(\omega^2 + f^2)}{N^2(\omega^2 - f^2)}, \quad (2.9)$$

where  $\Phi_s$  and  $\Phi_\lambda$  are the power spectral density of shear and strain in dependence on the wavenumber  $\beta$  ( $=|k_z|$ ), respectively (Fofonoff, 1969). The result is a modified version of Equation 2.8, namely

$$\epsilon = \epsilon_0 \frac{N^2 |f|}{N_0^2 |f_0|} \frac{\langle S_{10}^2 \rangle^2}{\langle S_{GM}^2 \rangle^2} F(R_\omega) \quad (2.10)$$

(Polzin et al., 1995), with a correction term  $F(R_\omega)$  which can be approximated by

$$F(R_\omega) = \frac{R_\omega + 1}{R_{GM} + 1} \sqrt{\frac{R_{GM}^3 \left[ 1 - R_\omega + \sqrt{(R_\omega - 1)^2 + 8R_\omega f^2 / N^2} \right]}{R_\omega^3 \left[ 1 - R_{GM} + \sqrt{(R_{GM} - 1)^2 + 8R_{GM} f^2 / N^2} \right]}} \quad (2.11)$$

(e.g. Kunze et al., 2002), where  $R_{GM} = 3$  is the shear to strain ratio  $R_\omega$  of a GM wave field.

### Diapycnal Diffusivity

The turbulent eddy diffusivity for density  $K_\rho$  is defined as

$$K_\rho \equiv -\frac{\overline{w'\rho'}}{\partial\rho/\partial z}, \quad (2.12)$$

i.e. the covariance of the fluctuations of vertical velocity  $w$  and density  $\rho$  divided by the mean density gradient. These flux quantities are difficult to measure directly. And, although a few successful attempts to do so have been made (e.g. Moum, 1990; Yamazaki and Osborn, 1993; Gargett and Moum, 1995),  $K_\rho$  is commonly evaluated from the dissipation rate  $\epsilon$  with the aid of parameterisations.

Osborn (1980), among others, used a TKE balance derived from the Navier-Stokes equation to relate the turbulent diffusivity to the kinetic energy dissipation rate  $\epsilon$  via a mixing efficiency,  $\Gamma$ , as

$$K_\rho = \frac{\Gamma\epsilon}{N^2}. \quad (2.13)$$

The mixing efficiency is defined by the flux Richardson number,  $R_f$ :

$$\Gamma = \frac{R_f}{1 - R_f}. \quad (2.14)$$

$R_f$  describes physically the ratio of turbulent buoyancy loss to the energy production by eddy stress acting on the mean shear. If it exceeds a certain value, turbulence will be suppressed. Theoretical considerations suggest that this is the case for  $R_f \approx 0.15$  (Ellison, 1957). Hence, it is possible to give an upper bound for  $\Gamma$  and thus for the diapycnal diffusivity,

$$K_\rho \leq 0.2 \frac{\epsilon}{N^2}. \quad (2.15)$$

There is some observational and laboratory evidence that the mixing efficiency in reality is about 0.2 or slightly above (e.g. Oakey, 1982), but there are also measurements which show considerable variations in  $\Gamma$  (Gargett and Moum (1995), for example) which likely depend on the origin and age of the turbulence and the ambient stratification (Smyth et al., 2001).

This derivation of the diffusivity hinges on several assumptions, which are partially equivocal (e.g. Davis, 1994b); it has, however, been widely used and proved to be a useful approximation, supported by results from tracer release studies (Ledwell et al., 1993). It is in any case advisable to keep its limitations and caveats in mind when using it to infer mixing rates.

### 2.3 Observational Methods

It was Munk who came up with a first estimate for a mean value of the eddy diffusivity in his famous *Abyssal Recipes* (1966). He assumed a simple balance between vertical diffusion and advection, and then determined the diffusivity with a fit of the balance to measured profiles of temperature, salinity, oxygen, as well as  $^{14}\text{C}$  and  $^{226}\text{Ra}$ . When accounting for things like oxygen consumption and radioactive decay, his calculations required a consistent diffusivity of  $10^{-4} \text{ m}^2 \text{ s}^{-1}$  for all the parameters to be in equilibrium, regardless of the location of the profiles. Also, the parameter distribution in the ocean agreed much better with turbulent than with laminar mixing, and he concluded that laminar fluxes could only add up to 1% of the total at maximum.

Since then, this was the magnitude for the diffusion coefficient which was expected to be found in the deep oceans. Astonishingly, open ocean experiments regularly came up with values an order of magnitude smaller than that (e.g. Kunze and Sanford, 1996; Ledwell et al., 1998), which led to the idea of mixing hot spots, and sparked off new concepts for research.

The various studies of the past couple of years have provided some insight as to where mixing happens, where it not happens, to what extent it does happen and how to measure it when and if it happens. The argument of whether the mixing is uniformly distributed throughout the ocean or whether it is confined to boundaries and hot spots now leans more and more towards the latter (Munk and Wunsch, 1998).

Process studies of mixing in the ocean are conducted with high-resolution measurements of temperature and velocity microstructure, often supplemented with accompanying CTD or current measurements. They were mostly programs confined to sites which were suspected to be mixing hot spots, often with the goal to link the magnitude of mixing to other, more easily accessible parameters like stratification and shear, and to refine the existent parameterisations.

Large scale studies which do not focus on the physics, but on the integrated effect of mixing are done by budget calculations of temperature, salinity and various other properties of water masses (Davis, 1994a). Occasionally, with the aid of tracer release experiments, actual measurements of mixing rates are accomplished (Ledwell et al., 1993; Watson et al., 1999; Ledwell et al., 2000).

Those are particularly valuable for a verification of the Osborn formulation for the mixing rate (Equation 2.13).

### *Mixing over Rough Topography*

One focus of these studies was the impact of various topographic features on the strength and location of mixing. Experiments were carried out in the vicinity of seamounts (Toole et al., 1994, 1997b; Kunze and Toole, 1997), fracture zones and passages (Ferron et al., 1998), mid-ocean ridges (Mauritzen et al., 2002; Thurnherr et al., 2002; Finnigan et al., 2002), and canyons (Kunze et al., 2002; Carter and Gregg, 2002).

Enhanced vertical mixing was found in, near and above overflows and passages, as for example the Romanche Fracture Zone. Here, the diapycnal diffusivity was as high as  $0.3 \text{ m}^2 \text{ s}^{-1}$  at the northeastern exit of the fracture zone, with the highest values just downstream of the main sill (Ferron et al., 1998). Bathymetric roughness was identified as a key trigger for vertical mixing in a comparison between the Mid Atlantic Ridge and the flat ocean floor in the Brasil Basin. The diffusivities were elevated above the ridges well into the water column, indicating the existence of not only a well mixed bottom boundary layer, but of remote effects, probably internal wave spreading, leading to more stirring in the water above rough bottom features (Polzin et al., 1997; Toole et al., 1997a; Ledwell et al., 2000; Morris et al., 2001; St. Laurent et al., 2001). The effectiveness of lee waves atop seamounts were studied in the Pacific, at Fieberling Guyot. The mixing there is confined to a relatively shallow layer atop the seamount with diffusivity up to  $1 \times 10^{-3} \text{ m}^2 \text{ s}^{-1}$  (Toole et al., 1994, 1997b; Kunze and Toole, 1997). Recently, in a coastal canyon, microstructure measurements revealed diffusivities 30 times larger than predicted by the Osborn parameterisation (Kunze et al., 2002); the reason for this is yet unclear.

Since some of these studies were conducted with several complementary instrumental setups, they also gave some insight as to whether the different means of measurement give comparable results and how those results are retrieved. Specifically, the results of microscale temperature and shear measurements were compared to results from CTD data (e.g. Ferron et al. (1998) and, recently, Mauritzen et al., 2002) or shear derived from current measurements, for example taken with XCPs (Gregg and Kunze, 1991). (This, among other things, was to test the formulation of shear parameterisations.)

Large scale budgets were mostly confined to enclosed basins, where the in- and outflow through passages were sufficiently known to encourage speculations regarding the vertical fluxes of mass and/or heat or other properties.

One interesting tendency in the results of the increasing number of studies is that while mixing in the main thermocline is weak, the deep oceans seem to experience much higher rates of turbulent stirring.

### 3. DATA

The main data base for this study was collected in the late summer of 1998, during the RV Polarstern cruise ARK XIV/2 (See Fahrbach (1999) for a detailed cruise report). The hydrographic stations are depicted in Figure 3.1. The cruise started on the 27th August in Tromsø, Norway, covered the Greenland Sea as well as Fram Strait, Denmark Strait and the northern tip of the Irminger Sea, and finally ended on the 15th October in Bremerhaven, Germany. A total of 282 hydrographic stations were occupied by a water sampling Rosette, a conductivity–temperature–depth probe (CTD) and, on most stations, a lowered acoustic Doppler current profiler (LADCP) attached.

#### 3.1 LADCP

##### *Data Coverage*

The focus of this investigation is on the evaluation of the current data measured by the LADCP, especially the vertical shear of the horizontal velocity. The distribution of stations (Figure 3.1) shows a good coverage of the different bathymetric conditions in the Greenland Sea: The 75°N transect comprises a smooth continental shelf in the west, followed by the abyssal plain and then crosses the steep submarine elevations and canyons of Knipovitch Ridge.

Two narrowband 150 kHz sonar with 20° beam orientation manufactured by RD Instruments (RDI, 1996) were being used throughout ARK XIV/2. The first instrument was in use from the beginning of the cruise up to station 114, when it sadly died of salt water leaking into a hairline crack in one of the sound transducers. It is unclear how long before the final breakdown this leakage was already going on and affecting the data quality. To be on the safe side (and for consistency), only the profiles measured with the second ADCP, which worked fine over the whole period, are being used.

This is not a problem as far as this study is concerned, because the profiles affected by the failure were located in the vicinity of Spitsbergen, the Fram Strait and the northern part of the Greenwich Meridian transect. The main area of interest, the Greenland Sea, was only reached after the change of instruments.

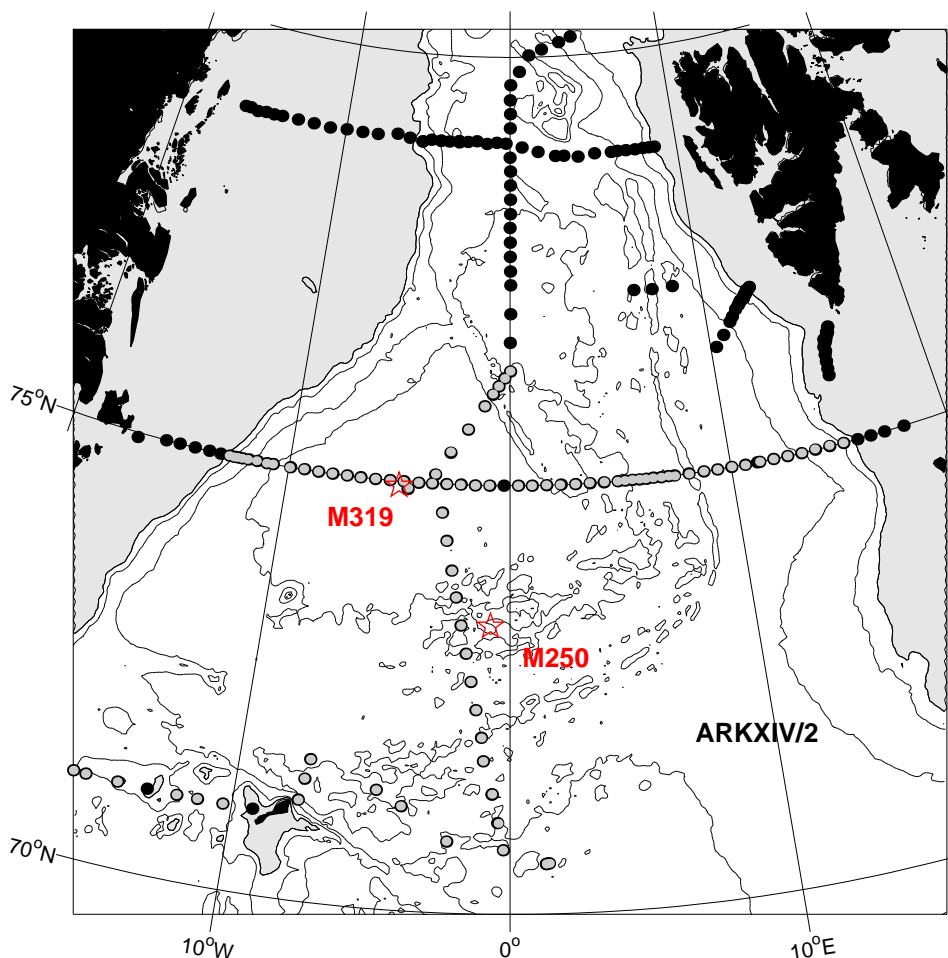


Fig. 3.1: Hydrographic stations from *Polarstern* cruise ARK XIV/2 (CTD and LADCP) and mooring locations. CTD profiles are marked with a black dot; where valid LADCP data are available at the same station they are marked with an additional grey dot. Mooring positions are marked with a star and the name of the mooring attached.

### *Principles of Operation*

An ADCP is a device which pulses sound (“pings”) of a defined frequency into the water. The sound is then reflected by small particles (e.g. plankton), which are carried along with the water current. Due to this motion, the frequency of the reflected sound pulse experiences a Doppler-shift. The ADCP receives the modified pulses, and the speed of the current is calculated from the frequency shift.

An ADCP has two pairs of transducers which are crosswise adverse orientated in the horizontal, and slanted towards the vertical, in order to resolve currents in all three directions in space. With four transducers and only three coordinates, the overdetermination of the third velocity is used to evaluate an error estimate of the measurement. The traveltime of the reflected ping can be used

to assign the transported signal to different depth bins. In doing so, every ping yields a profile of current speeds, the length of which depends on the settings of the device and on the abundance of scattering particles in the water. The disadvantage of the vertical slant of the transducers is an increasing horizontal separation of the four beams with increasing distance from the instrument, resulting in an increasing decorrelation of the measurements.

For the application as a Lowered ADCP, the ADCP is attached to the water sampling rosette with an autonomous energy source (battery pack), and in-house data recording (self-contained ADCP). The instrument pings continuously during up- and downcast, thus recording a “timeseries” of short profiles. After transferring the data to a PC, these are patched together to obtain a full depth profile of horizontal currents. Vertical currents cannot be determined with this setup, because the vertical speed of the lowered Rosette exceeds the magnitude of the vertical ocean currents by far.

The ADCP was set to a maximal range of 18 bins, with a bin length of 17.36 m (nominal 16 m, the difference is due to the 20° transducer angle instead of the standard 30°), which resulted in a total range of approximately 294 m. Since the Greenland Sea is rich in nutrients, the abundance of plankton was sufficient to gather data from all bins in most cases, although the strength of backscatter was somewhat reduced in depth greater than 2000 m (cf. Figure 4.9).

The instrument records internally the pitch, roll and heading, and was set to convert the measured velocity from beam coordinates into earth coordinates before recording them. The ping rate was chosen to be as fast as possible, which is approximately every 0.7 s. The save memory space, the instrument was programmed to ensemble average 12 pings at a time.

#### *Processing and Accuracy*

The processing of the raw data follows essentially the procedure described by Fischer and Visbeck (1993), with some modifications (discussed in detail in Section 4.5) due to the concentration on shear, rather than on absolute velocities.

According to the manufacturer (RDI, 1996), the total measurement error for each ping consists of a non-correctable unknown bias which is of the order of magnitude 0.5 – 1.0 cm/s, and a random error. This random error is uncorrelated from ping to ping and can be reduced by averaging. The standard deviation of the velocity error scales as (number of pings averaged)<sup>1/2</sup>.

Comparisons to independent current measurements show a mean accuracy of the final velocity profile in the order of 1–2 cm/s, with a standard deviation of up to  $\approx 5$  cm/s (Fischer and Visbeck, 1993). In this total velocity error, there are several factors contributing which only affect the final velocity profile, e.g. the accuracy of the navigation and possible data gaps, which both affect the determination of the barotropic component of the velocity. These errors, however, do not affect the individual shear estimates and are therefore only of minor significance for the present study. For a detailed discussion of the velocity errors, the interested reader is referred to Fischer and Visbeck (1993) and Firing (1998).

### 3.2 CTD and Bottle Data

#### *Instrument Setup*

The CTD was a Seabird SBE 911 plus equipped with one pressure, two salinity and two temperature sensors as well as an additional transmissiometer and a yellow-substance detector (only part of the cruise). Attached to the rosette were 21 12 Liter sampling bottles; the remaining space of three slots was used up by the LADCP. Five of the bottle were additionally equipped with electronic reversing instruments for temperature and pressure measurements. Supplementary salinity measurements were made from water samples using an Autosal salinometer.

#### *Processing and Accuracy*

All CTD data were loop-edited with 0 cm/s as minimum downward velocity and bin averaged over 1 dbar; spikes have been edited out individually. After sensor calibration before and after the cruise, the following accuracy was determined:

- Temperature: < 1.5 mK, with correction of +0.5 mK for temporal drift applied
- Salinity: < 0.002 psu
- Pressure: 1 dbar, with correction of -0.6 dbar relative to deck pressure applied.

(G. Budéus, pers. com.)

#### *CFCs*

The chlorofluorocarbons CFC-11 and CFC-12 were measured on 166 stations during the cruise from water samples, using a gaschromatograph-electron capture detection technique. The accuracy was determined by double analysis of the probes, and amounted to  $\pm 2\%$  or  $\pm 0.012$  pmol/kg (whichever greater). (M. Rhein, pers. com.)

### 3.3 Moorings

In addition to the dataset from *ARK XIV/2*, current meter records from two moorings from the central Greenland Sea (M319,  $74^\circ 57'$  N,  $4^\circ 59'$  W) and the flanks of Mohns Ridge (M250,  $73^\circ 21.5'$  N,  $0^\circ 48'$  W) were used for supplementary analysis. For the position of the moorings, see Figure 3.1. The moorings were parts of projects from the Institut für Meereskunde Kiel, and since their primary purpose was the monitoring of convective activity, the current meters have been deployed in the upper part of the water column. The water depth at the two locations was 3008 m (M250) and 3554 m (M319). A list of the instruments used and their settings is given in Table 3.1.

---

| Instrument | Mooring | Depth<br>(m) | Sampling Rate<br>(min) | Deployment<br>Time |
|------------|---------|--------------|------------------------|--------------------|
| RCM        | M319    | 347          | 60                     | 6/88–5/89          |
| RCM        | M319    | 1345         | 60                     | 6/88–5/89          |
| RCM        | M250    | 371          | 60                     | 7/88–5/89          |
| RCM        | M250    | 827          | 60                     | 7/88–5/89          |
| RCM        | M250    | 1437         | 60                     | 7/88–5/89          |
| RCM        | M250    | 2422         | 60                     | 7/88–5/89          |

---

*Tab. 3.1:* Overview of Moored Instruments

Details of the setup and data quality can be found for example in Schott et al. (1993); Visbeck et al. (1995), or Mertens (2000).



## 4. MIXING IN THE GREENLAND SEA

As mentioned before, the downward movement of isopycnals in the Greenland Sea suggests a non-equilibrium state. A possible reason for these observations may be that the effect of turbulent mixing is larger than counteracting vertical advection.

In the following, the boundary conditions for the existence of high levels of turbulent mixing are closely examined. Afterwards actual diffusivities are calculated with the aid of the parameterisations presented in Chapter 2.2 from finescale estimates of shear and stratification as measured with the CTD and Lowered ADCP.

### 4.1 Topography

Elevated levels of turbulence have been found in the vicinity or above topographic features, e.g. in the Brasil Basin, near the Mid Atlantic Ridge. This lead to the assumption that a rough topography supports the prevalence of high vertical diffusivities (Polzin et al., 1996). If this is indeed the case, the Greenland Sea is a place favourable for such topographic-induced mixing. The various ridge systems reveal topographic roughness on a multitude of scales.

In Figure 4.1, the variability of the seafloor topography is given in two different ways: depicted are the gradient and the Laplacian of the bathymetry. Used for the calculation is the seafloor elevation from the *International Bathymetric Chart of the Arctic Ocean* as included in the digital ETOPO-2  $2' \times 2'$  resolution global elevation and bathymetry data set (IBCAO, 2000; National Geophysical Data Center, 2001). The use of a gridded dataset implies that the mapped roughness of the seafloor is a lower boundary due to the limited horizontal resolution.

The gradient of the topography is obviously only a measure for the steepness of any given part of the seafloor, but not for its roughness. Therefore the Laplacian is calculated; it is not as demonstrative regarding real numbers, but gives a more accurate picture of sudden changes in the topography.

From Figure 4.1 it is clearly visible that most parts of the deeper (i.e. non shelf-) parts of the Greenland Sea are *not* flat. Even the so-called abyssal plain is, especially in the southeast of the Greenland Basin, covered with a great many bumps and hills of various horizontal extent. The steepness of the rises lies mostly in the range between 5 to 15% (lightblue to yellow in Figure 4.1), but exceeds 50% in some locations.

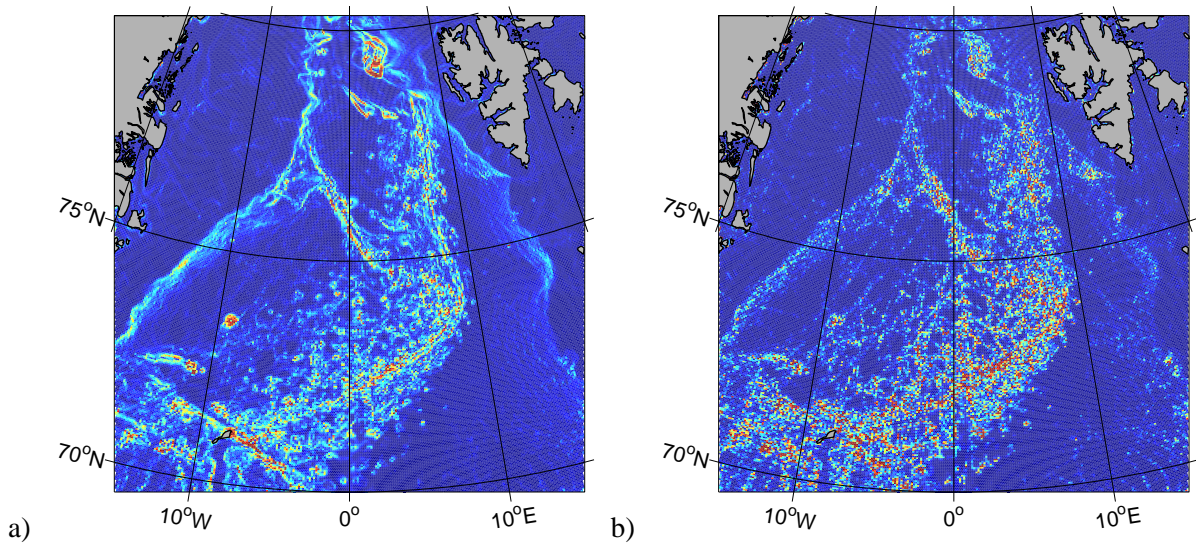


Fig. 4.1: Map of the roughness of the topography in the Greenland Sea, calculated in the two following ways: a) two-dimensional gradient of the elevation, and b) discrete Laplacian, i.e. a measure for the difference in elevation between a point and its four neighbors. The colouring ranges from blue for flat to red for variable topography. In a), the deepest red equals a slope of 20% and above. Topography is taken from ETOPO-2 (IBCAO, 2000; National Geophysical Data Center, 2001).

In contrast to this variability in the Greenland Sea, the Lofoten Basin (south and east of Mohns Ridge), which belongs to the Norwegian Sea, is very smooth and flat.

For the excitation of internal waves in the deep ocean, it is necessary for the horizontal scales of the topography and the horizontal excursions of the exciting frequencies and motions to match (Bell, 1975). Therefore, the seabed below the Greenland Sea Gyre is an excellent means to transfer energy to smaller scales by interaction with topography, and thus supports vertical mixing.

## 4.2 Stratification

When a water parcel is displaced from its position in the water column, it oscillates with a certain frequency, the Brunt-Väisälä or buoyancy frequency  $N$ , which is a function of the local density gradient (Equation 2.2). Given this definition,  $N^2$  (which is the directly computed quantity) is also a useful measure for the stability of a given water column.

The squared buoyancy frequency was calculated from 20 m mean profiles of temperature and salinity, using the adiabatic levelling method (Bray and Fofonoff, 1981; Millard et al., 1990). This algorithm results in a relative error smaller than 0.1% for depths shallower than 1000 m, and between 5 and 10% below that due to the smaller absolute values of the frequency (Millard et al., 1990).

A transect along 75°N is depicted in Figure 4.2. High stability is only found at the bottom

of the surface mixed layer and, to a certain extent, in the realm of the Atlantic inflow in the East. Below that, the stratification is generally weak. There is a local minimum where  $N^2$  drops below  $10^{-7} \text{ rad}^2 \text{ s}^{-2}$  ( $\approx 0.18 \text{ cph}$ ) in the centre of the Greenland Sea between 500 and 1200 m, the area and depth range which has been affected by convection in the preceding years.

The weakest stratification can be found in the abyss of the Greenland Basin and, to an extent, above the ridges and in the deep trench which forms the northern extension of the Norwegian Sea. The vertical extent of this minimum is up to a depth of about 1700 m, where the intermediate salinity maximum is located (cf. Figure 1.2). Above the ridge, at some stations occasionally patches of low  $N^2$  can be found up to marginally shallower depths.

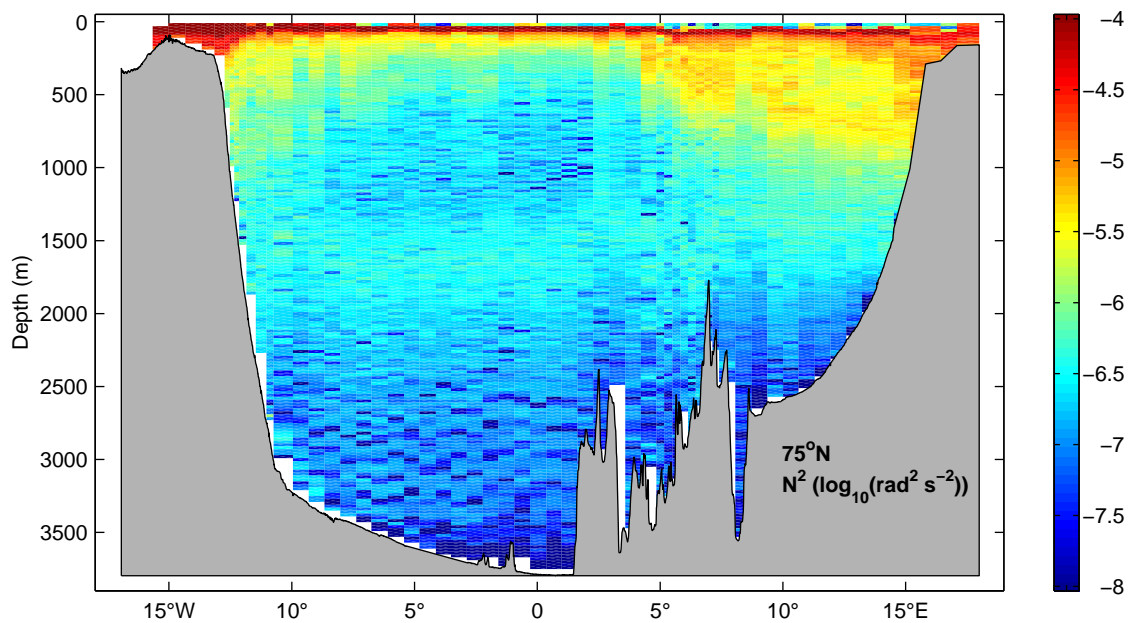


Fig. 4.2: Transect of buoyancy frequency for 20 m depth intervals along  $75^\circ\text{N}$ . Shown is the base 10 logarithm of  $N^2 = -g\bar{\rho}^{-1}(\partial\rho/\partial z)$ , calculated from temperature and salinity profiles. The logarithmic presentation was chosen for a better resolution of the differences in the deep water. The uneven horizontal resolution reflects the spacing of the hydrographic stations.

Especially in the region around the Greenwich meridian below 3500 m, the stability is very weak ( $N < 0.15 \text{ cph}$ ), and locationally the buoyancy frequency drops below the inertial frequency  $f$  ( $\approx 0.08 \text{ cph}$  in the Greenland Sea), thus restricting the internal wave field.

An interesting feature of the  $N^2$  distribution in the deeper layers is the apparent patchiness. Regions of practical inexistent stratification form ribbons of instability in the abyss of the Greenland Basin. In contrast to that, the stratification east of the Mohns Ridge belonging to the Norwegian Sea, while being comparable in magnitude, is much smoother and to a lesser extent marked by inhomogeneities. This is also visible when looking at a meridional transect (Figure 4.3), which is approximately coincident with the Greenwich meridian (cf. Figure 3.1). In this figure, the Mohns

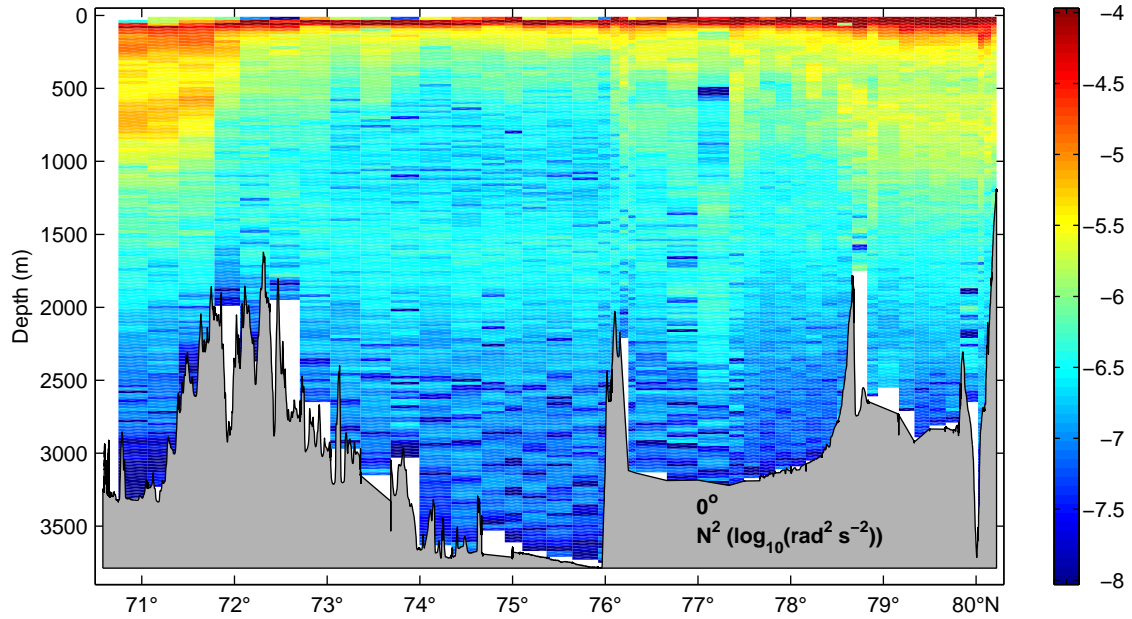


Fig. 4.3: Same as in Figure 4.2, but for the transect along the Greenwich meridian.

Ridge is located at 72°N, and the Lofoten Basin is south of that. The vertical structure in the Boreas Basin (north of 76°N) is not unlike that of the Greenland Basin; it seems, however, that the distribution is smoother towards the northern part of the basin.

### 4.3 Richardson Numbers

The gradient Richardson number  $Ri$  is the dimensionless ratio between the Brunt-Väisälä frequency and the squared shear,

$$Ri = N^2 / (U_z^2 + V_z^2), \quad (4.1)$$

where  $U_z$  and  $V_z$  are the vertical derivatives of the eastward and northward velocity, respectively.

$Ri$  is therefore a measure for the relative importance of the (stabilizing) effect of energy extraction by buoyancy and the counteracting destabilization by the shear, which transfers energy from the large-scale velocity towards smaller scales and ultimately turbulence.

The gradient Richardson number should not be confused with the overall Richardson number, which is the nondimensional number that describes the above ratio for the whole flow, and the flux Richardson number, which weights the energy gains and losses by eddy stresses and is used for the characterization of turbulent flows (cf. Section 2.2).

The critical Richardson number below which perturbations become turbulent is  $1/4$ ; if  $Ri > 1$  everywhere, the flow can be considered stable (Richardson (1923); see Thompson (1980) for a review of laboratory results on this). Likewise, no stable internal waves can exist if the Richardson

number of the background flow falls below  $1/4$  (Miles, 1961).

#### *Distribution of $Ri$ in the Greenland Sea*

For the Greenland Sea, the gradient Richardson number was calculated from CTD and LADCP data. On account of the resolution of the LADCP, which is approximately 17 m in the vertical, the calculation was restricted to 20-meter intervals. The buoyancy frequency was derived as described in Section 4.2, the shear estimates were also averaged into 20-meter bins. The calculation of  $Ri$  involves the division of two small quantities with comparatively large relative errors (up to 10% for  $N^2$  in the deep water (cf. Section 4.2), and up to 50% for the shear estimates, depending on the absolute magnitude of the shear), which leads to uncertainties of the same order of magnitude as the actual values. Therefore, the focus of the observations in the following should be on the larger structures, with not to much attention paid to the smaller details.

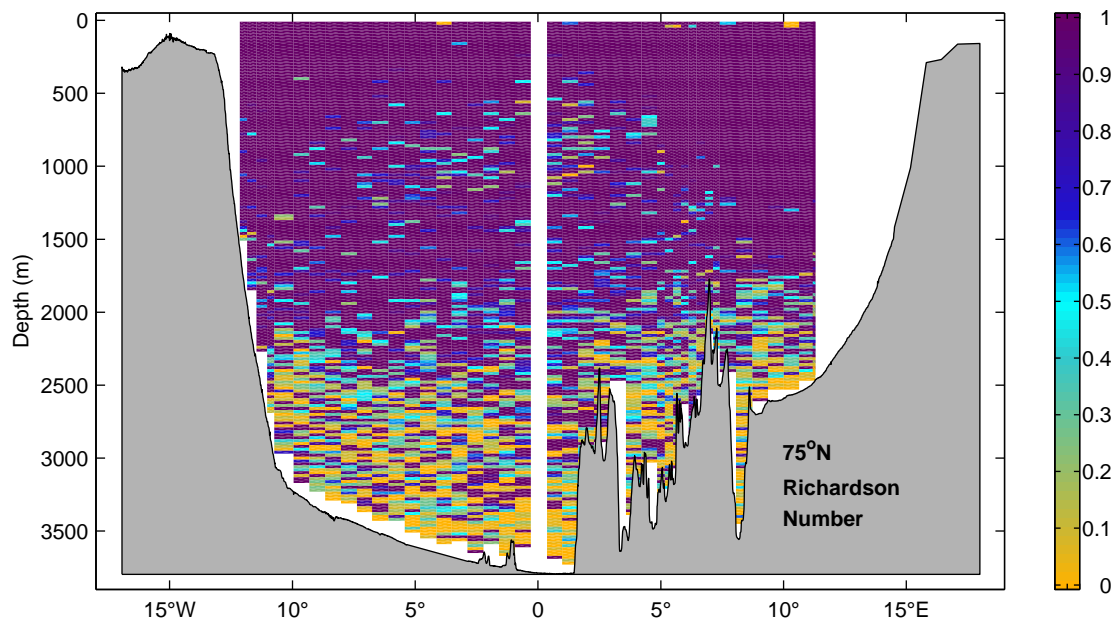


Fig. 4.4: Transect of Richardson number  $Ri$  along  $75^\circ\text{N}$ . The station at  $0^\circ$  is missing because of faulty LADCP data (See Section 3). The colour range is capped at one to emphasise the structures in the critical range around 0.25. Critical Richardson numbers are widely found in the deep basin below 2500 m and below 2000 m over the trenches and ridges.

The results of the calculation for the  $75^\circ\text{N}$  transect are pictured in Figure 4.4. The main thing that is obvious from the transect are the vast areas in the deep basin where  $Ri$  is close to the critical range. This includes to an extent the depth range which has been affected by convection, but mainly applies to the deep basin, where the value of 0.25 is frequently undercut.

### Contribution of Buoyancy vs. Shear

The Richardson numbers in the critical range are mainly due to the weak stratification (cf. Figure 4.2). But, the level of shear plays also a role in this: In Figure 4.5, the vertical shear as used in Equation 4.1 is plotted on the same transect as  $N^2$  for comparison.

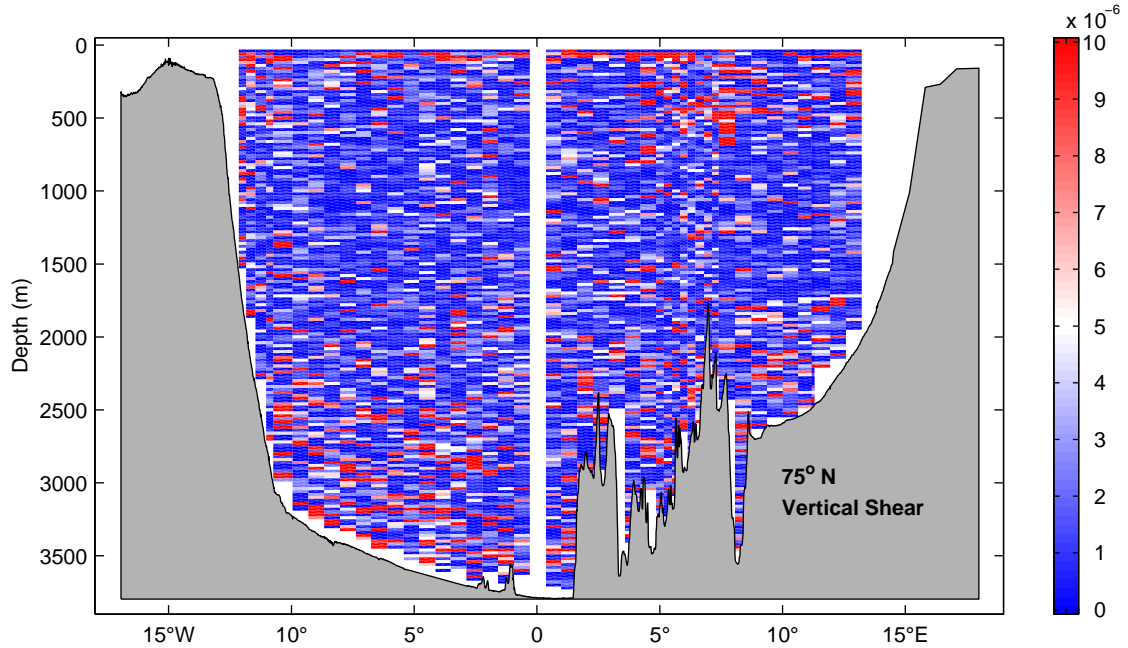


Fig. 4.5: Transect of squared mean vertical shear  $S^2$  of horizontal velocity at 20 m depth intervals along  $75^\circ\text{N}$ .

The variations are not large; the range lies between  $0 \leq S^2 \leq 10^{-5} \text{ s}^{-2}$ . However, apart from the higher levels near the surface (which one might expect), there is also a tendency for stronger shear in the deep water, which contributes to the low Richardson numbers in that region.

It is in principle possible to use the Richardson number to compute an estimate for the turbulent dissipation rate (Kunze et al., 1990; Polzin, 1996; Dengler and Quadfasel, 2002), but probably not advisable in this case. The method was originally developed for environments with a strong background shear flow, and is valid only in unstable events. Thus, deriving a mean  $\epsilon$  relies heavily on the proper detection of layers of unstable flow and their vertical extent. With the coarse resolution of the available shear data, a spectral method for the mixing estimate is to be preferred and will be carried out in Section 4.5.

### 4.4 Density Inversions and Thorpe Scales

Thorpe (1977) developed a straightforward empirical method to relate disturbances in the stratifi-

cation of a fluid to turbulent scales:

A stable stratified fluid shows a monotonous increase in density. Turbulent stirring results in overturning, and subsequently in density inversions. It is now possible to rearrange a measured density profile which may contain such inversions until it is monotonic. If there were any inversions, some parts of the profile have now changed their position. The stretch which a given point in the profile has to be moved in depth is called Thorpe displacement,  $d'$  (see Figure 4.6). The root mean square (rms) of the Thorpe displacements over a turbulent patch is called Thorpe scale  $L_T$ ,

$$L_T = \langle d'^2 \rangle^{1/2} \quad (4.2)$$

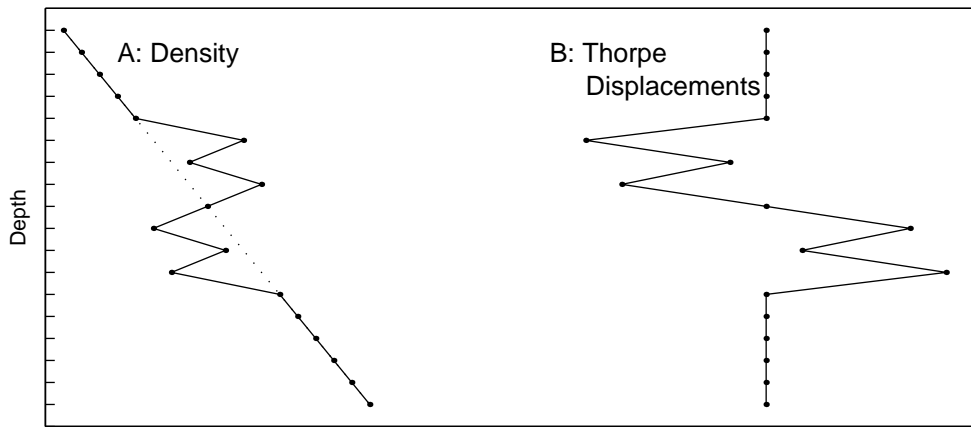


Fig. 4.6: Schematic density profile with inversions (A), and the Thorpe displacements ( $d'$ ) belonging to this profile (B). Negative displacements indicate a downward, positive displacements an upward movement necessary to generate a stable profile. The Thorpe scale for this patch would be  $L_T = 2.7$  vertical units. Figure adapted from Dillon (1982).

The Thorpe scale represents a characteristic length scale for a given overturn. In this sense, it can be related to the Ozmidov scale  $L_O$  (Ozmidov, 1965), which is a measure for the mean distance a parcel of fluid will move if it converts all its available potential energy into kinetic energy.

The Ozmidov scale is defined as

$$L_O = (\epsilon/N^3)^{1/2}, \quad (4.3)$$

where  $\epsilon$  is the dissipation rate of turbulent kinetic energy and  $N$  is the Brunt–Väisälä frequency.

Between  $L_O$  and  $L_T$ , a linear relationship of the form  $L_O = aL_T$  is expected. Several studies have been conducted with the goal to quantify the relationship between  $L_T$  and  $L_O$  by means of microstructure measurements. It turned out that the coefficient  $a$  equals more or less unity for several environments. Some oceanic values found for  $a$  are summarised in Table 4.1.

The Thorpe scale can therefore be of use in the determination of the local dissipation rate  $\epsilon$  and

consecutively the turbulent diffusivity,  $K_\rho$ . From Equation 4.3, substituting  $L_T$ , follows

$$\epsilon = a^2 \overline{\langle N^3 \rangle L_T^2} \quad (4.4)$$

and subsequently (cf. Equation 2.13)

$$K_\rho = \frac{\Gamma \epsilon}{N^2} = a^2 \Gamma \overline{\langle N \rangle L_T^2}, \quad (4.5)$$

where the the angle brackets denote an average over turbulent patches and the overbar an average over several vertical profiles. Note that the buoyancy frequency  $N$  must come from the individual profiles rather than from a mean, because the instantaneous stratification may be more important to the turbulence, especially in regions of internal wave activity (Dillon, 1982).

#### *Data Processing*

In this work, the algorithm developed by Ferron et al. (1998) was applied to calculate the Thorpe displacements and scales. It was chosen mainly because their data material presented the most similarities to that available here: Their study is the only one out of the existent literature (cf. Table 4.1) that used preprocessed CTD data with a 1 m resolution; still their algorithm gives results which are in reasonable agreement with the simultaneously conducted fine structure measurements.

Furthermore, they give a comparison between the Thorpe scales determined from temperature alone (as originally done by Thorpe (1977); he was working in a fresh water environment, where stratification is solely dependent on the temperature) and those derived from the density stratification. This is of importance for the present study, because in the Greenland Sea the salinity plays (especially in mid-depth) a significant role for the stability.

The use of CTD data with a low vertical resolution obviously limits the detection of overturns

| Relation                  | Location   | Author                   |
|---------------------------|--|--------------------------|
| $L_O = 0.79(\pm 0.4)L_T$  | Seasonal oceanic thermocline,<br>50°N, 145°W           | Dillon (1982)            |
| $L_O = 0.66(\pm 0.27)L_T$ | Permanent oceanic thermocline,<br>Equator, 150°W       | Crawford (1986)          |
| $L_O = 0.95(\pm 0.6)L_T$  | Romanche Fracture Zone, $\theta < 2^\circ\text{C}$     | Ferron et al. (1998)     |
| $L_O \approx 1.06L_T$     | Juan de Fuca Strait (Tidal channel, waterdepth < 250m) | Stansfield et al. (2001) |

Tab. 4.1: Overview over results of comparisons of the relation between Thorpe- and Ozmidov scales  $L_O = aL_T$  in oceanic environments.

to those with a large vertical extent. Although the value of the overall dissipation rate is dominated by the contributions of the larger overturns, the estimate of  $\epsilon$  will as a result be somewhat crude. Identifying “mixing hot spots” (if they indeed exist) should nevertheless be possible.

The ordering procedure was performed as follows (see Ferron et al. (1998) for a detailed description): Starting from an arbitrarily chosen density value, two consecutive densities are only considered significantly different if the second one differs by more than a value  $\delta$  from its predecessor. Hence,  $\delta$  is the threshold below which any signal is assumed to be below the instruments accuracy. In other words, the sensitivity of the overturn detection is determined by the noise level of the density measurements. If a small value for  $\delta$  is chosen, noise may be mistaken for overturns; on the other hand, if a more conservative  $\delta$  is assumed, some real overturns may be missed. The small background density gradient in the Greenland Sea ( $\overline{\partial\rho/\partial z} \approx -2 \times 10^{-5} \text{ kg m}^{-4}$  in the central GS below 1000 m) and the available high quality CTD data (cf. Section 3) justify to use a relatively low threshold of  $0.001 \text{ kg/m}^3$ .

Using this  $\delta$ , a so-called intermediate density profile is constructed, where (originating from the starting point) the single points always differ by a multiple of  $\delta$ . If the difference between two points in the original profile is smaller than  $\delta$ , they are considered the same, and the intermediate density is set accordingly, i.e.  $\sigma_{intermediate}(n) = \sigma_{intermediate}(n-1) + 0 * \delta$ . Again, if the difference between the two points lies within  $\delta$  and  $2 * \delta$ , the resulting intermediate density is set to  $\sigma_{intermediate}(n) = \sigma_{intermediate}(n-1) + 1 * \delta$  and so forth.

The intermediate profile is finally used to determine the displacements by sorting. This two step procedure ensures that the sorting is not corrupted by the instrument noise. For the calculation of the density profile, the reference pressure was varied according to depth range as follows: For depths shallower than than 800 m, the potential density  $\sigma_\theta$  (relative to surface pressure) was used;  $\sigma_1$  (relative to 1000 m depth) from 800 m to 1500 m,  $\sigma_2$  (2000 m) from 1500 m to 2500 m, and  $\sigma_3$  (3000 m) below 2500 m. Since the minimum vertical scale for the resolution of an overturn depends on the mean density gradient and the noise threshold as  $L_T = |(\overline{\partial\rho/\partial z})^{-1} * \delta|$ , in the deep Greenland Sea with its weak stratification only very large overturns with vertical scales typically exceeding 50 m can be resolved. As will be shown below, this constraint severely limits the number of detected overturns in the deeper parts of the Nordic Seas.

### Thorpe Scales

The resulting Thorpe scales are depicted in Figures 4.7 and 4.8. The vertical distribution of the Thorpe scales and the thickness of the corresponding overturns (Figure 4.7a) exhibits a large number of overturns of all sizes in the uppermost 1500 m, with  $L_T$  ranging from the minimum detection limit to nearly 40 dbar. At larger depths, the detection-limiting effect of the weak stratification is clearly visible: only a few, but very large, overturns show up in the analysis; the largest of those, with  $L_T$  between 20 and 50 dbar and a thickness of up to 300 m were found in the Boreas Basin.

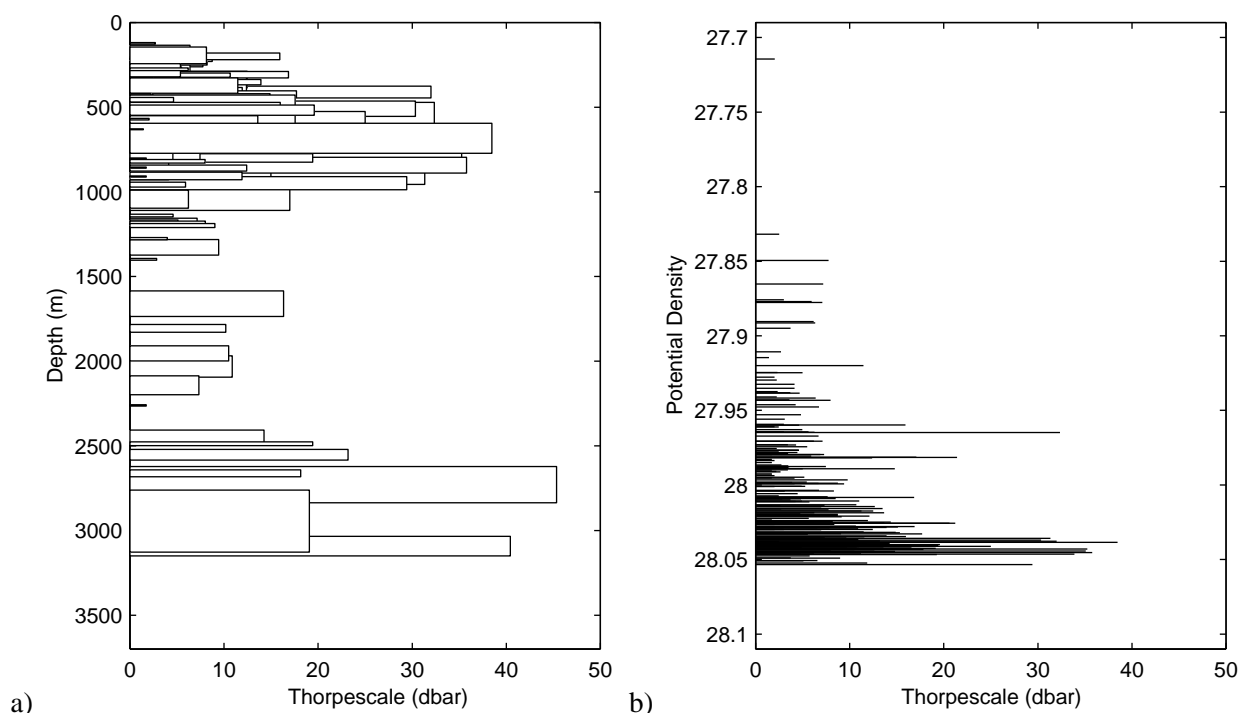
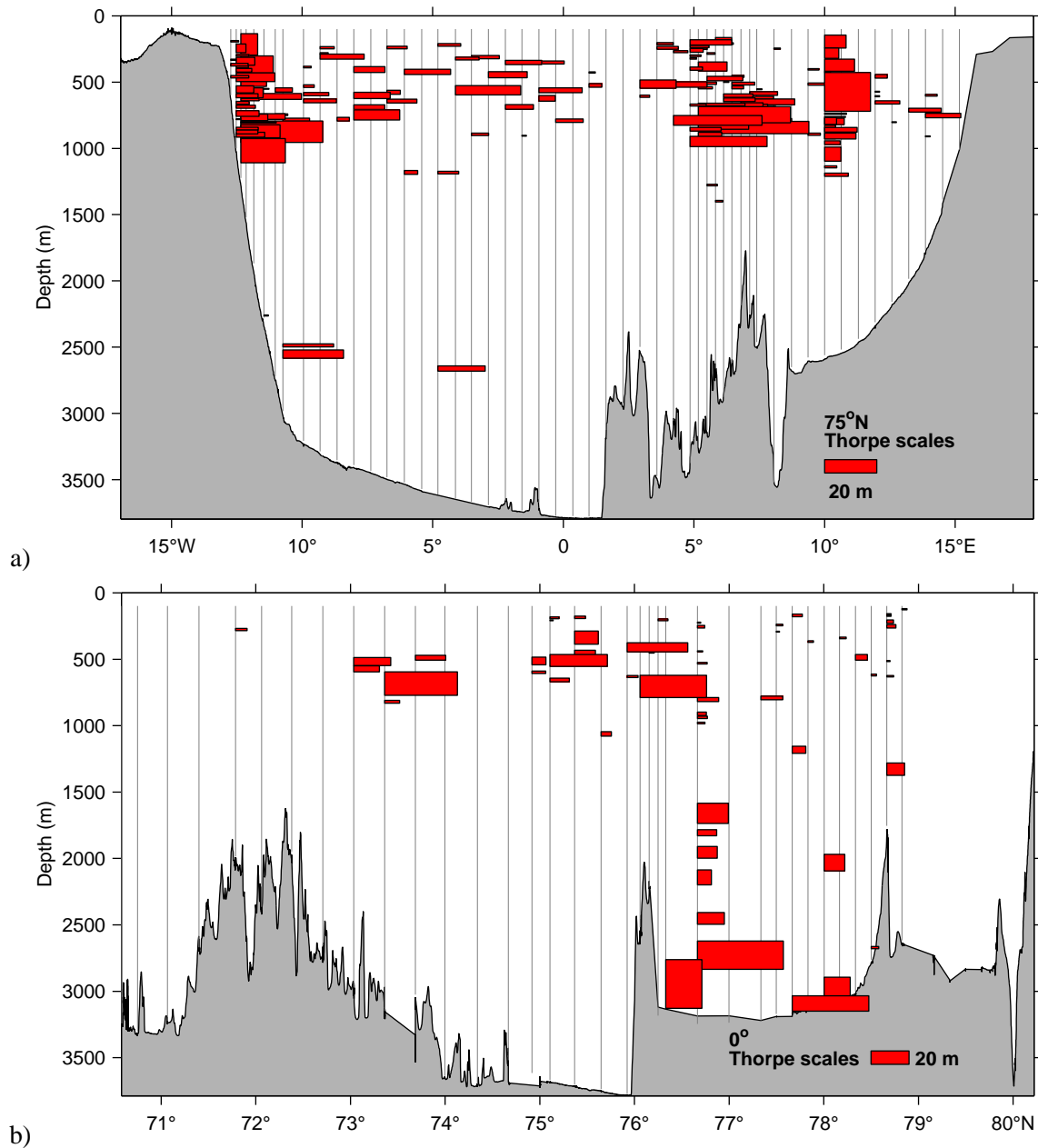


Fig. 4.7: a) Vertical extent and distribution of Thorpe scales for the Greenland Sea area, including the Boreas Basin and the shelves. b) Density distribution of the Thorpe scales for  $\sigma_\theta$ , corresponding to a depth range approximately from 100 to 800 m. The deep overturns visible in (a) occur in the Boreas Basin and near Knipovitch Ridge. Overturns below 2000 m along 75°N could only be detected on the lower boundary of the EBDW on the Greenland shelf break, where the stratification is slightly stronger than in the centre.

The distribution of the upper-layer Thorpe scales versus potential density  $\sigma_\theta$  (Figure 4.7b), which covers approximately the depth range between 100 and 800 m, shows that the majority of these overturns occur at densities greater than 28, which concurs with the lower boundary of the Atlantic Water inflow. When the horizontal distribution of the Thorpe scales is taken into regard (Figure 4.8), there is indeed an accumulation of overturns in the frontal region of this inflow (2° 30' – 7°E), suggesting an increase in baroclinic instabilities and mixing events at the boundary between the Atlantic Water and the Intermediate Water.

The Greenland shelf break with the EGC is the second region along the 75°N transect where a high number of overturns occur, albeit with slightly smaller Thorpe scales (Figure 4.8a). Also near the shelf slope, but at greater depths, occur about the only detections of deep overturns along 75°N. They are associated with the lower boundary of the inflow of EBDW from the Arctic. Except for the above mentioned two regions, the mixing events in the upper part of the water column do not exhibit a lot of structure; the overturns are typically thinner than 50 m with Thorpe scales less than 20 dbar.

Away from the 75°N transect, the largest overturns are found in the deeper parts of the Boreas



*Fig. 4.8:* Horizontal distribution of the Thorpe scales in the Greenland Sea along a) 75°N and b) the Greenwich Meridian. The horizontal scaling of the Thorpe scales is given in the lower right corner of each plot. The vertical extent of each patch corresponds to the thickness of the respective overturn. The greatest number of resolvable overturns occur in the upper layer, in the frontal regions of the Atlantic Water and in the EGC. Note that the weak stratification in the interior limits the detection of overturns to those of large vertical scales as, for example, in the Boreas Basin between 76° and 78°N. Thus the lack of Thorpe inversions in the abyss must not be interpreted as the nonexistence of mixing events in the deep Greenland Sea, but merely implies that the method is not successful in that particular environment.

Basin (Figure 4.8b), below 1500 m, with increasing thickness and Thorpe scales near the sea bed. A heightened number of mixing events can also be found in profiles from the Svalbard shelf (Storfjord outflow region) and above the Knipovitch Ridge (cf. Figure 3.1, both not shown here).

#### *Inferred Diffusivities*

For the obvious shortcome of overturn detection in the deeper parts of the basins, diffusivities were only estimated for the uppermost 1000 m of the water column, where the number and distribution of the Thorpe scales promised to give a reasonable picture of the ongoing mixing. Turbulent diffusivities for each overturn are computed using Equation 4.5, with the factor  $a = 0.95$  following Ferron et al. (1998) and a mixing efficiency  $\Gamma = 0.2$  (cf. Section 2.2). It should be noted, however, that there is evidence that the relation between Thorpe and Ozmidov scale in overturning events as well as the mixing efficiency change considerably during the temporal evolution of such an event (Smyth et al., 2001). Lacking direct estimates of Ozmidov scales, the above mentioned “conservative” values for  $a$  and  $\Gamma$  will more likely lead to an underestimation of diffusivity than to an overestimation (Smyth et al., 2001). The buoyancy frequency is taken as the mean over the vertical extent of the overturn in consideration. Following the calculation of the diffusivity for each patch, the values of each profile were vertically averaged over the uppermost 1000 m. Consecutively, an horizontal average was formed over several profiles. The resulting mean diffusivities can only be taken as a crude estimate, since the profiles entering the averaging process are coming from a wide spatial and temporal range and thus rely on the implicit expectation that the mixing is relatively time-invariant.

The above procedure results in a mean value of  $K_\rho = 1.9 \times 10^{-4} \text{ m}^2 \text{ s}^{-1}$  for the Nordic Sea; this estimate includes all available profiles from the Greenland Sea, Boreas Basin, Knipovitch Ridge and the shelves. When only the  $75^\circ\text{N}$  transect is taken into consideration, the mean increases to  $K_\rho = 2.5 \times 10^{-4} \text{ m}^2 \text{ s}^{-1}$ ; this result does not depend on whether only the Greenland Sea Gyre (west of  $8^\circ\text{E}$ ) or the total transect is included into the calculation. The main contribution for the mean diffusivity comes from the two regions with enhanced numbers of overturns, the EGC and the front between Atlantic and Intermediate Water. The East Greenland Current area, between  $13^\circ\text{W}$  and  $12^\circ\text{W}$ , shows a mean of  $K_\rho = 9.8 \times 10^{-4} \text{ m}^2 \text{ s}^{-1}$ . The frontal region, above the ridges, is taken to reach from  $2^\circ 30'$  to  $7^\circ\text{E}$ , and has a mean diffusivity of  $K_\rho = 3.6 \times 10^{-4} \text{ m}^2 \text{ s}^{-1}$ .

As an aside, the Storfjord shelf region exhibits also enhanced mixing rates with a mean diffusivity of  $K_\rho = 4.6 \times 10^{-4} \text{ m}^2 \text{ s}^{-1}$  and a maximum of  $K_\rho = 1.8 \times 10^{-3} \text{ m}^2 \text{ s}^{-1}$  over one of the profiles. The largest overturns here occur between 400 and 800 m depth. These estimates compare favourably with results from Fer and Haugan (2003); they calculated Thorpe scales from 0.1 dbar resolution CTD data to study the mixing of the dense water outflow of the Storfjord Plume, and found diffusivities up to  $10^{-3} \text{ m}^2 \text{ s}^{-1}$  in the plume.

### *Discussion*

The detection of mixing events by calculating the scales of density inversions from CTD profiles provides a useful and consistent picture of the spatial variability of mixing in the upper parts of the Nordic Sea. The highest number of overturns were found in the area of the East Greenland Current, which has been reported to be an effective mixing environment; baroclinic instabilities in the EGC have been suspected to be accountable for mixing in this area, but exhibit considerable year-to-year variability (Strass et al., 1993). Similar instabilities are also the likely cause of overturns in the frontal region between the warm saline Atlantic Water in the West Spitsbergen Current. The resulting diapycnal diffusivities for the Greenland Basin lie with values between  $10^{-4} \text{ m}^2 \text{ s}^{-1}$  and  $10^{-3} \text{ m}^2 \text{ s}^{-1}$  in the same range as those derived by a tracer release study, which was conducted in almost the same depth range (200 – 1000 m) in the Greenland Sea Gyre to study the penetration of wintertime convection (Watson et al., 1999).

In the abyss, however, the method is failing; it cannot be decided from the CTD measurements alone whether there really are no overturns in the deep waters or if the unfortunate signal-to-noise ratio inhibits the detection. The detection of the very large overturns in the deep Boreas Basin deems it reasonable to expect the existence of (smaller) ones also in the Greenland Basin. Overall it can be concluded that Thorpe scales, while they certainly give satisfying results in the upper ocean, are not a useful tool to really quantify mixing rates in the physical environment of the deep parts of the Greenland Sea.

In the following sections, a complementary approach using the finescale shear and strain as obtained from CTD and Lowered ADCP profiles will be undertaken, to evaluate the energy content of the internal wave field and thus quantify the dissipation rates and turbulent diffusivity in the abyss of the Greenland Sea.

## *4.5 Shear Calculated from ADCP Measurements*

The use of LADCP data for the calculation of shear levels and subsequent determination of dissipation rates and diffusivities is a relatively new and not-yet-established idea. It was first suggested by Polzin and Firing (1997) and in its feasibility further explored by Polzin et al. (2002). Whereas the LADCP when used as a means of current measurement is commonly operated with a bin size of 16 m, and therefore not entirely sufficient for the resolution of the finescale, its operational use and wide coverage yields a certain charm when compared to the expenditure usually involved with fine- or microstructure measurements.

### *4.5.1 Processing of the Lowered ADCP Data*

The processing of the raw data follows basically the procedure described in Fischer and Visbeck (1993), with the following modifications and thresholds:

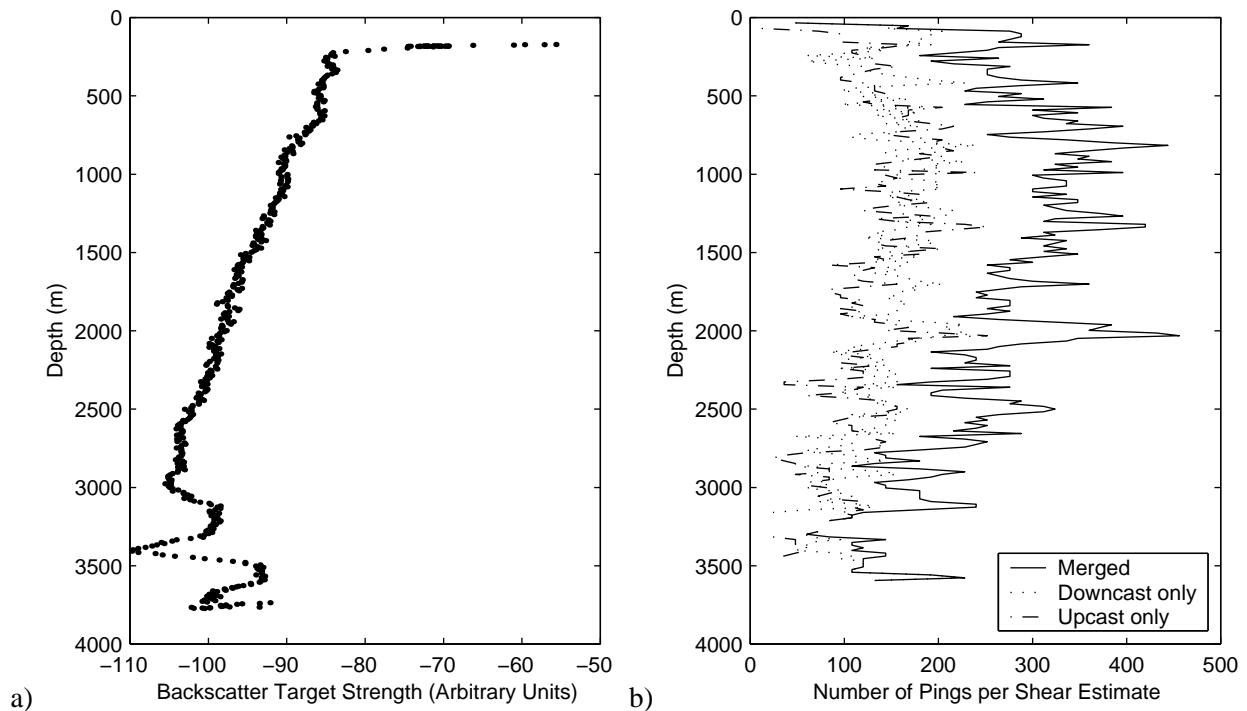


Fig. 4.9: a) Sample backscatter target strength of Lowered ADCP profile (Stn. 155, 75°N, 0° 57' W). The strong signals in greater depth are caused by bottom reflection. b) Number of pings included in each shear estimated for the same profile, shown separately for up- and downcast. In the range of the bottom this number is partly reduced because of outlier rejection.

- To minimise the inherent smoothing effect, the computation of the shear from the raw velocities was changed from central to first differencing.
- Raw data bins where the total (pitch and roll) instrument tilt exceeded 18° were rejected.
- Likewise, bins where the vertical and error velocity departed more than one standard deviation from the mean and from zero (respectively) were expelled.
- In the binning process, shear estimates that differed more than 2.8 times the standard deviation from the mean were discarded as outliers.
- The averaging of the single shear estimates for the final shear profile was done in 17.36 m bins, which equals the original bin size of the measurement and was chosen to ensure an adequate amount of raw data entering each final estimate. This resulted in  $O(100)$  pings per individual up- or downcast estimate in the deep water and rises up to  $O(200)$  in mid-depth. (See Figure 4.9 for a typical profile from the central Greenland Sea).

For the calculation of the shear spectra and -variance, the up- and the downcast of each profile are treated separately, in order to take the possible temporal variability into account (A full depth

cast last up to two or three hours, depending on depth and lowering speed). Unless otherwise indicated, only the data from the downcast are presented in the analysis and the figures, since the heaving was typically done with higher speed than the lowering, resulting in a diminished number of shear estimates per depth bin and thus a lessened accuracy.

In the range of the bottom, the ADCP receives a strong backscatter signal, that is not caused by particles in the water but by bottom reflection. Since this bottom signal is much stronger than the adjacent readings from the water column it tends to mask those, and consecutively causes spurious shear estimates. These are largely caught by the editing process, and thus leave data gaps in the profiles (cf. Figure 4.9). The gaps are expected at a height of approximately 375 and 250 m above the seafloor (evaluated for second and third reflection assuming a sound speed of 1500 m/s), and are smeared out somehow by the ensemble averaging.

To avoid contamination of the shear spectra by the data gaps, the gaps in the shear records were padded with zeros for analysis, and the calculation of the spectra was performed separately. To discard the data below the first occurrence of bottom reflection impact would mean to lose a significant portion of the data from the lower water column. Thus, the data are included in the analysis, but are indicated for clarity. It should be noted that the error for those bottommost values is larger, but the treatment of the gaps is not likely to add energy to the variance estimates. Furthermore, there is no evidence for an offset between the parts of the profile above and below the gaps (e.g. Figure 4.19). The inclusion of the bottommost data points covers in part the bottom boundary layer, since the casts typically end ten to twenty meters above the sea bed. A heightened mixing rate in the BBL would thus show up in the results of the bottommost segments of the analysis, but would be smeared out because of the need to include non-BBL parts of the water column.

While most of the shear in the profiles is comprised to the small wavelengths, the energy is constrained to the low wavenumber part of the spectrum. Hence it is desirable to resolve as much of this low wavenumber part as possible. Compromising between the coverage of the energy containing scales and the attempt to retain at least some sort of vertical resolution, every profile is subsequently divided into overlapping 1100 m length sections (corresponding to 64 data points). These sections are Fourier-transformed individually, with the prior application of a Hanning window of the same length to avoid spectral leakage. Shear variance is then derived by summation of the coefficients, with proper scaling according to sampling frequency and prior filtering.

#### *Spectral Correction of the Fine Scale Response*

A spectral correction has to be applied to the shear to correct for the characteristic attenuation at higher wavenumbers (shorter wavelengths). It accounts for the inherent filtering of the ADCP on the basis of finite bin length, beam configuration and so forth (Figure 4.10).

After conducting a comparison between the finescale characteristics of high-resolution shear

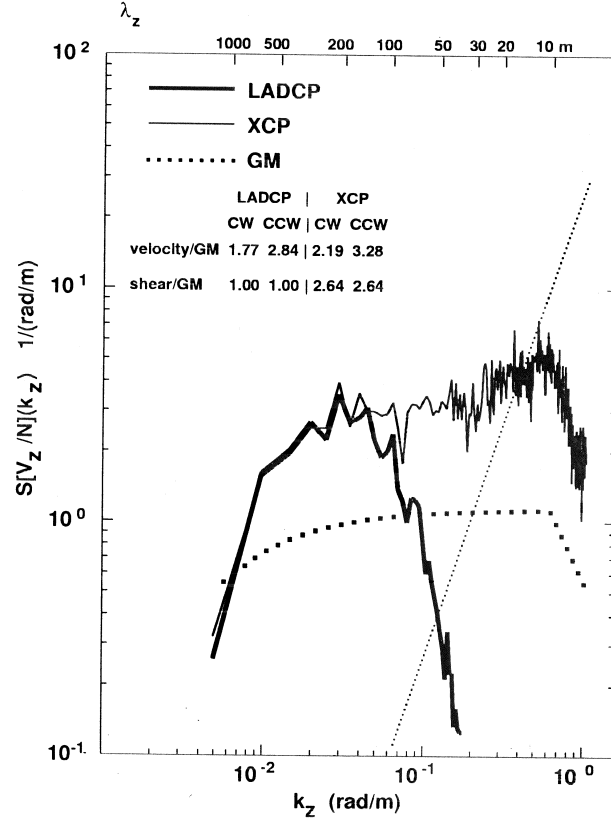


Fig. 4.10: Attenuation of Lowered ADCP shear spectrum at short wavelengths compared to high resolution measurement from XCP; Figure taken from Polzin et al. (2002).

measurements with XCPs (Expendable Current Profilers) and LADCP, Polzin et al. (2002) found that the observed transfer function could also be determined by modelling the various filters inherent to the LADCP measurement and data processing.

The theoretical transfer function in dependence on the vertical wavenumber  $\beta$  ( $\text{rad m}^{-1}$ ) is composed of the transfer functions accounting for range averaging ( $T_{ra}$ ), finite differencing ( $T_{fd}$ ), interpolation ( $T_{int}$ ), instrument tilt ( $T_{tilt}$ ), and beam separation ( $T_{bst}$ ) (Polzin et al., 2002):

$$\begin{aligned}
 T_{theo}(\beta) &= T_{ra}(\beta)T_{fd}(\beta)T_{int}(\beta)T_{tilt}(\beta)T_{bst}(\beta) \\
 &= \text{sinc}^2\left(\frac{\beta\Delta z_t}{2\pi}\right)\text{sinc}^8\left(\frac{\beta\Delta z_r}{2\pi}\right)\text{sinc}^2\left(\frac{\beta\Delta z_g}{2\pi}\right) \\
 &\quad \times \text{sinc}^2\left(\frac{\beta d'}{2\pi}\right)T_{bst}(\beta)
 \end{aligned} \tag{4.6}$$

where  $\Delta z_t$  is the length of the transmitted sound pulse;  $\Delta z_r$  is the length of the depth bin,  $\Delta z_g$  is the grid spacing and  $d'$  is a the range depending constant.

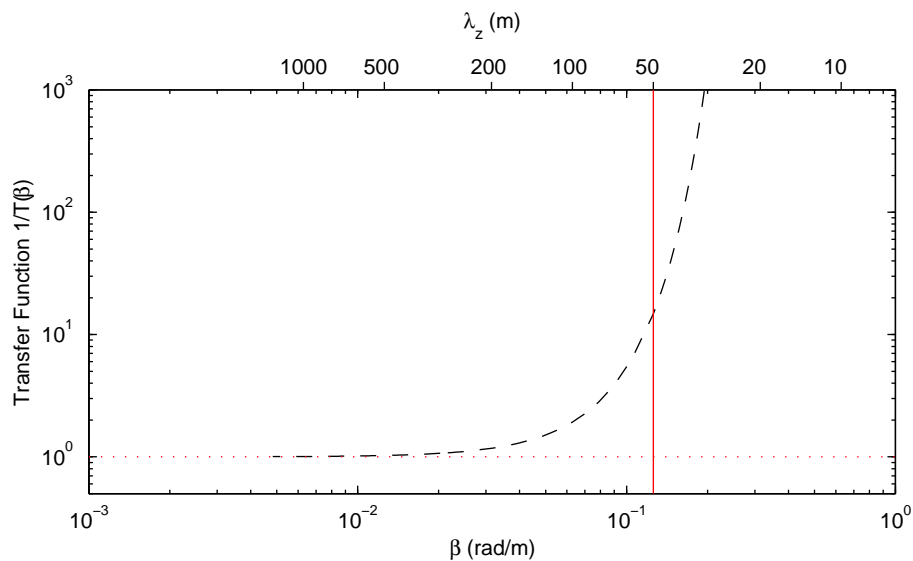


Fig. 4.11: Spectral transfer function  $T$  in dependence on the wavenumber  $\beta (= 2\pi k)$ , according to Polzin et al. (2002); computed with the settings listed in Table 4.2. The vertical line denotes the maximum wavenumber for the integration of the spectra.

| Term         | Value   |  |
|--------------|---------|--|
| $\Delta z_t$ | 17.36 m | Length of sound pulse                          |
| $\Delta z_r$ | 17.36 m | Length of depth bin                            |
| $\Delta z_g$ | 17.36 m | Spacing of vertical grid                       |
| $d'$         | 12.5    | Range parameter, corresponding to 272 m range* |

\* Real range in our configuration ( $20^\circ$  angle of beams) is 293.6 m

Tab. 4.2: Settings of the LADCP as used for the spectral correction applied prior to the shear variance analysis.

$d'$  is given to be 5.75, 9.0 and 12.5 for ranges 96, 160, and 272 m, respectively (Polzin et al., 2002). The maximum range for our instrument setup was somewhat larger than the latter (293.6 m instead of 272 m) because of a smaller beam angle. Since these values for  $d'$  were computed numerically and no functional dependence was given, the maximum value of 12.5 was used in this study.

The beam-separation transfer function  $T_{bsl}$  depends on the horizontal wavenumber spectrum at the location of the measured profiles. If this is not known (as it is the case here), the effect of the beam separation can be ignored by setting this term to 1 and thus slightly underestimating the finescale shear.

The settings of the LADCP that enter into the computation of the transfer function are sum-

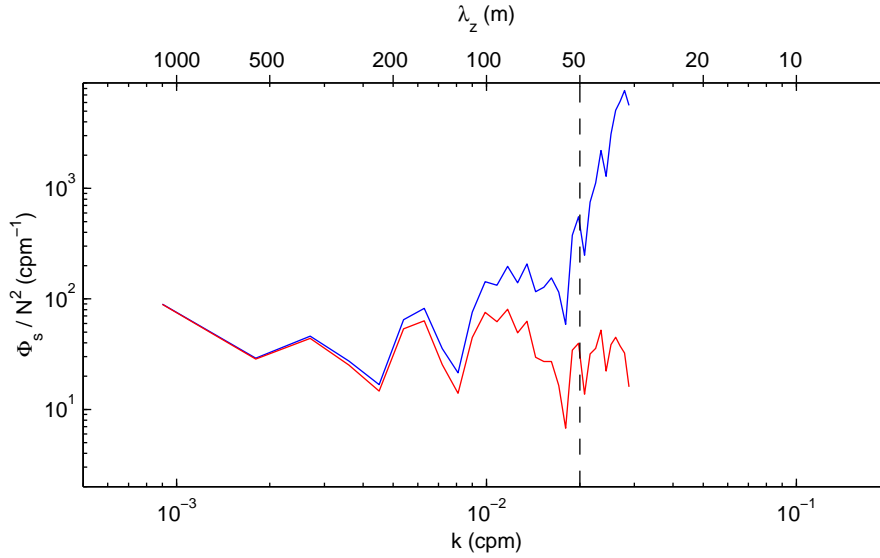


Fig. 4.12: Effect of the spectral transfer function: Shear spectrum of a single Lowered ADCP profile (Stn. 155, 75°N, 0° 57' W, downcast, depth range 2050–3150 m) with (blue) and without (red) application of the finescale correction. Note that the correction may mask an onset of instrument noise for high wavenumbers.

marised in Table 4.2. The transfer function itself is depicted in Figure 4.11. The effect of the application of the transfer function can be seen in Figure 4.12, where the uncorrected shear spectrum of an LADCP profile is shown in comparison with the corrected one. The spectral correction has an increasing impact for wavelengths smaller than 200 m.

#### 4.5.2 Shear Spectra

The resulting scaled shear spectra for several groups of stations (locations listed in Table 4.3) from the Greenland Sea are shown in Figures 4.13, 4.14 and 4.15. For the purpose of comparison, the respective GM spectrum for shear (cf. Appendix A) is included in the plots. Depicted are three depth ranges (where available): A shallow depth range, that contains profile segments between 500 and 1600 m depth to represent the convectively ventilated intermediate water masses, an intermediate depth range from 1500 to 2600 m depth covering the upper portion of the deep water, and a deep range below 2500 m for the lower deep and bottom waters. This last range is only satisfyingly covered for the central basin, where the water depth is sufficiently large and several deep stations were occupied. Few stations cover the required depth range at the shallower rims of the basin, thus no mean spectra are presented for the deepest range for want of enough profiles to form a meaningful average. The deep-range spectrum in Figure 4.14a from the Greenland Fracture Zone represents not an average but a single profile, and is included only for the purpose of comparison.

The profiles from the respective groups were combined for averaging under the reasoning that

| Area                          | Location                     | Depth Range<br>(m) | Number of<br>Profiles |
|-------------------------------|------------------------------|--------------------|-----------------------|
| Central Greenland Sea (GS)    | 74°– 75°40' N, 10°W – 2°E    | 500–1600           | 24                    |
|                               |                              | 1500–2600          | 24                    |
|                               |                              | 2500–3600          | 7                     |
| Greenland Fracture Zone (GFZ) | 76°– 76°30' N, 0°– 1°20' W   | 500–1600           | 5                     |
|                               |                              | 1500–2600          | 3                     |
|                               |                              | 2500–3600          | 1                     |
| Knipovitch Ridge (KR)         | 75°N, 2°E – 8°E              | 500–1600           | 10                    |
|                               |                              | 1500–2600          | 8                     |
| Mohns Ridge (MR)              | 71°45' – 74°N, 1°W – 2°30' W | 500–1600           | 5                     |
|                               |                              | 1500–2600          | 5                     |
| Greenland Shelf (SHELF)       | 75°N, 12°30' W – 10°W        | 500–1600           | 5                     |
|                               |                              | 1500–2600          | 2                     |

Tab. 4.3: Locations and depth ranges of profile ensembles.

the hydrographic conditions and characteristics were sufficiently similar. The central basin (Figure 4.13) is the largest homogeneous area, thus all 24 spectra from that area were combined to form the mean. The shear spectra from the rims of the Greenland Sea connected to rough topography (Figure 4.14) have been divided into three different groups, mainly with regard to the comparability with the strain spectra and the differences in the hydrographic conditions. The number of profiles entering the average is smaller, with a maximum of 10 for the eastern boundary with the Knipovitch Ridge. Figure 4.15 shows average spectra from the Greenland Shelf, which (contrary to the other rims of the basin that are marked by steep ridges and fracture zones) has a smooth topography.

Common to all locations, whether from the central Greenland Sea or from the rims of the basin, is the high shear spectral density; it increases from the shallow depth range, where it mostly agrees with the GM predictions, towards deeper depth ranges. Notably in the centre (Figure 4.13), it is clearly visible that the spectral density of the shear rises from the upper layer towards the bottom, where it exceeds the GM level by more than an order of magnitude. The other common feature of all average spectra regardless of depth range is the rise at high wavenumbers. This is probably at least partly caused by instrumental noise and will be discussed separately below.

The two average spectra from the shallow and intermediate depth ranges of the centre of the Greenland Sea are very similar. They are essentially flat with only a very weak positive slope for wavelengths larger than 100 m, and thus in accordance with the canonical shear spectrum proposed by Gargett et al. (1981). Their spectral density lies slightly above the appropriate GM spectrum with the intermediate depth spectrum showing the higher level. For wavelengths smaller than 100 m, the slopes of both spectra start to steepen. The energetic spectrum from the deepest range exhibits a

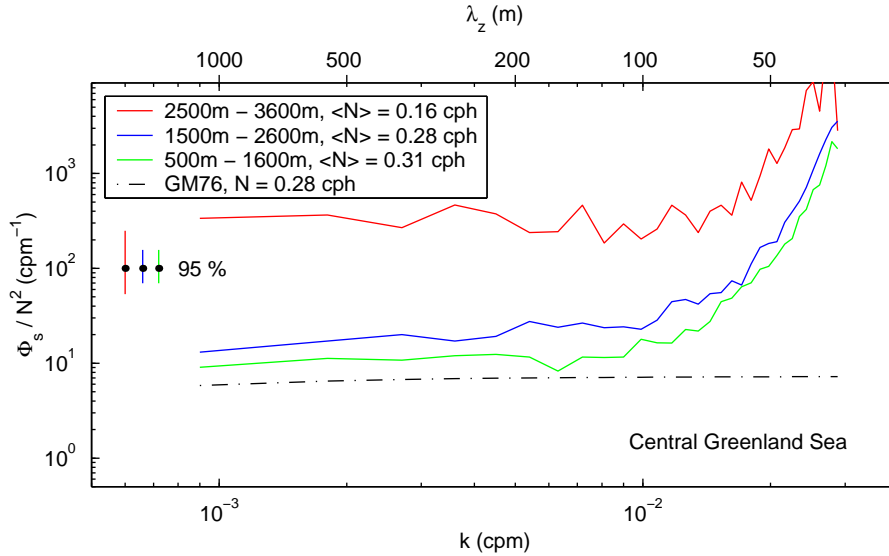


Fig. 4.13: Average buoyancy scaled shear spectra from the central Greenland Sea for 3 different depth ranges, 500 – 1600 m, 1500 m – 2600 m, and 2500 m – 3600 m. Each spectrum represents a mean over 24 profiles, except for the deepest range with only 7 profiles (bottommost part of profiles included). The GM76 spectra for the buoyancy ranges not shown in the figure differ only slightly in the low wavenumber range.

weak negative slope in the low wavenumber part. Slight departures from a GM behaviour like this have no significant impact on the validity of the dissipation parameterisation (Polzin et al., 1995).

The structures of the different average shear spectra from the rims of the Greenland Sea are relatively similar, with the notable exception of those originating from near the Greenland Fracture Zone. The deeper layers of all areas are more energetic than the shallower, just as in the central Greenland Sea. The spectra from the Greenland Fracture Zone (Figure 4.14a) show a peculiar departure from the canonical shape. The average from the middle depth range exhibits a distinct minimum of spectral density at intermediate wavelength between 150 and 500 m; the reason for this minimum is unclear. The one available deep spectrum is almost mirror-image shaped, except for the high wavenumber increase.

The low wavenumber portions of the spectra from Knipovitch Ridge, Mohns Ridge (Figures 4.14b,c) and the Greenland shelf (Figure 4.15) exhibit an approximately zero slope, with a tendency towards positive slopes for the shallow spectra, notably at the Greenland shelf. Above 1500 m, the spectral density is more or less that of a GM76 wave field, increasing in the intermediate layer towards approximately five times GM. In the low wavenumber part of the shallow spectrum from the profiles of the western rim of the Greenland Sea across the continental margin, higher shear spectral densities might be expected because of the low mode baroclinic waves that are known to travel along the shelf break in the East Greenland Current in this depth range (Lam,

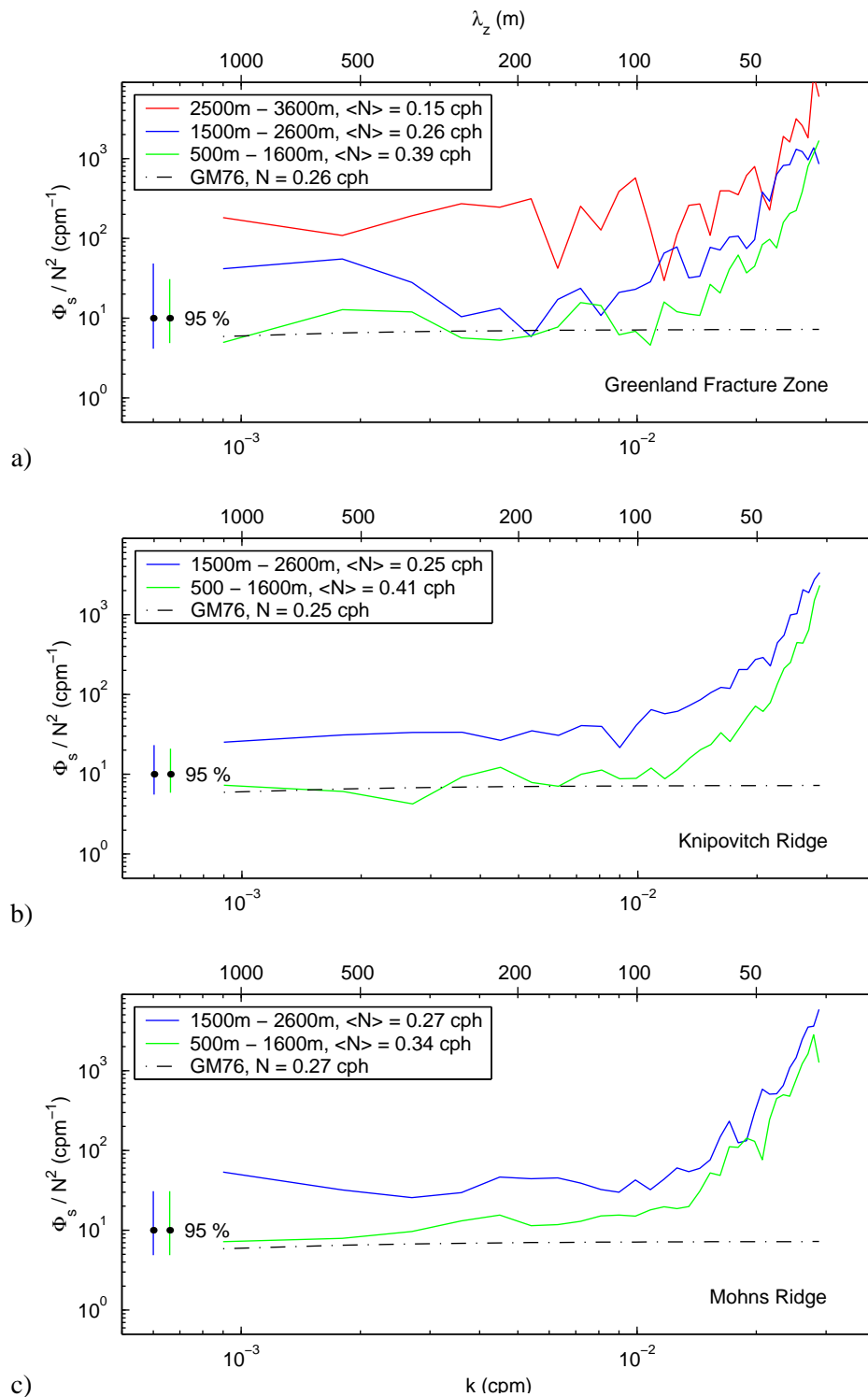


Fig. 4.14: Same as Figure 4.13, but for the rims of the Greenland Sea. a) Greenland Fracture Zone, average over 1/3/5 profiles in the deep/medium/shallow range, respectively. b) Eastern Greenland Sea and Knipovitch Ridge, average over 10 resp. 8 profiles in the shallow and deep depth range. c) Mohns Ridge, 5 profiles for both depth ranges. For locations, see Table 4.3.

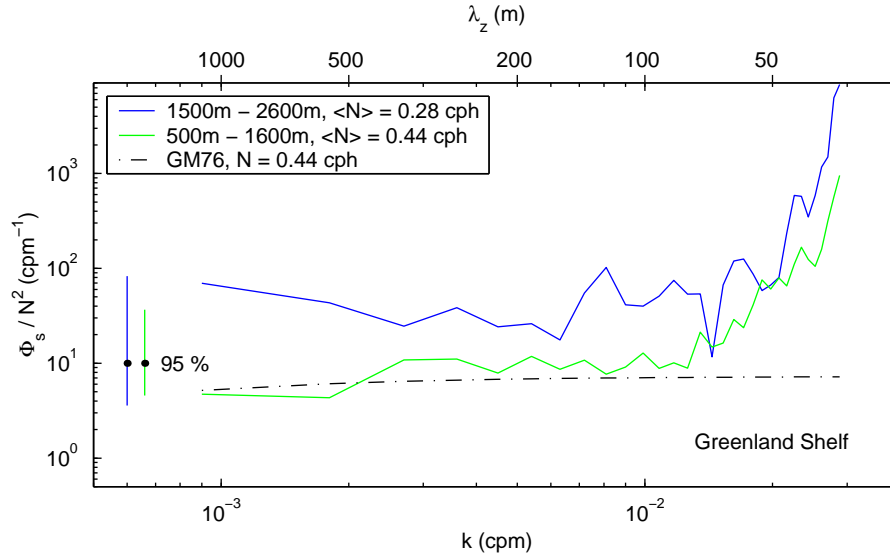


Fig. 4.15: Same as Figure 4.25, but for profiles close to the Greenland Shelf; average over 2 resp. 5 profiles for the deep and shallow depth range.

1999; Woodgate et al., 1999). This is, however, not the case. On the contrary, the low wavenumber spectral density is the lowest of all areas.

#### Noise

In all observed average spectra, there is an increase in spectral energy between 100 m and 60 m, the onset of which shifts towards higher wavenumber with depth. The most likely cause for such a rise is the instrument noise level of the LADCP measurements which can affect the spectral level at high wavenumbers. It depends on the strength of the backscattered signal, which is a function of the abundance of scatterers (i.e. zooplankton) in the watercolumn, and therefore decreases with depth (Figure 4.9a).

White noise in horizontal velocity translates to noise blue in shear as  $k^2$ . In a shear spectrum, noise accordingly reveals itself by a steep rise in spectral energy towards smaller wavelengths comparable to that observed in the shear spectra presented here. The onset of this rise is hard to detect, since the necessary spectral correction of the original measurements smears out the transition between signal and noise. Shear measurements from a complementary source would facilitate the noise detection, but are unfortunately not available.

Contradictory to the assumption of a noise increasing with depth is the fact that the onset of the rise apparently shifts towards higher wavenumbers with increasing depth: In the shallow layer above the salinity maximum it is typically found at wavenumbers around 0.01 cpm or below, in the upper deep water in the range  $0.01 \leq k \leq 0.0125$  cpm and at wavenumbers higher than 0.0125 cpm

in the deepest part of the water column. This shift is especially pronounced in the averages from the central Greenland Sea, and only to a lesser extent in the spectra from the rims. The increase of spectral energy with increasing depth possibly counteracts the decrease of backscatter signal, so that the net effect is an improved signal-to-noise ratio at larger depths.

Except from instrument noise, there is also evidence for another possible explanation for these observations. An indicator for an actual physical increase in variance in this wavenumber range is the similar spectral shape found in the corresponding spectra of vertical strain (cf. Figure 4.25), which stem from measurements with a much better vertical resolution and thus do not have to be corrected for attenuation in that wavenumber range. On the assumption of a more or less wavenumber independent shear to strain ratio, it is therefore reasonable to accept the rise at least partly as a heightened variance. Physically, blue shear spectra at high wavenumbers have been identified as the signal of bottom-reflected internal waves. These normally decay in the bottommost hundred meter of the water column (Eriksen, 1982), but similar enhancements up to a slope of  $k^2$  have been found in microstructure data from several hundred meters above the seafloor that were attributed to interaction with tidal currents and topography (Gregg and Kunze, 1991). A similar spectral shape is also evident in the shear spectrum derived from high resolution XCP measurements in the study of Polzin et al. (2002) (Figure 4.10 here), which also comes from data from an environment with rough topography, a fracture zone of the Mid Atlantic Ridge.

### 4.5.3 Shear Variances $\langle S^2 \rangle$

#### *Integration*

The use of shear variances for the determination of eddy diffusivities instead of energy levels or 10 m–shear is appropriate because of the limited vertical resolution of the LADCP measurements and the variation in the observed spectral shapes. The choice of the upper wavenumber limit for the integration to determine the variances holds some difficulty, though, namely (i) the determination of the cutoff wavenumber, (ii) the incorporation of as much of the signal as possible, and (iii) the exclusion of noise.

The canonical spectrum of vertical shear predicts a zero spectral slope for small wavenumbers with a transition towards the  $k^{-1}$  roll-off at a cut-off wavenumber of  $k = 0.1$  cpm. For the GM76 formulation, with a cut-off wavenumber of  $\beta_u = 0.63$  rad s $^{-1}$  (= 0.1 cpm), this leads to the relation

$$\langle S_{GM}^2 \rangle = \int_0^{\beta_u} \Phi_s d\beta = 0.7N^2 \quad (4.7)$$

(cf. Appendix A); in other words, the product of the cut-off wavenumber and the buoyancy scaled spectral level, the shear variance, should be a constant. This would require the cut-off wavenumber to shift towards lower wavenumbers for energetic spectra (Figure 4.16). Physically, such an energy

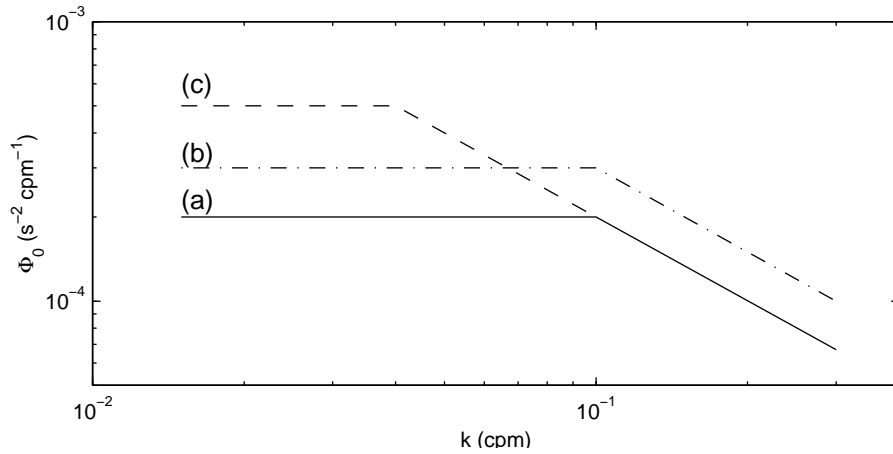


Fig. 4.16: Schematic representation of different models for the wavenumber dependency of shear spectra. a) Canonical model of Gargett et al. (1981) (cf. Section 2.1). The spectrum is flat at low wavenumbers and rolls off for  $k > k_0 = 0.1$  cpm as  $k^{-1}$ . b) The cutoff wavenumber  $k_0$  is independent of spectral energy density. c)  $k_0$  depends on the energy content of the low wavenumber part of the spectrum and rises towards higher wavelengths as  $\Phi_0$  increases.

density dependency of the cut-off wavenumber implies an upper limit of saturation for shear in an internal wave field, beyond which turbulent decay takes over. There is some observational evidence (e.g. Duda and Cox, 1989; Gregg et al., 1993; Kunze and Sanford, 1996) that a change of slope for energetic spectra indeed occurs at wavenumbers smaller than 0.1 cpm; but a consistent picture has not yet emerged.

The measurements presented here do not span the full wavenumber range up to 0.1 cpm caused by the inadequate vertical resolution of the shear data. If a transition of the roll-off range towards wavelengths larger than 50 m is present in the spectra presented here (Figures 4.13, 4.14), it is well masked by other effects (e.g. a possible noise onset). This poses the ambiguity of possible noise contamination of the variances versus an underestimation of the real signal by either choosing a too high or too low wavenumber limit for the integration.

Integration up to  $\lambda_z = 50$  m and alternatively to  $\lambda_z = 70$  m shows some scatter among the data. The resulting variances lie within a factor of four of each other, with  $\langle S_{70} \rangle$  more often smaller than  $\langle S_{50} \rangle$  than not, but no functional dependency as, e.g., a stratification or backscatter strength criterion, could be found. Employing an  $0.7N^2$  criterion as an upper integration limit complicates matters further in that, caused by the relatively high shear levels and the weak stratification in the deep water, such a limit restricts the wavenumber band for integration to very few data points.

As it is, there is no indication of an onset of roll-off in the resolved wavenumber band, and no sensible criterion for a limitation of the wavenumber band for integration could be found. Thus, following Polzin et al. (2002), variances were obtained by integrating the single shear spectra up to an upper boundary wavenumber  $\beta = 0.12$  rad  $m^{-1}$ , corresponding to a vertical wavelength of

$\lambda_z = 50$  m. This, however, may result in an overestimate of shear variance in the deepest part of the Greenland Sea, where  $\langle S_{50}^2 \rangle$  occasionally gets larger than  $0.7N^2$ . For a better comparability, the resulting shear variances are scaled with the appropriate GM variance  $\langle S_{GM}^2 \rangle$ , integrated over the same wavenumber band. Where the bottommost part of an ADCP profile with gaps from the bottom reflection is included in a variance estimate, the gaps were zero padded prior to analysis and the resulting data points have been marked in the figures.

#### Distribution of Variances

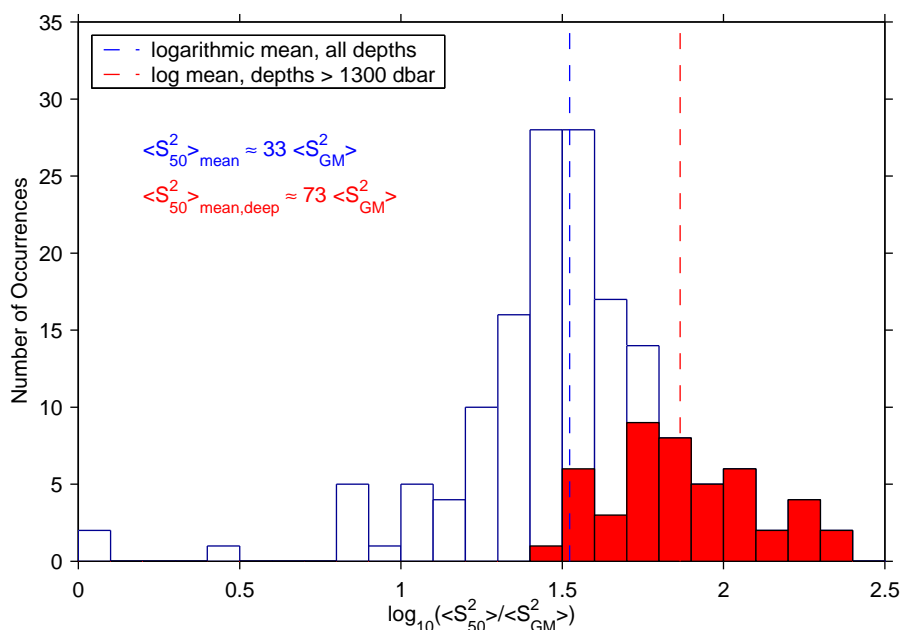


Fig. 4.17: Histogram of the distribution of GM76-scaled shear variances in the Greenland Sea. The unfilled bars include all available data points, while the red bars include only data from below 1300 m depth. Variances were calculated from 1100 m segments with a half segment length overlap (see Sections 4.5.1, 4.5.3); the underlying shear profiles reach from  $\approx 100$  m depth down to the first occurrence of bottom interference. Depicted is the base-10 logarithm of the scaled variances.

The magnitude of the resulting shear variances is shown in form of a histogram of the number of occurrences of the scaled variances (Figure 4.17). The distribution is roughly lognormal, but the numerical values are strongly elevated compared to the GM76 shear variances. The mean ratio between measured and GM76 shear variance is approximately 33, when all available data from all depths are included. If only data from depths greater 1300 m are considered, virtually all ratios are above the previous mean, with an average of approximately 73 times GM76.

The tendency for higher variances with depth is even more pronounced when the gap afflicted lower parts of the shear profiles are included (Figure 4.18): The resulting mean value for depths larger than 1300 m is almost doubled by the inclusion, and amounts to approximately 140 times

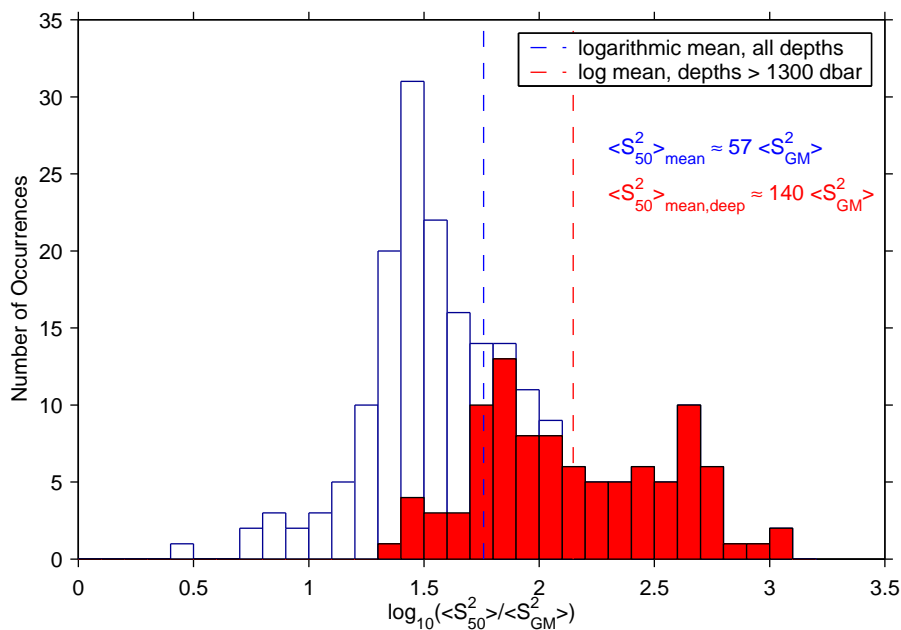


Fig. 4.18: Same as Figure 4.17, but including the sparse data between and below the bottom gaps; said gaps were filled with zeros for analysis.

the GM76 variance. While the distribution of shear variances without the near bottom data is more or less lognormal, inclusion of the data from the profile segments below the gaps distorts the distribution towards some sort of bi-modal shape (Figure 4.18). A tendency for this deviation from the normal distribution is already suggested when only the data from the deep water in Figure 4.17 are taken into account. Thus, the distortion may be caused by either by the unevenness of the sample distribution of the dataset, or it is simply a result of the higher errors in the gap affected data points.

The observed high values of scaled shear variance arise from the fact that the GM76 formulation depends on  $N^2$  (cf. Appendix A), and therefore predicts only a very low shear variance for weak stratification as can be found in the area considered here. Since the shear is not vanishing in the abyss, but increases again towards the bottom (cf. Figure 4.5), this leads inevitably to the large ratios found here.

The apparent depth dependence of the shear variance is best studied by depicting the vertical distributions. The vertical profiles of the GM76-scaled shear variances were obtained by overlapping the analysed segments with half the segment length, and assigning the resulting variance of each segment to the centre of the corresponding depth range. This procedure results in a vertical spacing of approximately 500 m, with a slight smoothing effect because of the overlap.

For the central Greenland Sea, vertical profiles calculated from 24 LADCP casts are presented in Figure 4.19. (The grouping of the profiles is the same as previously for the spectra, see Table 4.3.) The average profile is determined where at least two separate casts enter into the calculation. Vari-

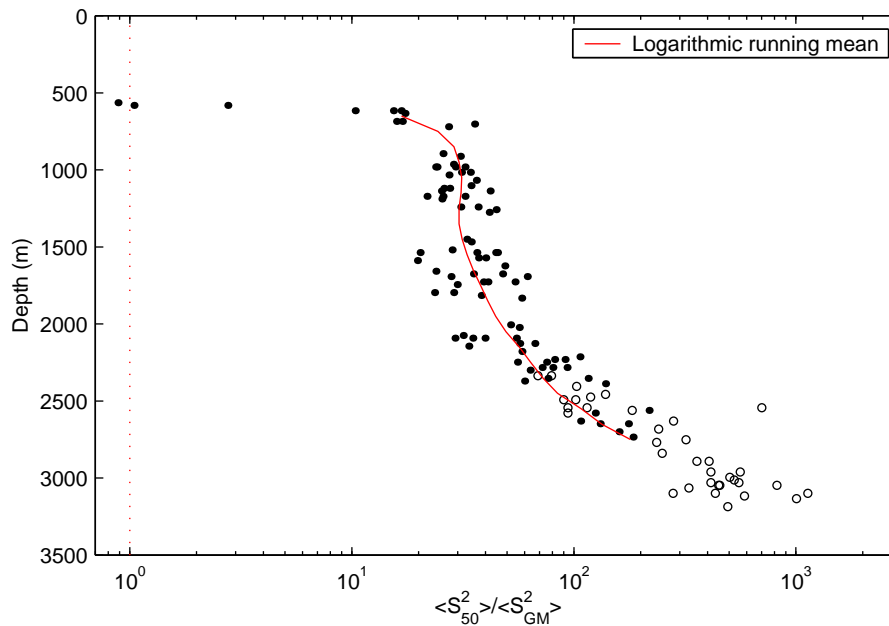


Fig. 4.19: Combined depth profiles of GM76-scaled shear variances for 24 shear profiles from the Greenland Basin (See Table 4.3 for locations). Also included is an average profile (red line, a running vertical mean from logarithmic means in depth bins), and the data from near the bottom below the data gaps (open circles) that are prone to larger instrumental errors (not included in the mean profile). Note that each data point represents a mean over 1100 m, centred at the location of the point.

ances that equal more or less the GM value, i.e. have a ratio of one, are only found in the uppermost of the analysed segments, centred between 500 and 600 m depth. For the depths below that up to values centred at 2300 m, there is little variation with depth; the values range from 20 to 50 times GM76. The largest scatter at one specific depth occurs around 1700 m, for those segments that include the deep water as well as the convectively renewed intermediate water. Below that, there is a dramatic increase towards higher ratios, with shear variances up to 100 times the GM values for data above the gaps. The variances that include the data from near the bottom pursue the same trend (with the exception of one extreme outlier), leading to maxima of 1000 times the GM shear variance. While those data are not included into the mean profile shown here, the transition seems smooth enough to justify the inclusion of the near bottom data into the further analysis.

The vertical distribution of the shear variances atop rough topography (Figure 4.20) does not exhibit a similar homogeneous layer up to mid depth, but a steady increase of variance from near-surface down to the bottom. The scatter of the data in any given depth is larger than in the central Greenland Sea. There are two possible reasons for this: Firstly, the profiles stem from a larger range of locations, with some degree of hydrographic variability. Secondly, the data points at any fixed depth originate from different vertical distances from the bottom because of their location above the ridge systems, and therefore different (higher) shear levels might be expected. An indication

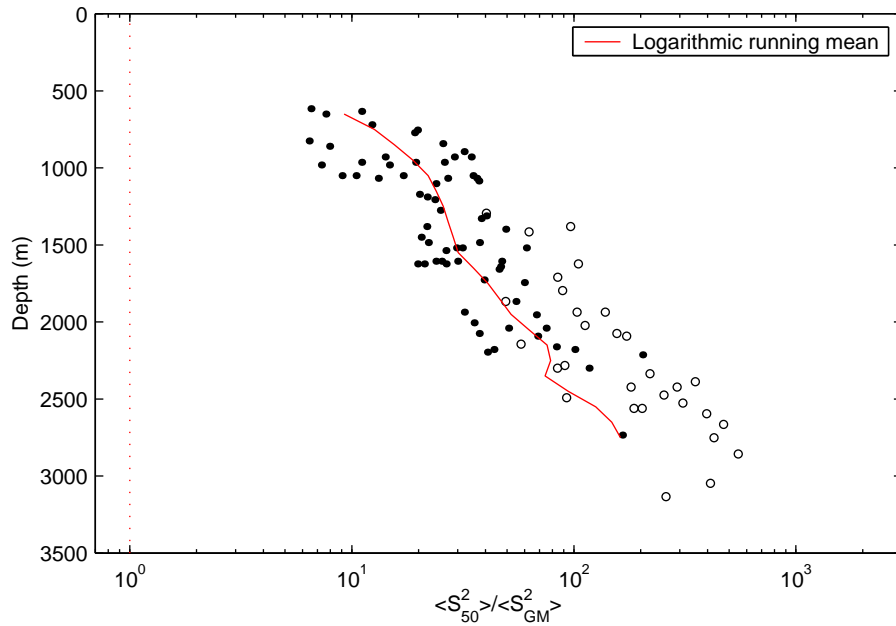


Fig. 4.20: Same as Figure 4.19, but for 27 shear profiles covering the area of Mohns Ridge, Knipovitch Ridge, and the Greenland FZ. Only profiles with waterdepths larger than 1300 m were included.

for this may be the fact that the data from the bottommost part of the shear profile are almost always larger than those from the open water in the same depth. The magnitude of the ratios in the deep water is comparable to that in the central Greenland Sea, but in the depths between 1500 and 2000 m, the ratios are higher; this points towards an elevated internal wave activity above the ridges in that part of the water column.

Closer inspection of the dependence on topography by horizontal mapping of the bottommost data (Figure 4.21) does not reveal any particular elevation of shear levels near the ridges compared to those from the Greenland Basin. While the shear levels are higher than those from the same depth in the open water, the proximity of rough topography obviously does not lead to exceptionally high shear variance. On the contrary, the highest values can be found in the centre of the Greenland Basin, where the seafloor is relatively smooth.

This surprising distribution is not confined to near-bottom variances; plotting the scaled variances versus height above sea bed instead of absolute depth (Figure 4.22) shows indeed that the variances in the centre of the Greenland Sea at any distance from the seafloor are higher than at any of the rim locations, in spite of the fairly rough topography. However, if elevated shear levels above the rough topography were confined to a layer much thinner than the 1100 m segments used for deriving the spectral estimate of the variances, it would not necessarily show up in the analysis. Instead, each centred variance represents a mean over the part of the water column corresponding to the analysed segment. Nevertheless, the fact that the highest levels are found in the interior is

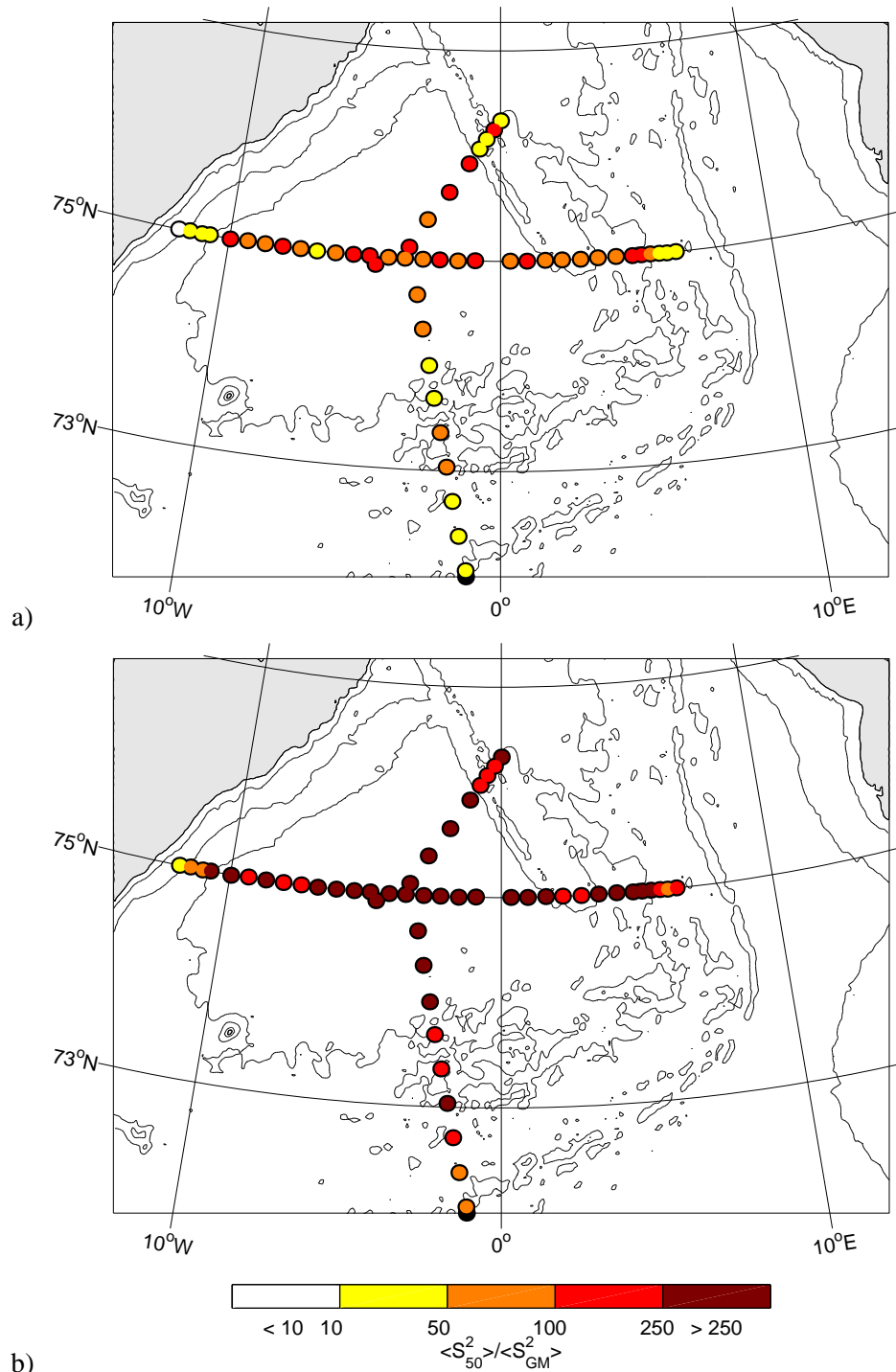


Fig. 4.21: Horizontal map of the GM76-scaled shear variances closest to the sea bed. a) Deepest 1100 m segments without data gaps, typically centred approximately 1000 m above bottom. b) Bottom-most 1100 m segments including the data below gaps, centred approximately at 600 m above bottom.

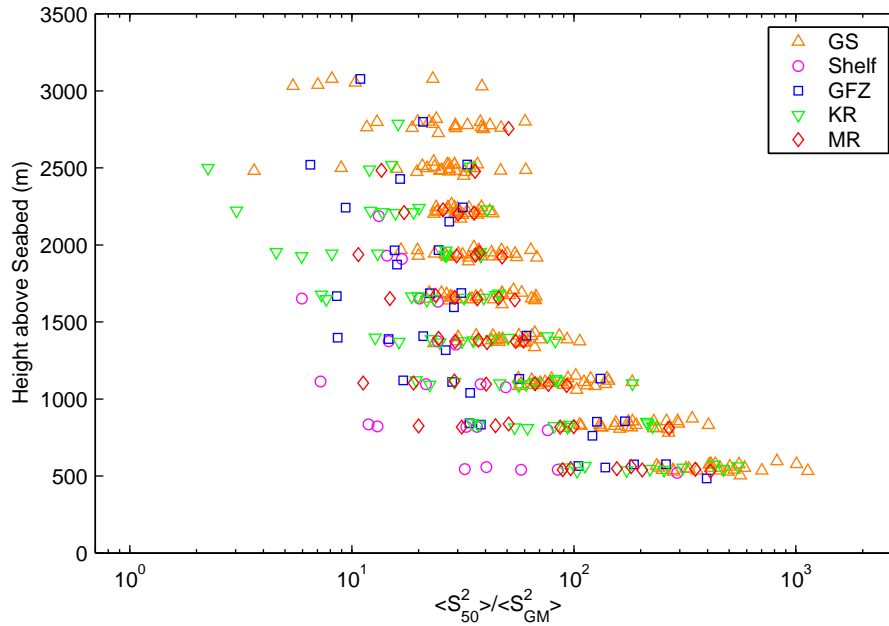


Fig. 4.22: GM76 scaled shear variances from various locations, plotted against distance from seafloor. The different areas are the same as for the spectra, and summarised in Table 4.3.

unexpected and will be investigated further.

#### *Error Assessment*

The estimation of an absolute or relative error of the shear estimates is difficult, since a lot of the partaking factors are hard to evaluate. The comparison with a complementing shear measurement technique with higher resolution would be ideal, but fails because of the absence of available data. However, Polzin et al. (2002) have attempted a systematic comparison between the results of LADCP and XCP shear measurements, with the ultimate goal to compute eddy diffusivities. They utilised a dataset from near the Charlie–Gibbs Fracture Zone in the North Atlantic, which is an environment comparable to the Greenland Sea in that it also is a deep ocean site that exhibits a weak stratification.

They found an agreement of shear-variance inferred diffusivities within a factor of two between both data sources, with a slight tendency for the ADCP diffusivities to exceed those derived from the XCP (their Figure 13). This prerequisites the use of the same integration limits for both, and prior application of the aforementioned spectral transfer function to the LADCP shear spectra. They concluded from their results, that the determination of eddy diffusivities by means of shear spectra measured with Lowered ADCPs is accurate within a factor of 3 to 4 (Polzin et al., 2002), and, while not as precise as microstructure measurements, is nevertheless a useful tool. A somewhat similar study was conducted by Dengler (2000) for data from the Indian Ocean. He compared spectra of

LADCP shear and velocity to spectra from a free-falling velocity probe (Pegasus), and arrived at similar encouraging results.

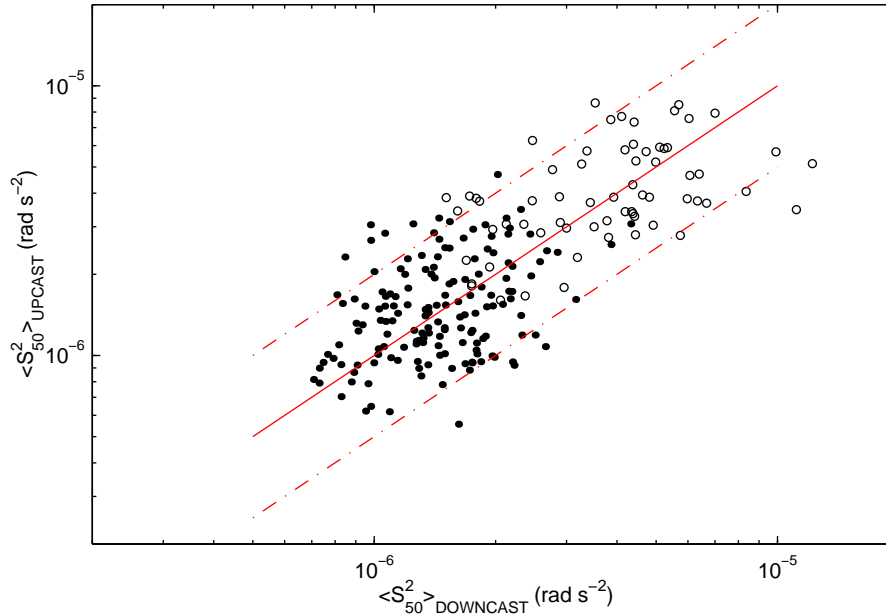


Fig. 4.23: Shear variance computed from upcasts versus shear variance from downcasts of the same profile. The red line identifies a ratio of one. Most data pairs lie within a factor of two of each other (red dash-dotted lines).

The robustness of the determination of the shear variance in this study can be tested by comparing results from the up- and downcast of the same LADCP profile (Figure 4.23). There is a reasonable agreement between the data pairs, they lie within a factor 2 of within each other. Even the pairs from the gap afflicted lowermost parts of the profiles, which are expected to have larger error bounds, exhibit the same good correspondency. This factor two of accuracy represents an upper limit, since the shear estimates from the upcasts (which are not used for the further analysis) rely only on 2/3 of the data for each estimate because of the higher package velocity. They are therefore subject to larger errors and and to a great deal responsible for the scattering of the data pairs. The accuracy in shear variance leads to a factor of 4 in the diffusivity estimate, which is in good agreement with the method accuracy given by Polzin et al. (2002).

To summarise, an over- or underestimation of the shear variance can originate from two sources: the error of the determination of variances from the resolved part of the LADCP shear spectra (by inclusion of noise), and the error made by the (necessary) limits of the integration (50 m wavelength instead of 10 m) and the unknown shape of the spectrum in the missed part. The latter can be estimated roughly by assuming upper and lower limits for the trend of the shape; this was done e.g. by Dengler (2000) and amounts (again) to a factor of two for a shear spectrum of GM energies, but gets smaller for more energetic spectra. In the present study, with the uncertain rise in spectral

density towards higher wavenumbers, an overestimate of the variance is more likely than an underestimate. Thus, the real variance will lie within an underestimate of a factor two (uncertainty from the integration) and an overestimate of a factor of four (integration error plus possible overestimate of the unknown part of the spectrum). This error bounds translate into corresponding accuracies of the derived diffusivity estimates of four and 16, for an under- or overestimate, respectively.

#### 4.6 *Shear/Strain Ratios*

In the same way as the shear variance can be interpreted as a proxy for the horizontal kinetic energy, the variance of strain corresponds to the available potential energy. Strain itself describes the approaching and withdrawal of individual isopycnals to each other associated with internal wave displacement. For the estimation of dissipation rates in non-GM wave fields, it has been proven useful to account for a possible distortion of the internal-wave aspect ratio (Polzin et al., 1995). This can be approximated by the ratio of the buoyancy-scaled shear variance to the strain variance, the shear/strain ratio.

##### 4.6.1 *Strain Spectra*

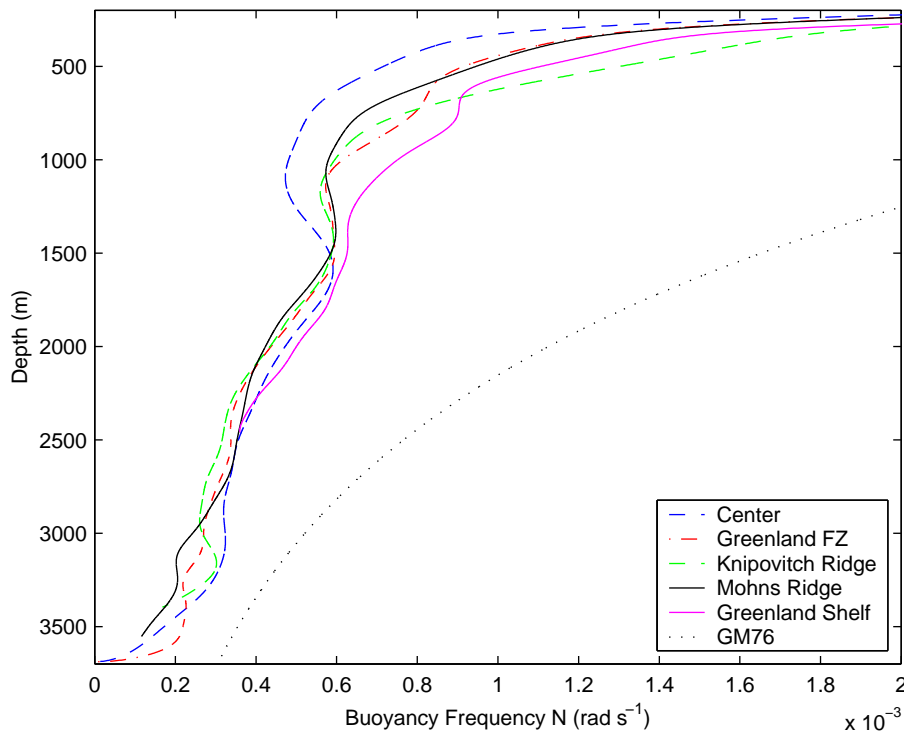


Fig. 4.24: Mean smoothed profiles of buoyancy frequency as used for the computation of the displacement spectra. The black dotted line represents the GM76 stratification as described Appendix A.

The vertical displacement  $\zeta$  of a local density surface is given by the difference between a local density and the background density, scaled with the background density gradient. This takes the form

$$\zeta = -\frac{\overline{\sigma_\theta}(z) - \sigma_\theta(z)}{\partial\sigma_\theta/\partial z}, \quad (4.8)$$

where overbars denote a spatial mean, and  $\partial\sigma_\theta/\partial z$  is derived from a 400 m smoothed mean profile of  $N^2$  (Eriksen, 1981).

The domain of the Greenland Sea was divided into five groups of stations, the central Greenland Sea, the Greenland Fracture Zone in the north, the Knipovitch Ridge in the east, the Mohns Ridge in the south and the Greenland shelf break in the west (These are the same groups as used for the shear analysis, Table 4.3). For each group, a separate mean density profile and a smoothed mean buoyancy frequency profile were computed from the 1-dbar CTD data. The smoothed buoyancy frequency profiles are depicted in Figure 4.24:  $N$  is generally very small, and the main differences between the groups occur between 200 and 1500 meter depth, the range that is affected by winter-time convection in the centre and dominated by Atlantic inflow at the rims. Vertical displacements were then calculated for the individual profiles according to Equation 4.8. The profiles of vertical displacement were divided into 1024 m segments prior to Fourier analysis; this was done to match the length of the profile segments from the shear analysis. Following that, the spectrum of vertical strain  $\Phi_\lambda$  was derived from the displacement spectrum  $\Phi_\zeta$  using the relation

$$\Phi_\lambda(\beta) = \beta^2 \Phi_\zeta(\beta). \quad (4.9)$$

Similarly to the previous section, in the following average spectra are presented for the different areas of the Greenland Sea. The profiles were again divided into three vertical ranges; the upper one ( $\approx 500$ – $1500$  m) roughly corresponding with the domain of the intermediate water masses formed by convection and the Atlantic inflow. The two deeper ranges both span the GSDW.

The spectra from the central Greenland Sea (Figure 4.25) exhibit qualitatively different wavenumber dependencies for the different depth ranges. In contrast to the shear spectra, the minimum of energy density is found in the intermediate depth range between 1500 and 2500 m. There is no flat level for large wavenumbers, but a rise approximately as  $k^{-1}$  for wavelengths between 500 and 20 m. For wavelengths smaller than that, the rise steepens up to the high wavenumber cut-off at  $\approx 0.15$  cpm. The cut-off is also notable for the deep range and, to a lesser extent, for the shallow spectrum, but is superimposed by noise for wavelengths smaller than 5 m.

The spectrum for the deepest range is for wavelengths smaller than 100 m somewhat similar in shape to the intermediate one, but more energetic. For wavenumbers lower than 400 m, the power spectral density for both is approximately that of the GM spectrum. The most outstanding feature of the deepest spectrum is the high spectral density in the wavenumber band between 0.015 and 0.003 cph (with a spectral peak at 0.005 cpm), where it departs dramatically from the shape of the

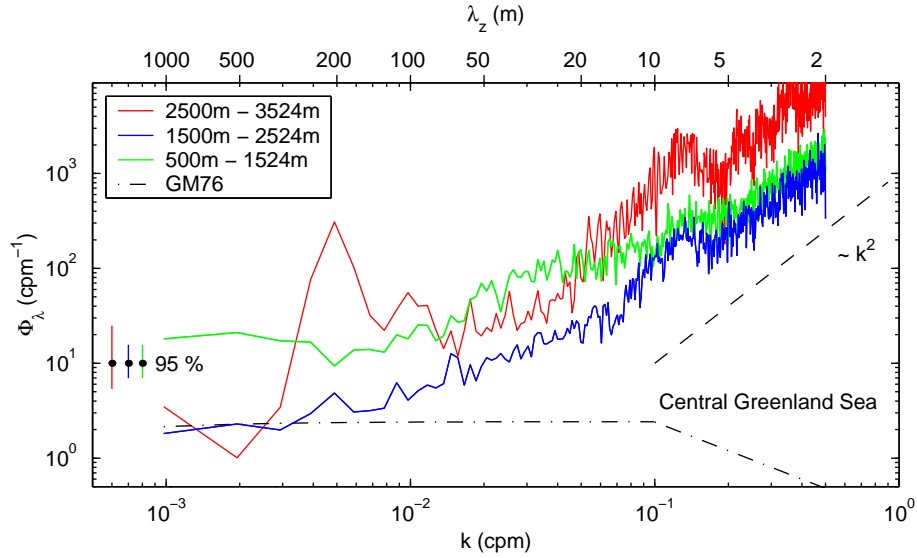


Fig. 4.25: Average strain spectra from the central Greenland Sea for 3 different depth ranges, containing 1/3/5 profiles in the deep/medium/shallow range, respectively. The incorporated profiles and depth ranges are the same as for the shear spectra (cf. Table 4.3, Figure 4.13). The GM76 spectrum is shown for  $\bar{N} = 0.16$  cph, corresponding to the deepest range; the GM76 spectra for the other depth ranges differ only slightly in the low wavenumber range.

intermediate spectrum as well as from the GM76 prediction. This is an indication of the presence of coherent structures in this spectral band, and not consistent with the view of the spectrum as a realisation of a statistical wave field. The wavelength of those structures reflects the ribbon-like structures found in the transect of buoyancy frequency (cf. Figure 4.2), but the physical reason for those is unclear.

The average spectrum for the upper layer shows the largest differences to either of the strain spectra from larger depths: In contrast to the corresponding shear spectra from the area (Figure 4.13), the spectral density is the highest of all depth ranges. It is elevated almost an order of magnitude for low wavenumbers as compared to the GM76 spectrum, and rises further for wavelengths smaller than 60 m. This increase of spectral energy towards smaller scales has been identified as a sign of the presence of vortical modes by Polzin et al. (2003); vortical modes (low-aspect-ratio subinertial density finestructure) have been reported to be generated by convection, e.g. in the Labrador Sea (Lilly and Rhines, 2002).

At all depths, the  $k^2$ -rise for high wavenumbers indicates an increasing influence of noise, notably for wavelengths below 5 m. This is caused by the small signal-to-noise ratio in the measurements of the density gradient, and also evident in the spectra from the other areas. It should nevertheless not pose a problem for the calculation of the variances, because the integration is limited to 50 m wavelength as for the shear variances.

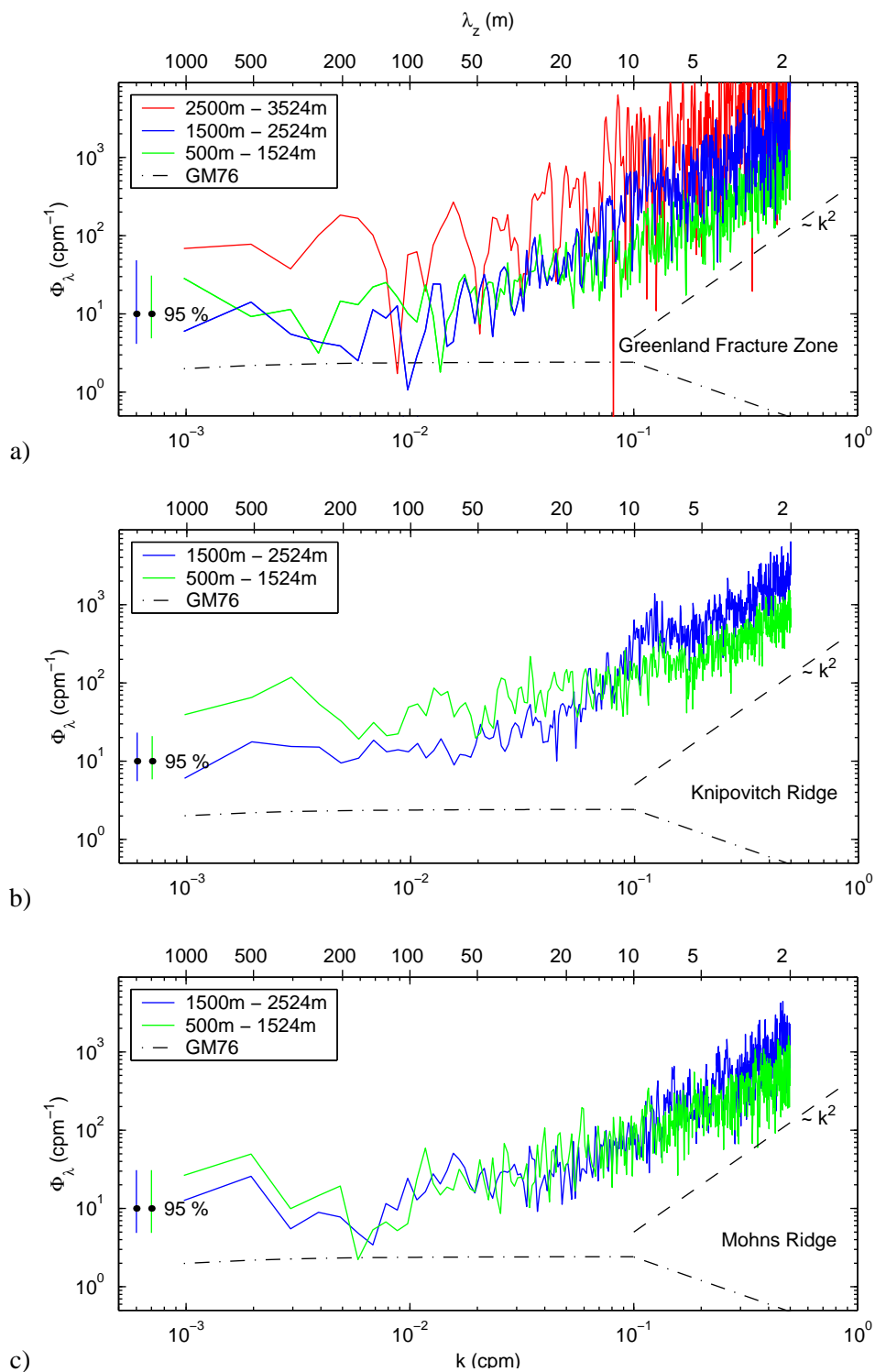


Fig. 4.26: Same as Figure 4.25, but for the rims of the Greenland Sea. a) Greenland Fracture Zone, average of 5 shallow, 3 intermediate and 1 deep profile(s); GM76 shown for  $\bar{N} = 0.26$  cph. b) Eastern Greenland Sea and Knipovitch Ridge, average of 10 shallow and 8 deep profiles, GM76 for  $\bar{N} = 0.25$  cph. c) Mohns Ridge, 5 profiles for both depth ranges, GM76 for  $\bar{N} = 0.27$  cph. For locations, see Table 4.3.

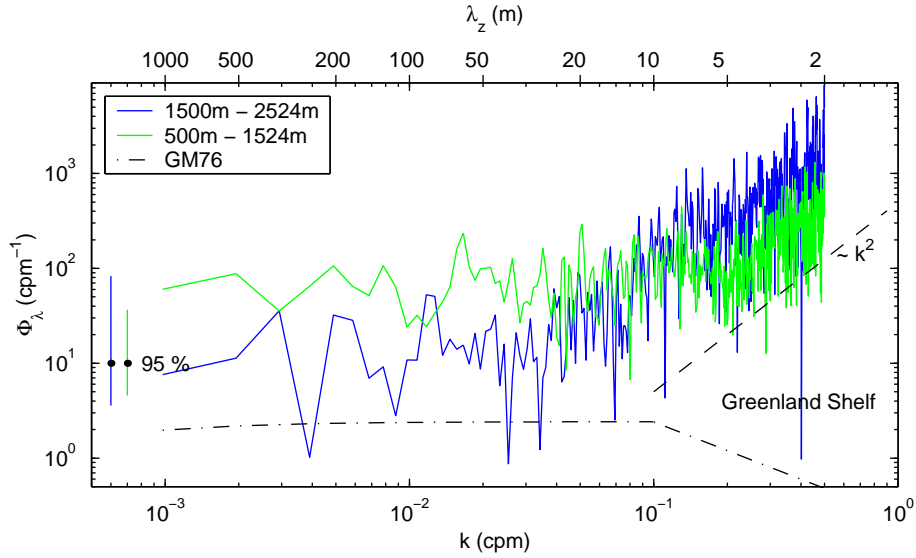


Fig. 4.27: Same as Figure 4.25, but for the Greenland Shelf, average over 5 shallow and 2 deep profiles. The GM76 spectrum is shown for  $\bar{N} = 0.28$  cph, corresponding to the range from 1500 m downward.

The groups of profiles from the rims of the Greenland basin (Figures 4.26, 4.27), exhibit more variability in strain than was found in shear. Sufficiently covered in all the locations were only the upper two depth ranges; a single spectrum from the deepest range of the GFZ area was included for comparison (Figure 4.26a). The spectra from intermediate and shallow depth range of the GFZ have very similar shapes and spectral densities. They are both more or less white for wavelengths smaller than 100 m, and rise approximately as  $k^{1.5}$  beyond that. The spectral density in the wavenumber band between 0.02 and 0.001 cpm is roughly 5 times GM76 between 1500 and 2500 m, and slightly higher for the shallow range average. The single deep spectrum is more energetic than the two averages, and white for all wavelengths larger than 30 m, but exhibits a lot of variability, especially for  $200 \text{ m} \leq \lambda \leq 50 \text{ m}$ .

The spectra from the eastern and western rim (Knipovitch Ridge, Figure 4.26b, and Greenland shelf, (Figure 4.27) are very similar to each other. As in all the other locations, the averages from intermediate depth are the least energetic, albeit well above the GM76 level. The spectra from the shallow depth ranges here exhibit the highest spectral densities ( $\approx 20 \times \text{GM76}$ ) of all observations. They are white for all wavelengths larger than 50 m, and only a very moderate positive slope for wavelengths smaller than that. The intermediate spectra on the other hand, show an increase in spectral density towards higher wavenumbers very similar to that in the central basin; this is more pronounced in the spectrum from Knipovitch Ridge than in the one from the Greenland shelf. The two average spectra from the southern edge of the gyre are almost identical. They show high ( $\approx 10 \times \text{GM76}$ ) spectral densities for wavelengths larger than 400 and smaller than 100 m, and a minimum in between, at approximately 150 m wavelength.

## 4.6.2 Ratios

Given the horizontal and vertical variability of the strain spectra and the apparent depth and wavenumber dependence of the relation between the shear and the strain spectra, it is particularly important to consider the shear/strain ratio when estimating dissipation rates.

The shear/strain ratio (Equation 2.9) of the measurements presented here is to some degree dependent on the wavenumber; this is a departure from the GM description, which can be shown to have a wavenumber independent ratio of 3 (see Appendix A). However, for the purpose of calculating the dissipation, a possible wavenumber dependency is neglected, and the ratio is calculated from the variance of measured shear divided by the variance of measured strain times the buoyancy frequency as

$$R_\omega = \frac{\langle S_{50}^2 \rangle}{N^2 \langle \lambda_{50}^2 \rangle}, \quad (4.10)$$

where both variances are obtained by integrating the spectra up to the same upper wavenumber limit, here corresponding to a wavenumber of 50 m as denoted by the subscript. The calculation was done using spectral estimates of shear and strain variances over the same depth range of approximately 1100 m, and the mean buoyancy frequency over the corresponding depth interval.

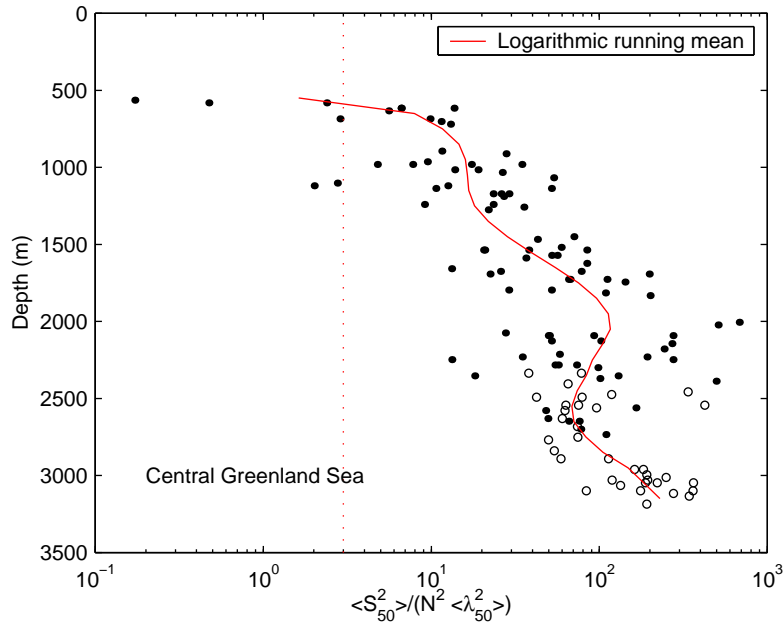


*Fig. 4.28:* Shear to strain ratios for the 24 profiles from the central Greenland Sea. The red line denotes the logarithmic mean calculated for 100 m depth bins. The red dotted line marks the ratio of a GM76 wave field. Note that each data point represents the mean over 1100 m, centred at the location of the point.

The detailed pictures of the vertical distribution of the ratios as given in Figures 4.28 and 4.29 for the central Greenland Sea and the rims, respectively, show that the occurrence of low

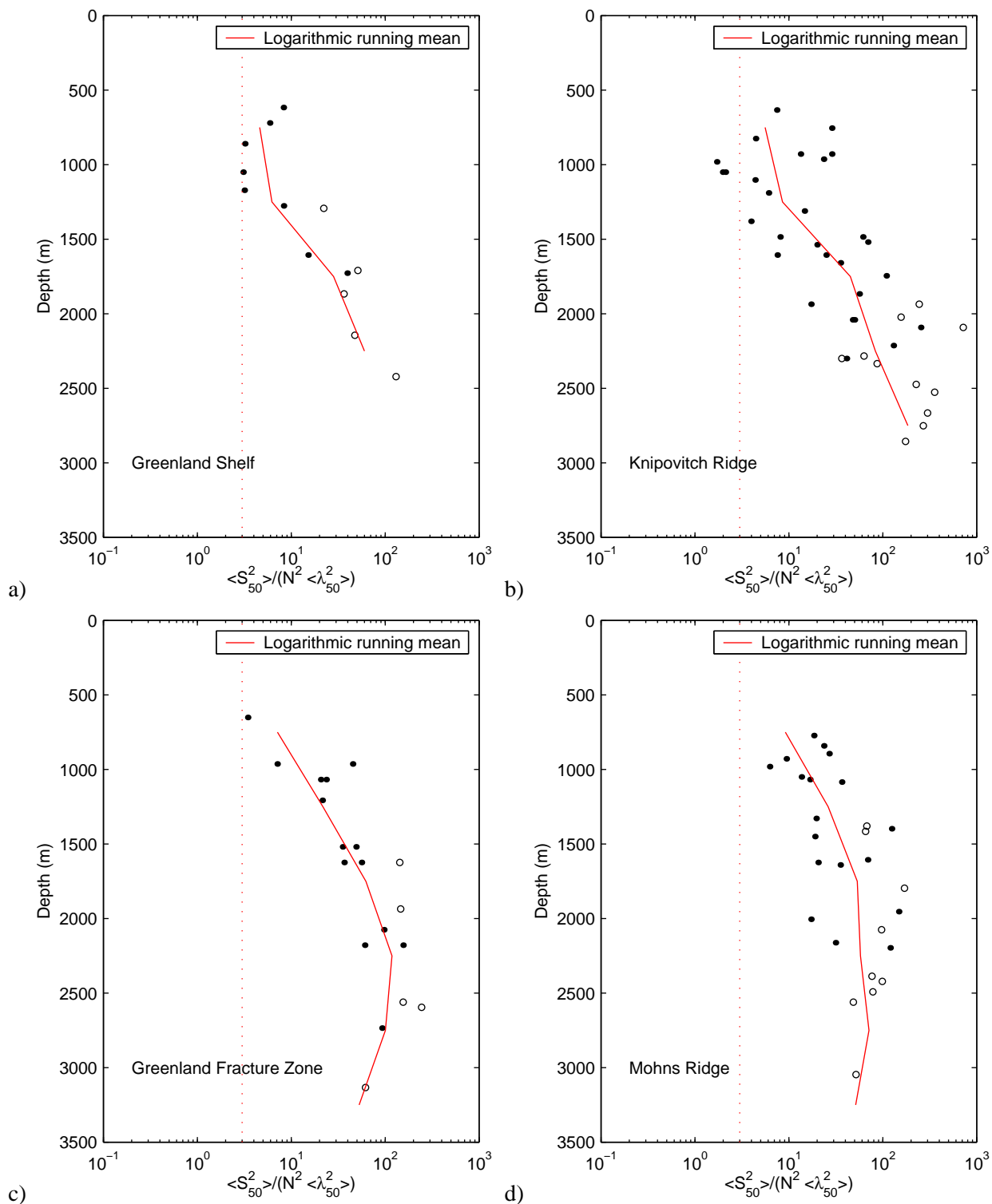


Fig. 4.29: Same as Figure 4.28, but for groups of profiles from the rims of the Greenland Sea. The mean profiles were calculated for 500 m depth bins.

shear/strain ratios below the GM value of 3 (and very occasionally below one) is confined to the uppermost parts (segments centred approximately between 600 and 700 m depth) of the profiles. For the most part, the ratios are in the order between ten and one hundred. All profiles, from the centre as well as from the rims, exhibit a general tendency for the shear/strain ratio to increase with depth up to 2000 to 2500 m; below that, the shape of the  $R_\omega$  profiles is more diverse.

In the central Greenland Sea, the ratios rise from the GM-like values to numbers between 10 and 20 for the layer of convectively ventilated water down to 1500 m, and further towards the maximum on an average of 100 for segments centred at 2000 m. Below, the profiles exhibit a local minimum (mean ratios around 70) at 2600 m and rise again towards the bottom. The largest singular ratios (for some of the profiles up to 500) are found above this local minimum; at the bottom, values of 300 to 400 are reached. At any given depth, the individual values scatter in a range of approximately an order of magnitude, with the exception of the deepest parts in the centre, below 2600 m.

The situation at the rims is qualitatively different in that the single profiles as well as the averages show different depth dependencies from location to location. While the average profiles from the eastern and western rims (Knipovitch Ridge and Greenland shelf) exhibit a steady increase from GM-like values at the top to mean ratios of 100 (GS) and 400 (KR) near the bottom, the average profiles from the Greenland Fracture Zone in the north and the Mohns Ridge in the south rise towards an intermediate maximum and decrease again towards the bottom. However, the maximum is located at depth that are not exceeded in the east and west, and the decrease of the mean at depth is based only on one or two profiles, respectively. Thus, the absolute position of the maximum is not entirely different for all groups of profiles, and concurs with the upper part of the deep water.

The shear to strain ratios exhibit significant departures from a GM-like behaviour in large parts of the Greenland Sea, especially in the deeper parts, where shear is elevated and stratification is weak, resulting in ratios up to two orders of magnitude larger than the canonical GM value of 3. The (relatively) small shear/strain ratios occasionally occurring in the upper layer are possibly a signature of shear instabilities (Kelvin-Helmholtz billows or vortical modes, e.g. Polzin et al., 2003), and therefore remnants of the shallow convection in winter.

The large values of the ratio indicate that the intrinsic frequency of the waves approaches the inertial frequency (cf. Equation 2.9), which results in a dominance of horizontal in contrast to vertical motion, and hence more energy in shear than in strain. The amplification of relative importance of horizontal motion at greater depths and below the stability maximum is a sign of the dominance of near-inertial motions in the internal wave band, and probably caused by an increased impact of internal tides, which have frequencies very close to the inertial frequency in the Greenland Sea. This will be further discussed in Chapter 5.

## 4.7 Dissipation and Turbulent Diffusivity

### 4.7.1 Dissipation Estimates from Shear Variances & Inferred Diffusivities

The dissipation rate  $\epsilon$  was calculated using the shear parameterisation of Gregg (1989) which employs the shear variances and accounts for the shear/strain ratio as described above. The latitude dependency of the dissipation as included in Equation 2.10 demands some closer enquiry.

#### *Latitude Dependency of the Dissipation Rate*

The  $f$ -scaling which is commonly included into the calculation of the turbulent dissipation rate would add an additional factor of  $f(75^\circ)/f(32.5^\circ) \approx 2$  to the estimate at the latitude of the central Greenland Sea. However, the complete term for the latitude dependency of the internal wave field (caused by Doppler shift proportional to changing aspect ratios) as predicted by the HWF model (Henyey et al., 1986) amounts to

$$L(lat, N) = \frac{f \cosh^{-1}(N/f)}{f_0 \cosh^{-1}(N_0/f_0)} \quad (4.11)$$

i.e. it depends not only on the inertial frequency  $f$  but also on the buoyancy frequency  $N$ . In most regions of the ocean, where the ratio  $N/f$  is large, the latter term is adequately approximated by  $f/f_0$ ; but for the deep Greenland Sea, where the buoyancy approaches the inertial frequency,  $L$  may go down to 0.5 or less (Figure 4.30).

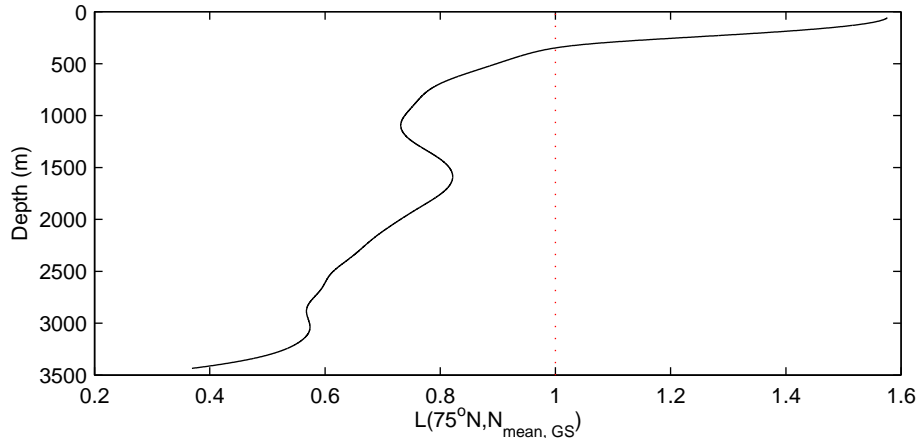


Fig. 4.30: Evaluation of Equation 4.11 for  $f$  at  $75^\circ\text{N}$  and a mean profile of  $N$  in the central Greenland Sea (cf. Figure 4.24).

Whether the HWF model gives correct predictions of the latitude dependency of the internal wave field or not is still subject to ongoing research (e.g. Gregg et al., 2003), but the reduction of Equation 4.11 to a factor of  $f/f_0$  is clearly not valid in the Greenland Sea. Thus, the scaling will not

be used in the following for the determination of dissipation and diffusivity. This omission may lead to an underestimate of dissipation (and diffusivity) of up to a factor two in the upper few hundred meters, and likewise an overestimate of the same magnitude in the deep water (cf. Figure 4.30). However, given the lacking evidence for the validity of the latitudinal scaling in general and its special problems in the Greenland Sea, the error from leaving out the scaling is most likely smaller than the one which would result from the application.

### *Eddy Diffusivities*

The computation of the diffusivities was done by substituting Equation 2.10 into Equation 2.13, thus eliminating the explicit  $N$  scaling. The possible latitude dependency was neglected on the ground described above, yielding

$$K_\rho = K_0 \frac{\langle S_{50}^2 \rangle^2}{\langle S_{GM}^2 \rangle^2} F(R_\omega) \quad (4.12)$$

with  $K_0 = \Gamma \epsilon_0 / N_0^2 \leq 0.06 \times 10^{-4} \text{ m}^2 \text{ s}^{-1}$  (cf. Section 2.2). The shear variance  $\langle S_{50}^2 \rangle$  used for the estimate of the diffusivities as well as the dissipation rates was computed by integration of the shear spectra for wavenumbers up to  $0.12 \text{ rad m}^{-1}$  (wavelengths larger 50 m), as described in Section 4.5.3; the adjustment for the shear to strain ratio  $F(R_\omega)$  is employed as described below.

Note: The (common) use of a mixing efficiency of  $\Gamma = 0.2$  is strictly appropriate only for high Reynolds number turbulence, i.e.  $N$  should not be much smaller than the velocity shear in the vertical. Thus, the mixing efficiency (which hinges on the possible buoyancy loss) might be smaller in an already weakly stratified environment, and a given dissipation therefore results in a smaller eddy diffusivity. The aforementioned condition may be violated locationally in the deep basin of the Greenland Sea (cf. Section 4.3); in other words, the assumption of  $\Gamma = 0.2$  gives only an upper boundary of the estimate of the eddy diffusivity, which likely presents an overestimate in some areas of the abyss.

### *Effect of Shear/Strain Correction*

The correction for a possibly distorted aspect ratio of the internal wave field  $F(R_\omega)$  is determined according to Equation 2.11 from the ratio of shear to strain; mean values for these ratios in different areas and depth ranges are listed in Table 4.4. It should be noted that since shear/strain ratios in theory cannot drop below one for hydrostatic internal waves, Equation 2.11 and the dissipation parameterisation hold only for ratios above unity. A shear/strain ratio of 1.01 was substituted for the calculation in the rare cases where the actual measured ratio undercut the limit. The use of an average buoyancy frequency over a range greater than 1000 m where it varies rapidly (cf. Figure 4.24) in the calculation results an additional smoothing effect on  $F(\omega)$ , therefore the resulting

dissipation rates for the upper layer should be interpreted with care.

The correction term  $F(R_\omega)$  has no large effect (relative to the accuracy of the method) on the dissipation and eddy diffusivity estimates for depths up to 1500 m, where it is generally close to one. For most parts of the deep water, however, the average of the correction is approximately 0.1, thus lowering the resulting dissipation and diffusivity estimates by an order of magnitude. A small number of the estimates is heightened by the correction term, because the ratio of shear to strain approaches or undercuts the GM76 value only at shallow depths in some locations (Figures 4.28 and 4.29). Generally, the inclusion of the distortion of the wave field results in a more homogeneous distribution of dissipation and diffusivity.

#### 4.7.2 Spatial Variability

The large variations of shear, stratification, and the resulting average turbulent dissipation rates and eddy diffusivities for the different areas and depth ranges are summarised in Table 4.4. The details of the vertical and horizontal distributions will be discussed in the following, with emphasis on the presentation of distributions of eddy diffusivities as a measure for mixing.

Tab. 4.4: Mean dissipation rates  $\epsilon$  and eddy diffusivities  $K_\rho$  for the different areas and depth ranges of the Greenland Sea. Also given are the corresponding buoyancy frequencies  $N^2$ , GM76 scaled 50 m shear variance  $S_{50}^2$  and shear to strain ratios  $R_\omega$ . The diffusivities in brackets denote the values one standard deviation away from the logarithmic mean. For the number of profiles and positions of each group, see Table 4.3.

| Location | Depth Range<br>(m) | $N^2 \times 10^{-7}$<br>( $\text{rad}^2 \text{ s}^{-2}$ ) | $S_{50}^2$ | $R_\omega$ | $\epsilon \times 10^{-9}$<br>( $\text{W kg}^{-1}$ ) | $K_\rho \times 10^{-4}$<br>( $\text{m}^2 \text{ s}^{-1}$ ) |                   |
|----------|--------------------|---|------------|------------|---|--|-------------------|
| GS       | 500–1600           | 2.94  | 30.8       | 16.2       | 2.23  | 14.9   | (8.7, 25.4)       |
|          | 1500–2600          | 2.41  | 47.0       | 117.8      | 1.42  | 11.6   | (5.8, 23.2)       |
|          | 2500–3600          | 0.83  | 416.0      | 167.4      | 34.42   | 809.0  | (477.7, 1370.1) * |
| GFZ      | 500–1600           | 4.65  | 16.0       | 16.1       | 0.93  | 3.9  | (2.4, 6.4)        |
|          | 1500–2600          | 2.16  | 37.9       | 69.5       | 1.09  | 9.9  | (5.5, 17.7)       |
| KR       | 500–1600           | 5.29  | 17.8       | 5.6        | 2.86  | 10.6   | (5.7, 19.9)       |
|          | 1500–2600          | 2.07  | 77.1       | 82.9       | 3.98  | 37.7   | (19.2, 74.0) *    |
| MR       | 500–1600           | 3.98  | 32.1       | 20.8       | 2.72  | 13.4   | (7.8, 23.1) *     |
|          | 1500–2600          | 2.30  | 65.4       | 55.8       | 3.89  | 33.2   | (14.4, 76.5) *    |
| SHELF    | 500–1600           | 6.17  | 15.8       | 3.4        | 3.51  | 11.2   | (6.6, 18.9) *     |
|          | 1500–2600          | 2.53  | 47.1       | 41.5       | 2.53  | 19.9   | (11.8, 33.6) *    |

\* Estimates in this layers include shear data below bottom gaps

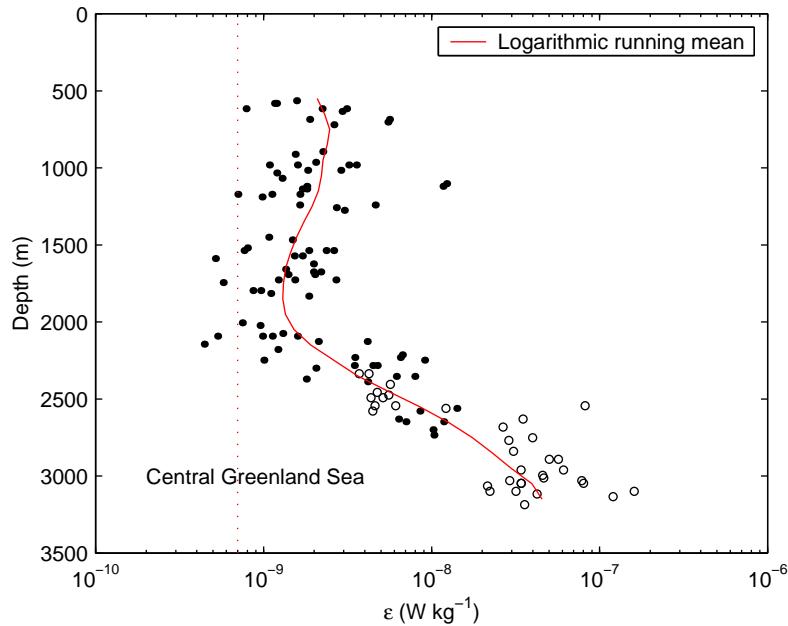


Fig. 4.31: Turbulent dissipation rates  $\epsilon$  for the 24 profiles from the central Greenland Sea. The red line denotes the logarithmic mean calculated for 100 m depth bins. The red dotted line marks the dissipation rate  $\epsilon_{HWF}$  (Henyey et al., 1986) of a GM wave field. Note that each data point represents a mean over 1100 m, centred at the location of the point.

### Turbulent Dissipation Rate

The resulting dissipation rates are not unusually high for most parts of the gyre. The range of the individual values encompasses more than two decades, with  $\epsilon$  spanning from  $0.5 \times 10^{-9} \text{ W kg}^{-1}$  towards maxima occasionally exceeding  $10^{-7} \text{ W kg}^{-1}$  near the bottom. The smallest as well as the largest of those numbers can be found in the central Greenland Sea (Figure 4.31). At the rims of the basin (Figure 4.32), the profiles cover a smaller range and have a less pronounced vertical structure.

The models of energy flux through the internal wave spectrum predict a dissipation rate proportional to the squared buoyancy frequency and the squared spectral energy level (cf. Section 2.2). If the ocean were in an equilibrium as stated by the GM description, the energy level (and therefore the shear variance) would decrease with decreasing stratification, and resulting dissipation should be more or less depth independent ( $\epsilon_{HWF} \approx 7 \times 10^{-10} \text{ W kg}^{-1}$  (Henyey et al., 1986), as indicated in Figures 4.31 and 4.32). For many areas in the open ocean it is instead expected to find a depth independent distribution of shear, resulting in a decline of  $\epsilon$  with depth as  $N^2$ , e.g. Kunze and Sanford (1996).

The profiles from the rims (Figure 4.32) show virtually no depth dependence between the surface and 2000 m, despite the large variability in stratification (cf. Figure 4.24). They can therefore

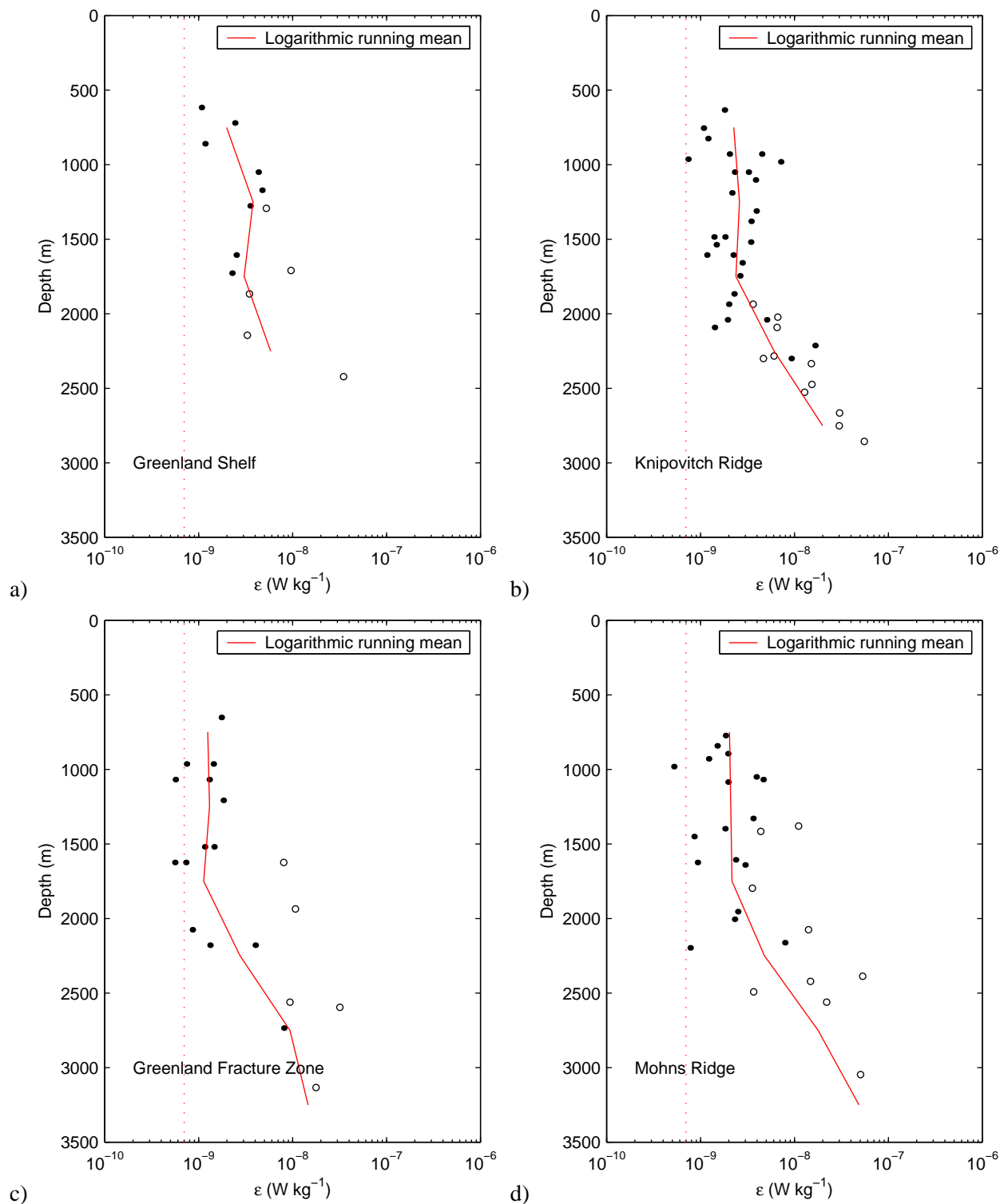


Fig. 4.32: Same as Figure 4.28, but for groups of profiles from the rims of the Greenland Sea. The mean profiles were calculated for 500 m depth bins.

be considered to be in a GM equilibrium (if slightly elevated as compared to GM) in this depth range. Below 2000 m, varying increases can be observed which contradict a possible  $N^2$  dependence. The increases are frequently even steeper than  $1/N^2$ , indicating an inverse relation between dissipation and stratification in the deep water. (This holds even when only the values above the bottom gap-afflicted are considered to exclude possible uncertainties).

The same two-fold depth dependency as for the rim profiles is found (and even more pronounced) in the vertical distribution in the central Greenland Sea (Figure 4.31), where the mean profile shows a decline with decreasing buoyancy frequency in the depth range up to 2000 m. In the abyss, the rise exceeds those at the rims, with dissipation rates occasionally growing as  $N^{-4}$  for single profiles. Thus, the distribution of dissipation in the vertical is obviously characterised by the dominance of the shear contribution in the deep water versus the dominance of stratification in the upper part of the water column.

Increasing dissipation rates towards the bottom similar to those observed in this study have previously been reported from the combined tracer release and microstructure experiment in the Brasil Basin near the Mid-Atlantic Ridge (Polzin et al., 1997; Ledwell et al., 2000), where the magnitude of the increase was closely linked to the local bathymetry and largest above and near the sloping flanks of the ridge.

#### *Eddy Diffusivity – Vertical Structure*

The corresponding eddy diffusivities exhibit (naturally) a depth distribution similar to the dissipation rates, but with more pronounced increase in the deep water due to the missing attenuation by means of the  $N^2$  term in Equation 4.12.

The numbers for the eddy diffusivities found in the uppermost 1000 m are generally smaller than those derived from the Thorpe scale calculation (Section 4.4). The difference is largest for the profiles from the Greenland Shelf break (Figure 4.34a), where the mean diffusivity calculated from the finescale shear and strain spectra (1100 m segments centred at 600 m depth) is  $K_\rho = 0.5 \times 10^{-4} \text{ m}^2 \text{ s}^{-1}$ , as compared to the  $9.8 \times 10^{-4} \text{ m}^2 \text{ s}^{-1}$  from the Thorpe scales. This is a quite dramatic difference, even if single profiles are considered, where the finescale estimate can rise up to  $1.1 \times 10^{-4} \text{ m}^2 \text{ s}^{-1}$ . The underestimation of the finescale estimates compared to the Thorpe diffusivities for the Greenland Sea Gyre (Figure 4.33) and the frontal region of the Atlantic inflow above Knipovitch and Mohns Ridge (Figures 4.34b,c) is not quite as large, but more or less within the the estimated accuracy of the method. The profiles from the gyre and the ridges show relatively similar means of  $2.3 \times 10^{-4} \text{ m}^2 \text{ s}^{-1}$  and  $0.9 \times 10^{-4} \text{ m}^2 \text{ s}^{-1}$  respectively, versus the  $2.5 \times 10^{-4} \text{ m}^2 \text{ s}^{-1}$  (gyre) and  $3.6 \times 10^{-4} \text{ m}^2 \text{ s}^{-1}$  (ridge, along  $75^\circ\text{N}$ ) means estimated from the Thorpe analysis.

The diffusivity profiles from the centre fall within a factor of five of the average profile, that is less scatter than could be expected from the added accuracy of the method (factor 4) and the

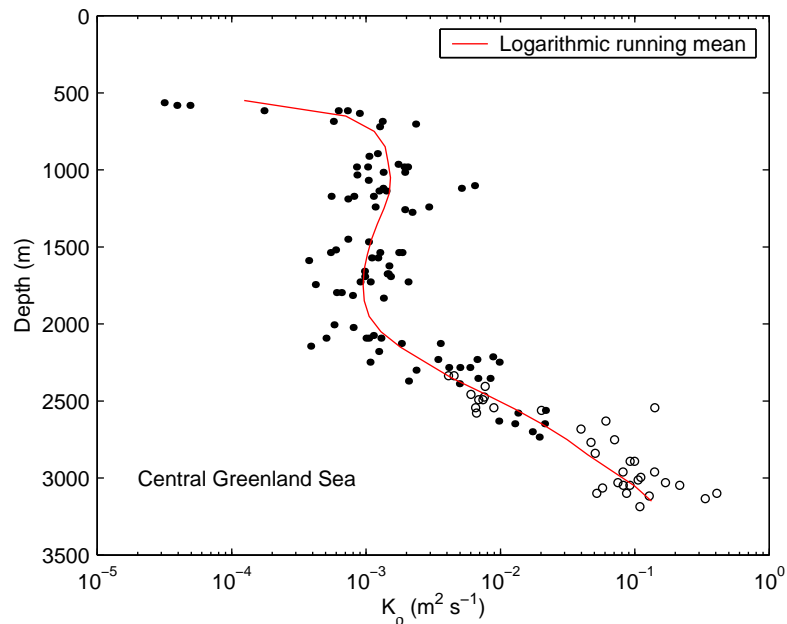


Fig. 4.33: Diapycnal diffusivities for the 24 profiles from the central Greenland Sea. The red line denotes the logarithmic mean calculated for 100 m depth bins. Note that each data point represents a mean over 1100 m, centred at the location of the point.

estimated error of the shear variance (factor 10) alone. Evidently there is not much variation in the interior of the gyre in mixing across the density maximum and most of the deep water (with the exception of some outliers). This is different at rims of the basin, where the variability is larger, especially in the Greenland Fracture Zone and Mohns Ridge (Figures 4.34c,d). The scatter within these profiles increases notably below 1000 m, which indicates a greater spatial variability caused by the impact of the topography and larger variations in the water depth.

The magnitude of the turbulent diffusivities found in the basin exceed virtually everywhere (except in the uppermost part of the water column as discussed above)  $10^{-4} \text{ m}^2 \text{ s}^{-1}$  and thus is elevated by at least an order of magnitude compared to the values found in the deep ocean over abyssal plains (e.g. Toole et al., 1994; Kunze and Sanford, 1996). It is, however, roughly in the range of diffusivities measured above rough topography and near mid-ocean ridges (Polzin et al., 1997; Ledwell et al., 2000), where elevated mixing ( $K_\rho$  in the order of  $10^{-3} \text{ m}^2 \text{ s}^{-1}$ ) associated with the topography was found several hundreds of meters up in the water column. The interesting difference to the observations cited above is the fact that the high eddy diffusivities in the Greenland Sea are not confined to the areas near or above the submarine ridges and fracture zones, but can be found throughout the whole basin.

The intermediate minimum of eddy diffusivity centred slightly above 2000 m depth lies just above the sill depths adjacent to the Norwegian and Island Seas, and well above the maximum exchange depth with the Arctic Ocean, and is furthermore confined to the centre of the gyre. Below

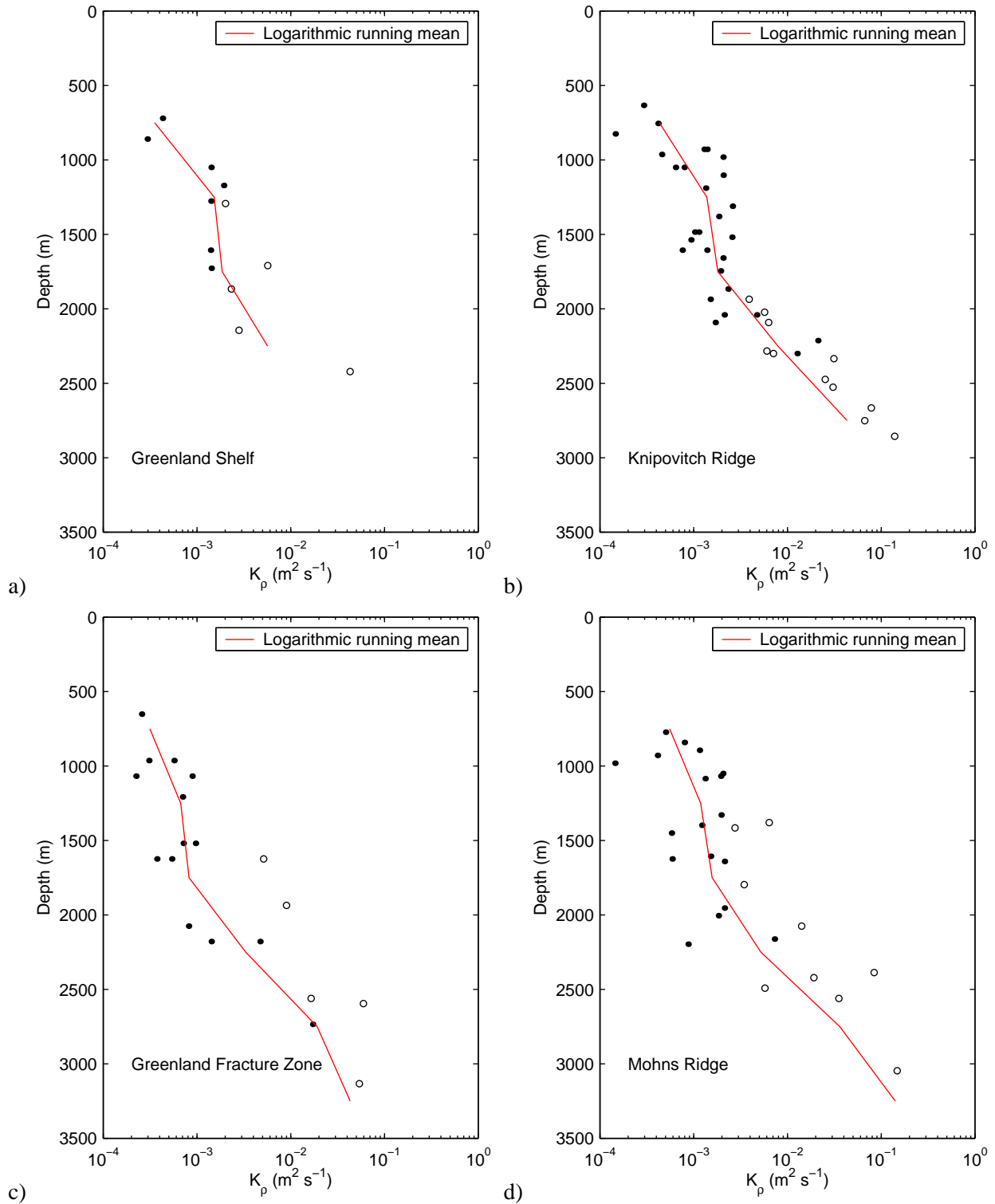


Fig. 4.34: Same as Figure 4.33, but for groups of profiles from the rims of the Greenland Sea. The mean profiles were calculated for 500 m depth bins.

the minimum and at the rims, the diffusivity increases smoothly towards the bottom. This implies that horizontally advected water masses can add to changes in the Greenland Sea Deep Water. For example, the inflowing Eurasian Basin Deep Water (centred at a depth of approximately 2000 m at 75°N, cf. Figure 1.2) can act as an additional source of salinity for the GSDW since it is easily mixed down in the interior.

The very large diffusivities calculated for the abyss are most likely overestimates, since the stratification in the deep interior is almost nonexistent to begin with, and therefore the assumption of a mixing efficiency of 0.2 will probably not hold (see discussion above). Nevertheless, since the deep diffusivities exceed values of  $10^{-2} \text{ m}^2 \text{ s}^{-1}$ , even employing a mixing efficiency reduced by a factor of ten ( $\Gamma = 0.02$ ) will lead to diffusivities much higher than reported from other areas. While this is interesting in itself, the actual numbers of  $K_\rho$  below 2500 m are of little consequence for the water mass properties because of the small initial gradients, and therefore not crucial for this study.

#### *Eddy Diffusivity – Horizontal Distribution*

The horizontal variability of mixing on different depth levels is the subject of the following discussion. Four levels were chosen to represent layers over which vertical exchange is of special interest, for example because of inflowing water masses across the sills. Mapped are the diffusivity values at all stations for the 1100 m segment centred at the selected depth. The layer depicted in the first map spans the depth range influenced by wintertime convection, centred at 800 m (Figure 4.35); the second is centred at the lower limit of this same layer at 1500 m, to illustrate the exchange across the boundary between the convectively ventilated part of the water column and the deep water below (Figure 4.36). The remaining two depths of 2100 m (Figure 4.37) and 2800 m (Figure 4.38) were chosen to represent the vertical exchange across the sill depths towards the Norwegian Sea and the Arctic Ocean, respectively.

The isobath chosen to represent the diffusivities in the convectively renewed layer (Figure 4.35) is 800 m, which means that the depicted values represent segments that cover the range between 250 and 1350 m depth. For a comparison with the results from the Thorpe scale analysis (cf. Section 4.4), it would be more convenient to choose a shallower isobath (e.g. 600 m), but the diffusivities from segments near the surface which include the seasonal surface mixed layer and span large ranges of  $N^2$  are prone to larger errors and therefore not suitable for a station-to-station mapping to analyse spatial variability to a larger extent than already done above with averages from both methods (cf. the scatter in the vertical profiles in this depth, Figures 4.33 and 4.34).

The eddy diffusivities in the upper layer lie between 1 and  $50 \times 10^{-4} \text{ m}^2 \text{ s}^{-1}$ . The average values in this depth range for the different areas scatter around  $10 \times 10^{-4} \text{ m}^2 \text{ s}^{-1}$ , with the highest layer average occurring in the centre (cf. Table 4.4). The diffusivities tend to decrease towards the shallower margins of the basin and above the ridges, where they seldom exceed  $10^{-3} \text{ m}^2 \text{ s}^{-1}$ .

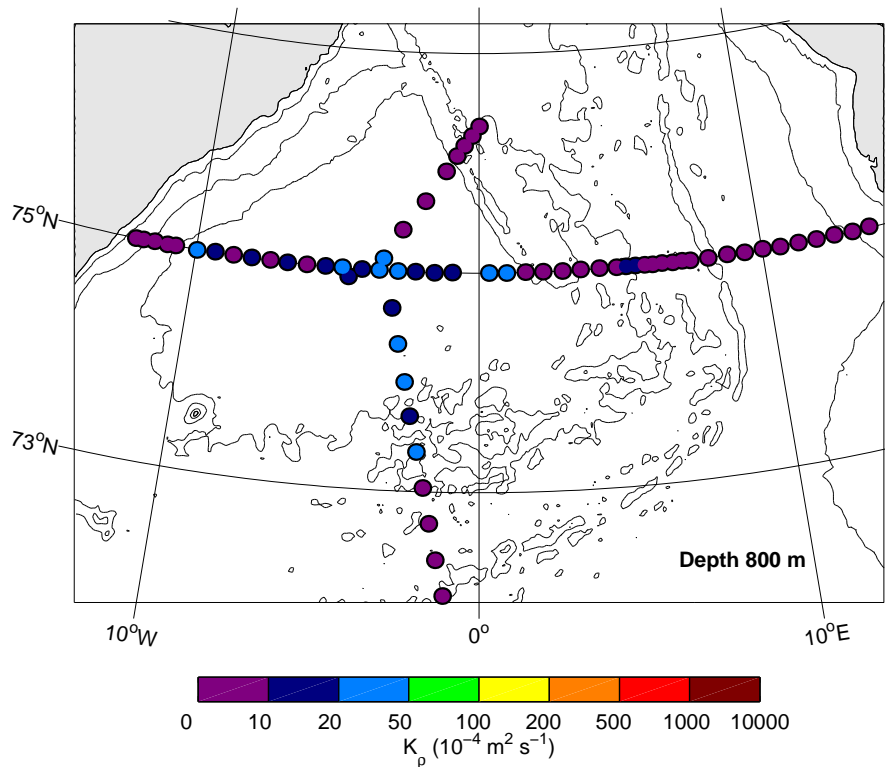


Fig. 4.35: Horizontal distribution of diapycnal diffusivities in the upper layer centred at 800 m water depth.

Single profiles with elevated diffusivities away from the centre can be found approximately at  $10^{\circ}\text{W}$  and  $1^{\circ}\text{E}$  on the  $75^{\circ}\text{N}$  transect; these positions coincide with the locations of the fronts towards the Atlantic Water, therefore frontal instabilities are the probable cause for this heightened mixing.

The eddy diffusivities found east of Knipovitch Ridge, in the Norwegian Sea towards the European shelf, are smaller than any of those in the Greenland Sea Gyre. They do not exceed  $1.6 \times 10^{-4} \text{ m}^2 \text{ s}^{-1}$  and amount to an average of  $6.7 \times 10^{-5} \text{ m}^2 \text{ s}^{-1}$ . This contrast underpins the notion that the Greenland Sea is an environment which is favourable for strong vertical mixing on the basis of several factors (wintertime convection, several frontal regions and strong horizontal gradients near the surface; large areas of rough topography in the abyss).

The upper layer with its freshly ventilated Intermediate Water in the centre of the gyre as well as with its warm and saline Atlantic Water at the western and eastern boundaries is the most likely source for of the heat, salt and tracer input observed in the deep water (cf. Section 1.2). Therefore, the amount and the pattern of vertical mixing across the lower boundary of the upper layer is crucial to the question whether vertical mixing in the Greenland Sea is sufficient to explain the observed modifications in the Greenland Sea Deep Water.

In contrast to the distribution of diffusivities in the upper layer, the maximum mixing across the stability maximum (chosen to be represented by the 1500 m isobath, Figure 4.36) is located at

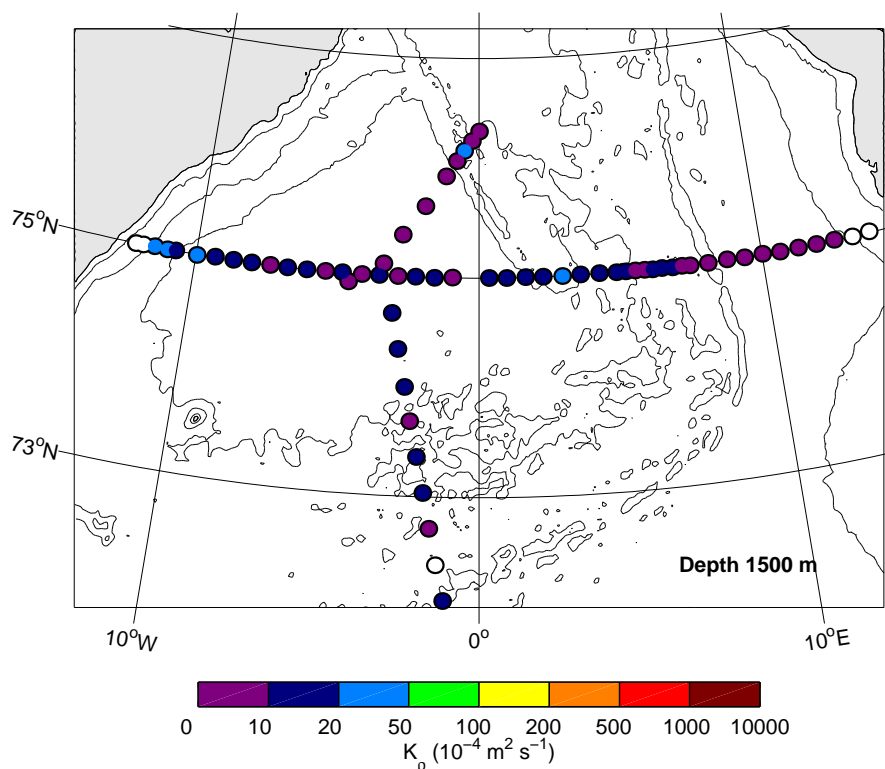


Fig. 4.36: Horizontal distribution of diapycnal diffusivities across the temperature/salinity maximum at the lower boundary of the layer of convection and the Atlantic inflow (segments centred at 1500 m water depth). Stations that were too shallow for this depth layer are marked by empty circles.

the rims of the basin, namely on the Greenland shelf break, and above the ridges and valleys of the Greenland Fracture Zone, where it reaches values of  $K_\rho = 5 \times 10^{-3} \text{ m}^2 \text{ s}^{-1}$ . This attenuation can again be attributed to the fronts between the Atlantic and Polar water masses. Additionally, it may be a remote effect of the underlying topography; the possibilities of interaction of the flow with topography at the different locations will be further explored in Section 5.2. The numbers inside the gyre are up to an order of magnitude smaller, with the minimum occurring over the abyssal plains north of the 75°N transect; despite being smaller than at the western and northern rims, these eddy diffusivities still amount to an average of approximately  $1 \times 10^{-3} \text{ m}^2 \text{ s}^{-1}$ .

The elevated mixing, especially at the shelf break is an excellent means to transport the salinity and heat from the Atlantic and Return Atlantic Water down into deeper layers. This will be somewhat counteracted by the mixing in the centre of the gyre which should result in deepening and eroding the intermediate temperature and salinity maximum (cf. Figure 1.2). This has indeed been observed on repeated surveys along 75°N during the past decade, where a deepening (up to 150 m per year) as well as a slow erosion of the temperature maximum took place (Budéus et al., 1998).

The turbulent diffusivities centred at 2100 m (Figure 4.37) are mostly of the order of  $1 \times$

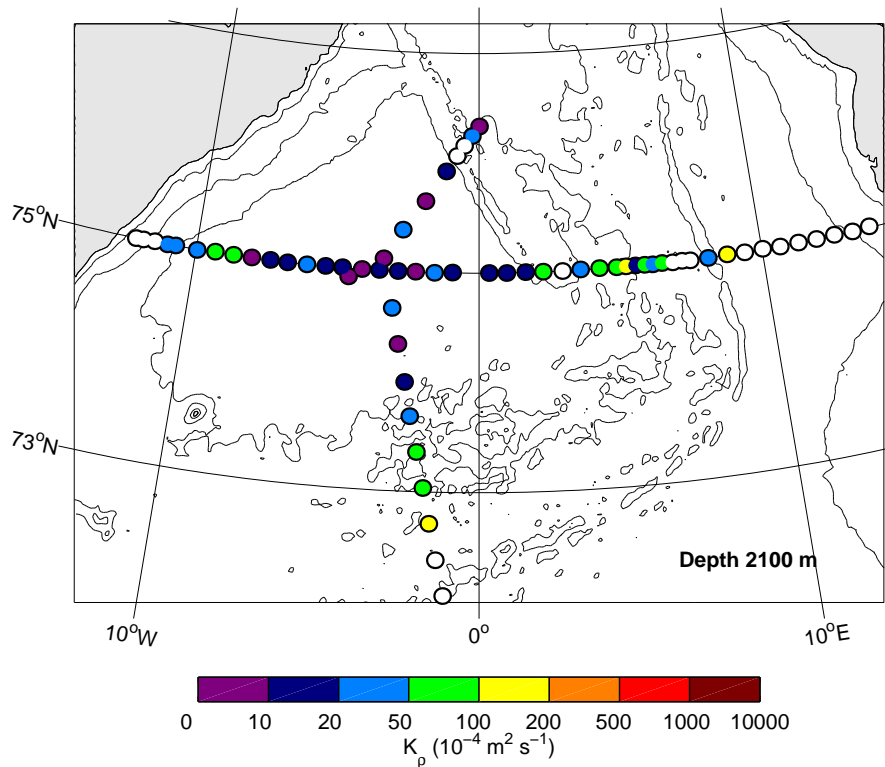


Fig. 4.37: Horizontal distribution of diapycnal diffusivities spanning the sill depth towards Norwegian and Iceland Sea (segments centred at 2100 m). Stations that were too shallow for this depth layer are marked by empty circles.

$10^{-3} \text{ m}^2 \text{ s}^{-1}$  in the Greenland Sea Gyre. Higher diffusivities are again confined to the rims of the basin and the areas above the oceanic ridges. The maxima reach nearly  $2 \times 10^{-2} \text{ m}^2 \text{ s}^{-1}$  at southern end of  $0^\circ$  transect above Mohns Ridge and in the deeper valleys of Knipovitch Ridge. Nearly equally high values can be found off the Greenland shelf break ( $K_\rho$  up to  $10^{-2} \text{ m}^2 \text{ s}^{-1}$ ). This distribution coincides with the anticlockwise pathway of the Eurasian Basin Deep Water that enters the Greenland Sea through Fram Strait and can be found between 1500 and 2200 m at the  $75^\circ\text{N}$  transect (cf. Figure 1.2); especially the denser components of this water mass are therefore accompanied by high mixing rates. Notably the exchange of deep water with the Norwegian Sea through the Jan Mayen Channel and adjacent passages in the ridge system northeast of Jan Mayen is associated with a large amount of vertical mixing. This is a direct affirmation of the notion that the Norwegian Sea Deep Water is formed by mixing of the EBDW with the surrounding GSDW in the southern part of the Greenland Sea Gyre, which was proposed on the grounds of the analysis of water mass properties (Aagaard et al., 1985; Smethie, Jr. et al., 1988; Mauritzen, 1996a).

The mixing processes at the rims and in the interior seem to be quite separated in this intermediate depth ranges; the eddy fluxes near the rough topography are even more elevated than elsewhere

in the Greenland Sea, while the stability maximum in the interior cushions the mixing rate. The amplification of mixing towards the rims of the gyre explains the high share of EBDW, which is relatively low in anthropogenic tracers, in the formation of NSDW (which is also marked by a tracer minimum).

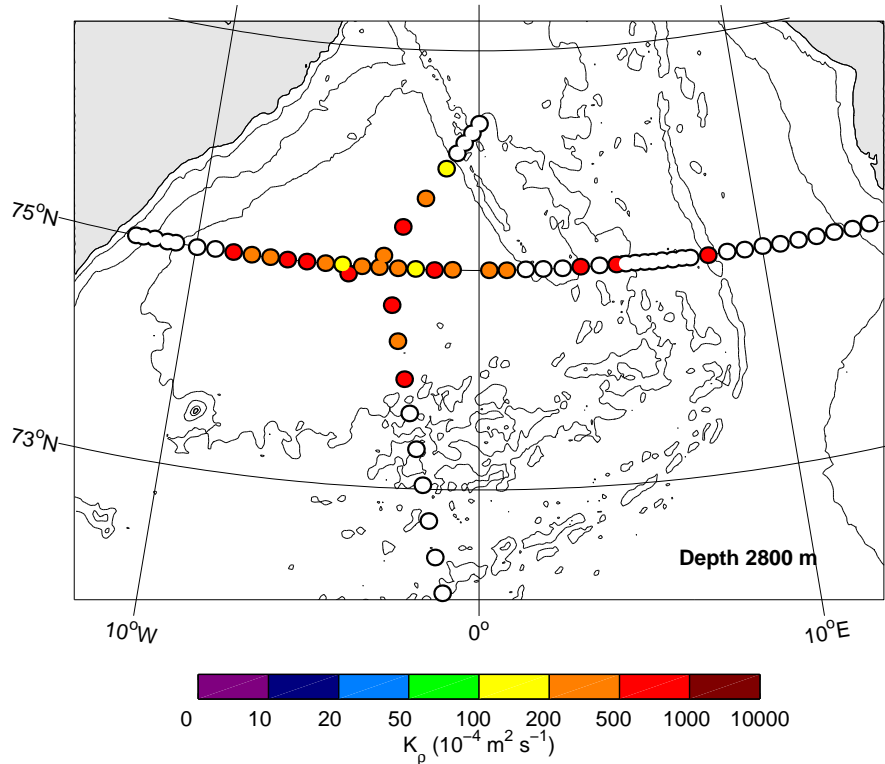


Fig. 4.38: Horizontal distribution of diapycnal diffusivities spanning the sill depth towards the Arctic Ocean (segments centred at 2800 m). Stations that were too shallow for this depth layer are marked by empty circles.

The water column below the deepest exchange depth with the Arctic Ocean can be considered well mixed (Figure 4.38). The eddy diffusivities are elevated above  $10^{-2} \text{ m}^2 \text{ s}^{-1}$  everywhere in the deep basin, and there is no obvious spatial structure in the abyss. Supporting evidence for the existence of high shear variances and consecutively high turbulent diffusivities at great depths in the abyss of the Greenland Sea comes from current meter moorings along the  $75^\circ\text{N}$  parallel from the Greenland Shelf and the western part of the deep basin, originally designed to monitor the variability of the East Greenland Current (Woodgate et al., 1999). The moored current meter timeseries show an intensification of current speed leading to an amplification of kinetic energy in the records of the near bottom instruments. This intensification is more or less permanent on the slope and possibly caused by bottom trapped topographic Rossby waves (Woodgate et al., 1999). It varies in strength barotropically with the East Greenland Current, with the maximum in late winter.

The moored time series from the western part of the Greenland Basin around  $7^{\circ}30'$  W on the other hand exhibit episodic outbreaks of strong bottom currents, which might be connected to sediment avalanches from the shelf break (Woodgate et al., 1999; Woodgate and Fahrbach, 1999). The occasional occurrence of such strong currents (up to  $0.5 \text{ m s}^{-1}$ ) will induce strong shears and consecutively inertial motions, and is therefore an excellent additional means of internal wave excitation in the deep Greenland Sea.

### *Discussion*

There is a slight disagreement between the results from the Thorpe scale analysis and the dissipation rates calculated from the finescale parameterisation in the upper 1000 m. There are several possible reasons for this: (i) the different handling of the variability in this depth range by the different methods, (ii) a possible underestimation of the diffusivity by the omission of the latitude dependency in the Gregg/Polzin parameterisation, and (iii) variable influence of shear versus strain variance; notably very small shear/strain ratios at some stations in the central Greenland Sea.

With regard to (i), the diffusivity estimates from the Thorpe scales, while representing a mean over the range from 100 to 1000 m depth, take into account the strong vertical variability in this part of the water column (Figure 4.8). The uppermost values in the profiles derived by the spectral method are 1100 m averages centred in approximately 600 m depth (cf. Figures 4.33, 4.34). Therefore the vertical scale posed by the method is not appropriate for the scales of the variability in shear and stratification (Figure 4.24) and may consequently smear out the occurring mixing events and result in smaller mean values.

The other likely reason for the discrepancy is (ii). While the possible latitude dependency of the dissipation parameterisation is cancelled out in most parts of the Greenland Sea by the weak stratification (cf. Figure 4.30), it may be necessary to take it into account where the stratification is stronger. This is especially the case at the frontal zone between the interior and the Atlantic inflow at the eastern rim of the gyre and at the return flow of Atlantic water on the Greenland shelf break (Figures 4.2, 4.24). The inclusion of the latitude term in the calculation doubles the figures of diffusivity and dissipation in this regions.

(iii) There are some profiles in the central Greenland Sea, where a strong dominance of strain over shear in the upper few hundred meters lead to small shear/strain ratios (Figure 4.28), which in some cases exceed the limits of validity of the parameterisation, and therefore had to be substituted by larger values for the calculation. As already noted above, this may lead to uncertainties and possible underestimation of the dissipation rate and eddy diffusivities in the affected upper regions of the water column. Kunze et al. (2002) reported the simultaneous observation of directly measured high dissipation rates and small shear/strain ratios in a canyon, where the finescale variance parameterisation underestimated the turbulent diffusivities by a factor of 30. However, since the small ratios in this case here affect only two or three stations, and only in the centre of the gyre, it

is unlikely that they are responsible for the lowered average.

Interestingly, the distribution of the density inversions along 75°N (Figure 4.8a) is better reflected by the distribution of average strain variances alone than by the dissipation rates which take into account the shear as well as the strain variances: Strain in the upper water column is strongly elevated for profiles at the Greenland shelf break and above Knipovitch Ridge compared to the average strain in the central gyre, as can be seen in the average spectra of strain density (Figures 4.26b and 4.27 versus Figure 4.25). This fits the observations of mixing from Arctic (Yermak Plateau and Fram Strait) by Wijesekera et al. (1993), where a strain-only parameterisation worked much better for the scaling of microstructure measurements in the uppermost 200 m than the shear-only parameterisation by Gregg (1989), which led to an underestimate of  $\epsilon$  by a factor of 10. These inconsistency led initially to the inclusion of strain into the dissipation parameterisation by Polzin et al. (1995). Still, it seems that strain is more important than shear in the upper ocean in polar regions, and this is only partly covered by the existent scalings.

There is data source, which, while not exactly comparable to this study, still support the results in various aspects:

In order to study the strength and penetration depth of deep convection, the artificial tracer sulphur hexafluoride ( $SF_6$ ) was released in the central Greenland Sea Gyre in August 1996 (Watson et al., 1999). In the following years, the  $SF_6$  patch was tracked and sampled in its concentration and horizontal and vertical extent. From these data, vertical mixing rates were calculated. For the depth range between 200 m and 1000 m, the authors come up with overall values (from the different surveys) that lie in the range  $0.66 \times 10^{-4} \leq K_z \leq 2.5 \times 10^{-4} \text{ m}^2 \text{ s}^{-1}$ ; When only regarding the concentrations in the central basin, values of  $1.1 \times 10^{-4} \leq K_z \leq 1.5 \times 10^{-3} \text{ m}^2 \text{ s}^{-1}$  are derived from the  $SF_6$  spread (Watson et al., 1999). While these numbers are limited to the upper part of the water column and integrate the effect of winter convection and/or additional vertical mixing in this depth range, they nevertheless compare well with the results from this study, which give  $0.4 \times 10^{-4} \leq K_\rho \leq 8.0 \times 10^{-4} \text{ m}^2 \text{ s}^{-1}$  with a mean of  $K_\rho = 2.3 \times 10^{-4} \text{ m}^2 \text{ s}^{-1}$  for the spectral method applied in approximately the same region and depth range (Greenland Sea Gyre, segments centred at 600 m), and  $K_\rho = 2.5 \times 10^{-4} \text{ m}^2 \text{ s}^{-1}$  for the upper 1000 m of the mid-gyre part of the 75°N transect from the Thorpe scale analysis.

The failure to detect Thorpe inversions in the deep water and the high eddy diffusivities determined by the finescale parameterisation do not mutually contradict each other: The maximum size of turbulent overturns is described by the Ozmidov scale  $L_O = \sqrt{\epsilon/N^3}$ . For a typical observed dissipation rate in the deep water of, say,  $\epsilon = 2 \times 10^{-8} \text{ W kg}^{-1}$  and a buoyancy frequency of  $N = 3 \times 10^{-4} \text{ rad s}^{-1}$  (cf. Table 4.4, Figure 4.31), this results in an Ozmidov scale of 27 m; thus the maximum overturn size is for most cases well below the minimum detection limit of a Thorpe inversion of  $\approx 50 \text{ m}$  as posed by the weak mean gradient and the noise threshold.

An important result that at first sight is opposed to earlier findings is that elevated mixing is

found throughout the whole basin of the Greenland Sea and does not decay away from the ridge systems to the same extent observed elsewhere in the ocean. The absolute maxima of turbulent diffusivities are located in the deepest parts of the interior, although the values near the ridges are elevated for isobaths located at mid-depth. This apparent disconnection of topography and elevated mixing in the deep water may be a consequence of the small horizontal scales of the basin, which has a diameter of only 400 km. The possible mechanisms involved in the generation of the observed distribution will be further discussed in Section 5.2 in the next chapter.



## 5. DISCUSSION

### 5.1 *The Role of Vertical Mixing in Deep Water Formation*

The central question is whether the observed mixing is sufficient to explain the changes in the deep water of the Greenland Sea as visible in temperature, salinity and tracer profiles. In this study, different methods have been employed to assess diapycnal mixing. A snapshot of the horizontal and vertical distribution of turbulent diffusivities was produced with the aid of a quasi-synoptic data set from the summer of 1998. To summarise: the use of a one-dimensional advection-diffusion balance for temperature, salinity and CFC-12 in a 1000 m thick layer (1500 – 2500 m) over a time of 15 years (1982–1997) lead Visbeck and Rhein (2000) to equate the temporal changes in all three parameters to a mean vertical diffusivity of  $2 - 3 \times 10^{-3} \text{ m}^2 \text{ s}^{-1}$ . An earlier estimate by Meincke and Rudels (1995) from the changing T-S relation of two single profiles from the central Greenland Sea (1982 and 1993) arrived at turbulent diffusivity of  $1 - 2 \times 10^{-3} \text{ m}^2 \text{ s}^{-1}$  across the salinity maximum.

How do the findings of this study compare to the values above? The average eddy diffusivity in the central Greenland Sea in the layer centred at 2000 m amounts to  $K_\rho = 1.2 \times 10^{-3} \text{ m}^2 \text{ s}^{-1}$  (cf. Table 4.4); the choice of this depth covers the layer considered by the cited authors as well the location of the salinity maximum, and is therefore well suited for a comparison. The actual depth of the salinity maximum in 1998 was closer to 1700 than to 2000 m; the mean diapycnal diffusivity centred at this isobath (1700 m) is  $K_\rho = 0.9 \times 10^{-3} \text{ m}^2 \text{ s}^{-1}$  for this survey, thus slightly lower than at the deeper level (cf. Figure 5.1).

In all, the average diffusivities measured in this study are at the lower end of the range which would be expected from the developments of water mass properties, if those were solely due to diapycnal mixing. Further aspects of the results which shed additional light on the role of vertical mixing in deep water formation will be discussed in the following:

- Does the spatial distribution of the mixing inferred in this study relate to the observed patterns and evolutions of temperature, salinity and tracers?
- How does the amount of deep water ventilated by vertical mixing compare to the ventilation rates accomplished by other mechanisms?
- What is the contribution of bottom boundary layer mixing?

- Is the observed situation a possible equilibrium? Or is it a sign of the Greenland Sea in a transition from a site of deep convection towards a new, differently balanced state?
- Does the intermittency of some of the forcings influence the net effect of the mixing? If so, on which timescales? How suitable is a summer snapshot for an assessment of the quantitative role of mixing in deep water formation?

### Observed Patterns of Mixing and Ventilation

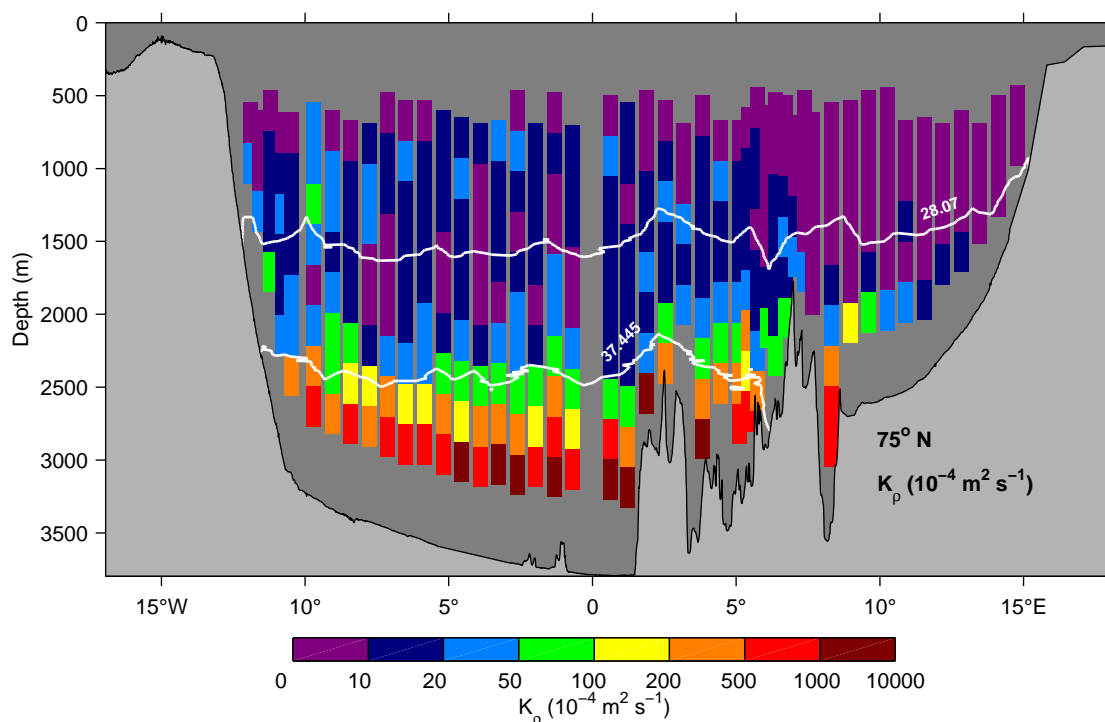


Fig. 5.1: Transect of  $K_p$  along  $75^\circ\text{N}$  as computed from the LADCP and CTD data from the ARK XIV/2 cruise during late summer 1998. Note that each depth bin represents the value computed from a centred 1100 m depth segment. Included for reference are the isopycnals  $\sigma_\theta = 28.07$  and  $\sigma_2 = 37.445$ , denoting the approximate location of the stability maximum and the core density of the EBDW inflow, respectively.

The spatial inhomogeneities of the observed mixing rates are in the following compared to the patterns and changes found in the water mass properties on the basis of the distribution of two properties along a zonal transects across the Nordic Seas. Figure 5.1 shows the best estimate of the turbulent diffusivity as computed from LADCP and CTD data (Section 4.7) along the 75th parallel. An independent proxy for the ventilation are the measurements of the anthropogenic chlorofluorocarbon CFC-12 taken during the same late summer cruise (ARK XIV/2) as the mixing data. The concentrations along  $75^\circ\text{N}$  are plotted in Figure 5.2. The CFC distribution gives an

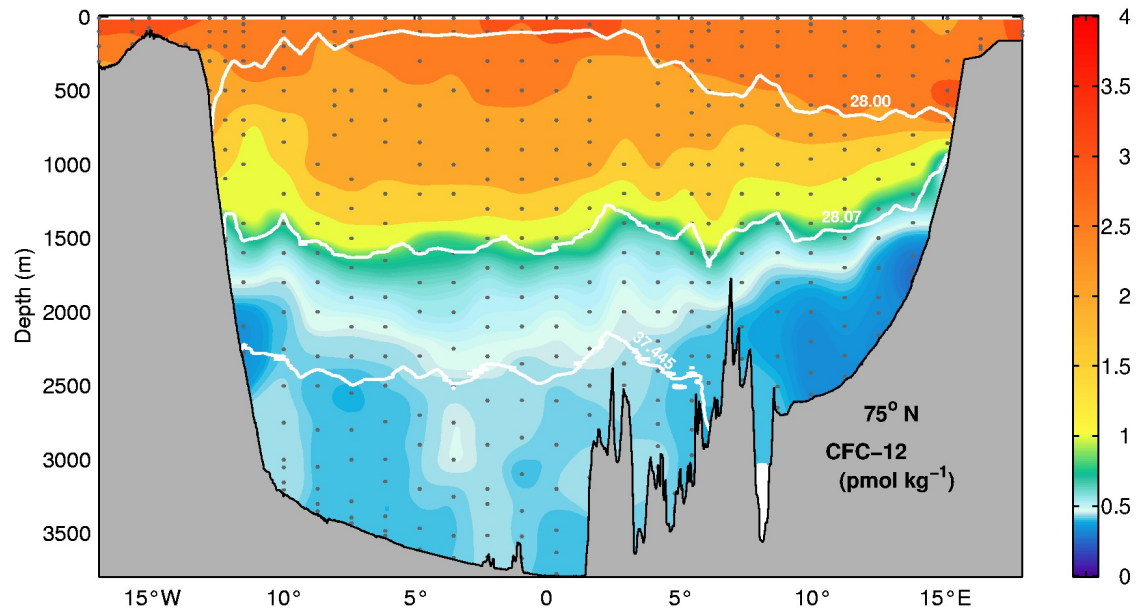


Fig. 5.2: Transect of CFC-12 along  $75^\circ\text{N}$  with data from the same stations as Figure 5.1 (ARK XIV/2). Contour interval is  $0.01\text{ pmol/kg}$  for the Deep Water, and  $1.0\text{ pmol/kg}$  for CFC contents larger than  $1\text{ pmol/kg}$ . For plotting, the bottle data were interpolated on a  $20\text{ m} \times 0.1^\circ$  grid using an objective analysis method. The original data points are denoted by grey dots. Included for reference are the isopycnals  $\sigma_\theta = 28.00$ ,  $\sigma_\theta = 28.07$ , and  $\sigma_2 = 37.445$ , denoting the lower boundary of the Atlantic Water, the approximate location of the stability maximum and the core density of the EBDW inflow, respectively.

integral picture of the ventilation over the last couple of decades since the CFCs are transferred into the ocean via the atmosphere. The atmospheric concentration has been zero prior to the start of industrial production in the early 20th century and increased until the 1990s (e.g. Walker et al., 1999). Thus, high concentrations in an oceanic water body denote a recent contact with the atmosphere, whereas low concentrations are an indicator of either a slow ventilation or a separation from the surface over a long period.

From the surface down to the stability maximum (indicated by the  $\sigma_\theta = 28.07$  isopycnal in the Figures 5.1 and 5.2), the tracer gradients are large because of the constant supply of CFC at the surface, and the comparatively weak mixing in this depth range. Vertically homogeneous tracer concentrations that indicate stronger mixing can be found in the deeper part of the East Greenland Current (between 700 and 1500 m, approximately  $11^\circ\text{W}$ ) and, to a lesser degree, below the lower boundary of the Atlantic Water above Mohns and Knipovitch Ridge ( $3^\circ\text{E}$ , 500 m –  $6^\circ\text{E}$ , 1300 m). The large homogeneous water body in the Greenland Sea Gyre above 1000 m between  $8^\circ\text{W}$  and  $3^\circ\text{E}$  is caused by wintertime convective mixing and only partially reflected by the diffusivities. The weakest mixing in the upper layer (and the whole transect) is found from the surface down to 2000 m depth east of the ridge system in the northern extension of the Norwegian Sea.

There is only a relatively slow exchange across the stability maximum located between 1500 and 1700 m depth. In the centre of the Greenland Sea Gyre, the smallest diffusivities of  $K_\rho \leq 1 \times 10^{-3} \text{m}^2 \text{s}^{-1}$  are found around 1500 m. From this distribution, the strongest diapycnal fluxes between intermediate and deep water masses are located at the rims of the gyre, below the EGC and above the ridges. This restricts the vertical exchange mainly to warm and saline water masses of Atlantic origin, and is in accordance with the observations of the deep water getting equally warmer and more saline.

The eddy diffusivities in the deep water range get very large with increasing depth throughout the whole transect. The highest values are found at the western flank of Mohns Ridge, and in the deepest part of the Greenland Basin below the sill depths with the adjacent basins (denoted in Figures 5.1 and 5.2 by core isopycnal of the EBDW,  $\sigma_2 = 37.445$ ). Accordingly, the cross-isopycnal gradients of the CFC-12 below the stability maximum are weak and diminish towards the abyss. The relative importance of the lateral advection above the sill depths is reflected by the spreading of the minimum CFC concentrations associated with the less well ventilated deep water masses of the Arctic Ocean (EBDW, located at the Greenland shelf) and the Norwegian Sea (NSDW, east of Knipovitch Ridge). Since these two water masses are also warmer and saltier than the GSDW, they are partly responsible for the hydrographic observations from the mid-1970s to the present, which showed a spreading of higher temperatures and salinities from the margins towards the center and a subsequent reduction of the horizontal gradients along density surfaces. The spreading has come to a natural halt in the 1990s, when the gradients were completely eroded (Budéus et al., 1998).

Nonetheless, the penetration of higher CFC contents in the centre of the gyre and the high abyssal turbulent diffusivities clearly show that the observed trends in the deep water are to a large part caused by elevated diapycnal mixing and not merely by lateral advection.

#### *Ventilation Rates of Greenland Sea Deep Water*

Besides the deep water formation rate, which can accurately only be determined by a water mass census, there are several other ways to quantify the amount of ventilation in a water body. Commonly used measures are the vertical volume transport and turnover timescales. Most estimates of those quantities stem from the use of box models, which constrain the exchange between some source water masses and a surface reservoir with measured profiles of various tracers, e.g. Radio-carbon, CFCs and Tritium (Peterson and Rooth, 1976; Smethie, Jr. et al., 1986, 1988; Schlosser et al., 1991; Rhein, 1991, 1996). The timescale of deep water renewal by deep convection for all of these models fall between 10 and 35 years for the time before 1980. Since then, with the cessation of deep convection, the turnover rates have risen to much larger periods between 100 to 200 years. For models which include the lateral exchange with the adjacent deep water masses EBDW and NSDW, the numbers are significantly reduced, especially for the recent situation with timescales be-

tween 25 and 70 years. In terms of volume transports, these ventilation rates translate to numbers up to more than 1 Sv before 1980 (Rhein, 1991) and gradually decrease from then on, towards 0.1 Sv in the first half of the 1990s (Rhein, 1996; Bönisch et al., 1997).

To compare the volume of GSDW ventilated by open ocean convection or other processes with efficiency of ventilation by diapycnal mixing, it is necessary to express the measured turbulent diffusivities in those quantities: The one-dimensional advection-diffusion balance

$$w \frac{\partial \rho}{\partial z} = \frac{\partial}{\partial z} \left( K_\rho \frac{\partial \rho}{\partial z} \right) \approx K_\rho \frac{\partial^2 \rho}{\partial z^2} \quad (5.1)$$

(Munk, 1966) relates the turbulent diffusivity  $K_\rho$  to the vertical velocity. For an exponential solution, the ratio of the diffusivity to the vertical velocity is therefore given by the scale depth of the stratification as

$$\frac{K_\rho}{w} = \frac{\partial \rho / \partial z}{\partial^2 \rho / \partial z^2} = z_0 \Rightarrow w = \frac{K_\rho}{z_0} \quad (5.2)$$

An eddy diffusivity of  $K_\rho \approx 10^{-3} \text{ m}^2 \text{ s}^{-1}$  across the boundary between the layer reached by convection in the last two decades and the deep water could therefore be expressed as an effective vertical velocity of approximately  $w = -8 \times 10^{-7} \text{ m s}^{-1}$  (employing a density scaling depth of  $z_0 = -1300 \text{ m}$ ). At the 1500 m depth level, the Greenland Sea covers an area of approximately  $0.3 \times 10^6 \text{ km}^2$  (e.g. Aagaard et al., 1985), thus the effective vertical velocity corresponds to a volume flux of roughly 0.25 Sv across this isobath.

In the same way, an effective vertical velocity could also be expressed as a turnover timescale. The renewal of the deep water below the stability maximum entails the overturning of a water column of approximately 2000 m vertical extent. Thus for the above cited diffusivity ( $K_\rho = 1 \times 10^{-3} \text{ m}^2 \text{ s}^{-1}$ ) and respective velocity  $w$ , the timescale is approximately 80 years. At the level of the lateral advection of EBDW and NSDW, the eddy diffusivities are already an order of magnitude higher (Figure 5.1), which reduces the turnover time for the remaining 1000 m in the abyss to less than one year; therefore any contribution of those two water masses towards the total ventilation will lower the average. Allowing for this, the turnover timescale associated with diapycnal mixing indicates a rate of ventilation which is well within the range given by the models for the period since the cessation of deep convection.

Is it possible to evaluate the effect of other ventilation processes, namely convection, during the late 1990s? Observation and modeling showed that the ventilation depth (by open ocean convection) amounted to between 500 and 1500 m in the years 1994 to 2000 (Budéus et al., 1998; Ronski, 2002), thus not reaching the depth of the GSDW. From the  $SF_6$  release experiment, Watson et al. (1999) estimated that even in the ventilated depth range, only about 10% of the water in the gyre centre was turned over by convective mixing. An active deep water formation by basinwide open ocean convection is thus unlikely. However, the repeated hydrographic surveys in the past couple of

years discovered the existence of stable chimneys that reached considerably deeper, and are probably caused by localised convective processes at the rims of the Greenland Sea Gyre. Analysing float data, Gascard et al. (2002) found evidence for eight chimneys over the course of two years; the trajectories suggested that the vortices are typically 5 km in diameter and have a lifespan of more than a year. In case of breaking up, they may play some role for the ventilation of the GSDW, and should be included in a discussion of ventilation rates. A large chimney, which was located approximately at the intersection of the 75th parallel and the Greenwich meridian, was monitored during winter 2001 (Wadhams et al., 2002). The chimney had a diameter of 10 km and a vertical extent of 2400 m; this translates into a reservoir of roughly 200 km<sup>3</sup> ventilated water. Therefore, every chimney of a comparable size would add (if breaking up) less than 0.01 Sv towards a deep water budget over the period of a year. Only, while the stratification inside was weak, the density of the 2001 chimney was not high enough to penetrate into the deep water; the equilibrium depth of the trapped water was only 1800 m (Wadhams et al., 2002). According to this, the direct freshening and cooling of GSDW because of the breakdown of isolated, long-lived chimneys is probably negligible in the present day situation. This may be different though in times when the surface fluxes are strong enough to produce water dense enough to penetrate into the deep water domain.

#### *Circulation and Transition*

The ongoing temporal change of the thermal structure of the Greenland Sea Gyre raises the question whether the direct ventilation by open ocean convection is a requirement to sustain a thermal equilibrium in the gyre (and the Nordic Seas as a whole). The downward displacement of isothermals in the gyre in the years from 1993 to 1996 (Budéus et al. (1998); equivalent to a homogeneous sinking velocity of 150 m yr<sup>-1</sup>, and a corresponding volume transport of 0.6 Sv) points towards the possibility that the Greenland Sea may be in an energetic imbalance since the cessation of deep convection, and a new equilibrium state is not yet reached.

When discussing dynamical implications, it is useful to employ a diapycnal instead of a vertical velocity (as assumed by the one-dimensional balance of Equation 5.1, which represents a basin-wide mean state rather than a local balance). Neglecting lateral fluxes and terms related to slope and curvature of isopycnals, the diapycnal advection (away from the boundaries) can be approximated as

$$w_* N^2 \cong -\frac{\partial J_b}{\partial z} \quad (5.3)$$

(e.g. St. Laurent et al. (2001), and references therein). The turbulent buoyancy flux  $J_b$  is related to the eddy diffusivity as  $J_b = -K_\rho N^2$ , hence the diapycnal velocity  $w_*$  can be expressed in terms of the vertical change of dissipation rate and mixing efficiency as

$$w_* \cong N^{-2} \frac{\partial(\Gamma\epsilon)}{\partial z} \quad (5.4)$$

(cf. Section 2.2).

For the distribution of dissipation in the Greenland Sea, Equation 5.4 implies a substantial increase of velocity with depth below 2000 m (cf. Figure 4.31), if the increasing dissipation is not balanced by an abyssal decrease of the mixing efficiency  $\Gamma$ . An increase of velocities with depth requires upwelling elsewhere to come to a mass balance. A likely candidate is the bottom boundary layer; mixing in a homogeneous BBL on a slope induces an upslope transport in the boundary layer, depending on the stratification and the volume of the boundary layer. Visbeck and Rhein (2000) estimated the BBL of the Greenland Basin to be capable of an upward transport between 0.1 Sv at 2000 m increasing towards 0.5 Sv with the growing relative volume of the layer. The resulting secondary circulation in the vertical consists of an overturning cell below approximately 2000 m. Above this depth, the flow in the boundary layer is not favourable to sustain sinking in the interior.

An interesting point for speculation is the effect of the depth-increasing downward velocity on the vorticity balance and subsequently on the horizontal flow field. The induced stretching of the water column reduces the potential vorticity. For retaining the balance, the water column must either increase its planetary vorticity by moving northward, or its relative vorticity by acquiring more cyclonic rotation. A detailed examination of the patterns of upwelling and their effect on the abyssal circulation would be of great interest, but exceeds the limits of the present data set and is beyond the scope of this study. For now, it is sufficient to conclude that there may be regions preferred for the upwelling required by the mid-gyre mixing, for example the northern boundary, the Greenland Fracture Zone and the rift valleys therein.

Ongoing turbulent mixing and further absence of deep convection will result in continued warming and decrease in density of the deep water, until the density is small enough to reverse the lateral exchange flows with the neighboring basins. For the Lofoten Basin, the spreading of the high salinity and low CFC water from the east towards the centre of the gyre is a sign that the direction of the flow across Mohns Ridge has already reversed and that the NSDW, instead of being formed by an overflow of a mix between GSDW and EBDW, is now acting as a source water mass for the GSDW.

#### *Contribution of the Bottom Boundary Layer*

Visbeck and Rhein (2000) argued that the bottom boundary layer may play an important role in the overall budget, because it takes up a large portion of the total area of the bowl-shaped Greenland basin. Neglecting a possible overestimation of the diffusivity by the unknown mixing efficiency, the exponential rise towards the sea bed can be interpreted as an increasing impact of the well-mixed bottom boundary layer on the dissipation and diffusivity estimates towards the bottom and used to qualitatively assess the portion of the overall mixing rates caused by boundary mixing.

When considering only the profiles from the central Greenland Sea, a straightforward extrapolation of the increase in diffusivity down to the bottom (Figure 5.3) yields a value of

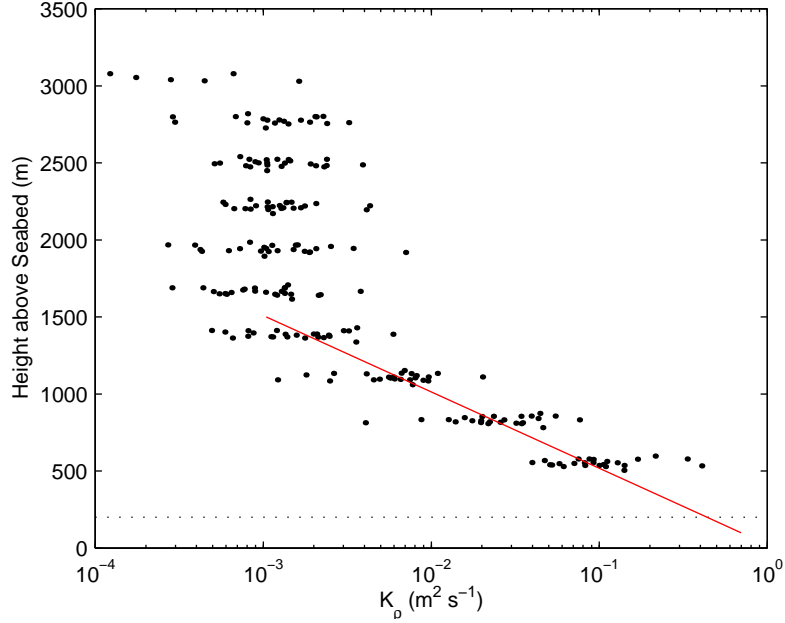


Fig. 5.3: Diapycnal diffusivities  $K_\rho$  in the central Greenland Sea plotted against height above seabed. Extrapolation of the increase in the deepest 1500 m (red line) yields a diffusivity of up to  $(1.1 \pm 0.2) \text{ m}^2 \text{ s}^{-1}$  in the bottom boundary layer (maximum vertical extent of the well mixed layer in the CTD data is denoted by the dotted line). The inclusion of the shallower profiles from the rims with smaller diffusivities (not shown here) lowers this value towards  $K_\rho = (2.2 \pm 0.6) \times 10^{-1} \text{ m}^2 \text{ s}^{-1}$ .

$K_\rho = (1.1 \pm 0.2) \text{ m}^2 \text{ s}^{-1}$  at zero elevation above the sea bed from the fit. This value is lowered towards  $K_\rho = (2.2 \pm 0.6) \times 10^{-1} \text{ m}^2 \text{ s}^{-1}$  when all available profiles, including the shallow ones from the rims with lower diffusivities, are taken into account (not shown; cf. Figure 4.22). Visual inspection of the temperature, salinity and density profiles from the central Greenland Sea indicates homogeneous BBLs between 50 and 200 m thickness, with the largest vertical extents occurring at the deepest locations. If the average thickness of the BBL is taken to be 100 m, the extrapolation executed above results in a diffusivity of  $(7.0 \pm 1.3) \times 10^{-1} \text{ m}^2 \text{ s}^{-1}$  for this boundary layer in the deep Greenland Basin (equivalent to  $(1.5 \pm 0.4) \times 10^{-1} \text{ m}^2 \text{ s}^{-1}$  for the whole area).

The overall volume of the BBL adds up to approximately one third of the total area below 2000 m; considering the diffusivity of  $1.2 \times 10^{-3} \text{ m}^2 \text{ s}^{-1}$  measured in the interior, the boundary layer mixing required to account for an overall average of  $3 \times 10^{-3} \text{ m}^2 \text{ s}^{-1}$  amounts to approximately  $7 \times 10^{-3} \text{ m}^2 \text{ s}^{-1}$ . This is much less than the above number inferred from the increase of diffusivities towards the bottom, and reinforces the notion that the abyssal diffusivities represent an overestimate because of the use of the canonical  $\Gamma = 0.2$ . The ratio of the boundary layer diffusivity evaluated here and the one required to close the tracer budgets suggest that the genuine mixing efficiency falls in the range between 0.01 and 0.02.

### *Temporal Variability*

Some of the mechanisms which are involved in the generation of the mixing are subject to temporal (seasonal as well as interannual) variability. The present study is a late summer situation, and additional effects may occur during other seasons. Namely in winter, the forcing from the surface is altered because of the extreme weather conditions. While it is not possible to quantify the effects of the changes in the forcing on the turbulent mixing rates, it is nevertheless interesting to speculate about the qualitative effects. The near surface circulation in the Nordic Seas is mainly winddriven with large seasonal variations; the rotation of the windstress has a minimum in summer, and reaches its maximum in late fall (Jónsson, 1991). This has direct impact on the strength and the kinetic energy of the current system, in particular the East Greenland and West Spitsbergen Currents.

The EGC consists of a thermohaline and a wind-driven component, with the latter being three times stronger in winter than in summer (Woodgate et al., 1999). The strength of mixing inside the EGC itself and exchange with the surrounding water from the Greenland Sea Gyre is connected with barotropic instabilities, triggered by fluctuations of the current (Strass et al., 1993). The amount of mixing across the boundary between Atlantic Water and the interior as a result of instabilities is therefore defined by the environmental conditions of the EGC. Variations in the atmospheric forcing as an increase in storm frequency or generally stronger winds in fall and winter will therefore result in higher mixing rates than observed in summer. In addition, the large barotropic component of the EGC and the bottom trapped topographic Rossby waves associated with the deep EGC (Woodgate et al., 1999) constitute a means to propagate surface forcing signals into the deep water domain, thus a response to a seasonal signal is not necessarily restricted to the upper layer. A reaction to surface forcing similar to that of the EGC (except probably the interaction with topography) can be expected from the Atlantic Water domain and the WSC. For example, the geostrophic transport of the Atlantic inflow as well as its temperature and salinity are correlated to the atmospheric surface conditions in winter for periods of strong westerly winds (Mork and Blindheim, 2000).

For the interior of the Greenland Sea Gyre, the spreading of the  $SF_6$  patch in the upper layers during the tracer release experiment indicated that the highest vertical mixing occurred in the spring, when the numbers were doubled compared to late summer (Watson et al., 1999). However, late winter is the season where open ocean convection is most likely to occur, thus the spring maximum is probably largely caused by mid-depth convection.

The possible influence of the surface forcing on the strength of the mixing at the boundaries of the currents (and therefore the amount of downward mixing of heat, salt, and tracers) poses the question whether the trends observed in the deep water show some similarity to changes and trends in the large scale atmospheric conditions over the years. A common tool to characterise the state of the atmosphere in the area of the subpolar North Atlantic is the North Atlantic Oscillation (NAO) index. The index is based on the atmospheric pressure difference between Iceland and the

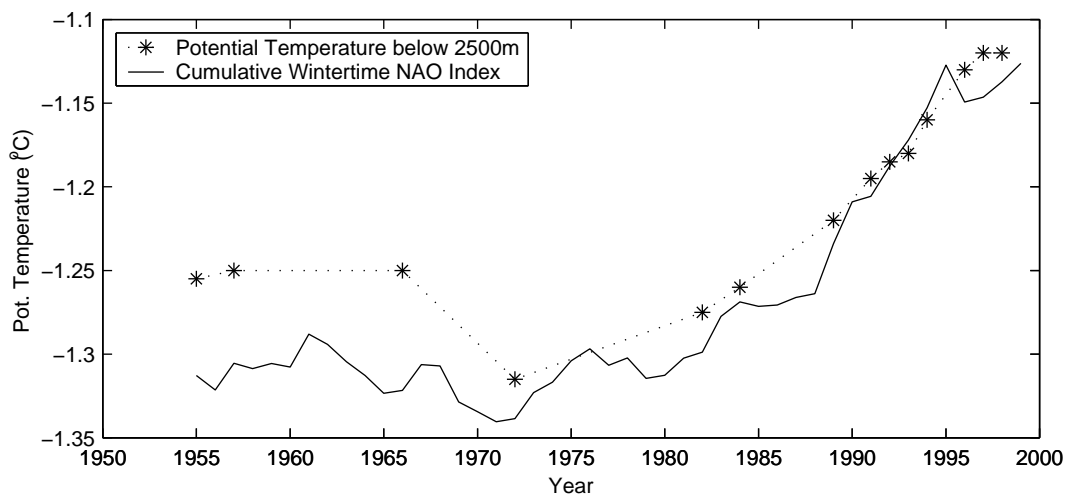


Fig. 5.4: Timeseries of average potential temperature in the GSDW below 2500 m and appropriately scaled cumulative wintertime (DJFM) NAO index (updated from Jones et al., 1997) over the same time period.

Azores (or Lisboa), thus representing the relative strengths of the Iceland low and the Azores high (Hurrell, 1995). For a positive NAO index, both high and low are strongly developed, and as result, so are the mid-latitude westerlies, which carry warm, humid air with them. For the domain of the Nordic Seas, a NAO+ situation is marked by stronger southward winds parallel to the Greenland shore, along with a lesser ice coverage and higher export; inflow of the warm humid air with the northward winds along the Norwegian coastline, and a heightened storm frequency in the southern part north of Iceland. A negative index on the other hand goes along with weak westerlies over the North Atlantic, and the dominance of cold, dry, arctic air together with generally weak winds in the area of the Nordic Seas.

If the strength of the turbulent mixing in the upper layer and the subsequent transfer of properties as temperature and salinity into the deep water domain depends in some way on the interaction of the upper layers with the atmosphere, the development of the deep water properties as a result of the mixing should be related to the integrated effect of the atmospheric variability. Elevated mixing can be expected for a NAO+ situation, when the energy input by the wind is stronger and the ocean–atmosphere interaction is not reduced by an ice cover. In Figure 5.4, the evolution of the deep water temperature is compared to the cumulative wintertime NAO index. The two timeseries are significantly correlated (a similar but slightly weaker correlation is found for the annual mean index; not shown). Since a high correlation can be a spurious result of the rise apparent in both series, it should not be overinterpreted. Nevertheless, it may serve as an indicator that the turbulent mixing below the surface mixed layer is not entirely decoupled from surface interaction and at least part of the energy for the mixing in the interior stems from the wind.

## 5.2 Sources and Distribution of Energy

The observed distribution of turbulent diffusivity differs in an important way from observation in other places with high diapycnal mixing, e.g. the Mid Atlantic Ridge in South Atlantic. While elevated mixing in those locations was strongly associated with the nearby rough topography (Polzin et al., 1997), the diffusivities in the Greenland Sea show only a moderate increase towards the rough ridge system, but are strongly elevated throughout the basin (Figure 5.1).

The principle understanding of the sources of energy for mixing and the processes involved has considerably increased in recent years, prompted by the proliferation of observations and complementing modeling (see Garrett and St.Laurent (2002) for a recent review). However, central questions like the relative importance of different possible energy sources and the mechanisms of the energy transfer to smaller scales, its efficiency, and the regions and reasons of the eventual dissipation are still open. High mixing near rough topography is commonly attributed to heightened internal wave activity, caused by interaction between the flow and the topography.

In the framework of this study, the available data will be used to describe the environmental conditions for the internal wave climate with the goal to gain a better understanding of the processes and conditions which lead to the unusual height and distribution of the diapycnal mixing in the Greenland Sea.

It was already discussed in the previous section that the temporal trend in the deep water properties bears some resemblance to the integrated NAO index, and that therefore the atmospheric forcing must be considered a part of the energy supply for the diapycnal mixing. The important role of other, additional, energy sources is stressed by the fact that the integrated measured dissipation in the upper layer of approximately  $2.5 \text{ mW m}^{-2}$  (cf. Table 4.4) already exceeds the direct input of energy by wind ( $1.6 \text{ mW m}^{-2}$ ; average of the years 1994 to 2000 estimated with an one-dimensional model; Ronski, 2002).

Microstructure measurements of dissipation rates at other deep ocean sites (e.g. Brasil Basin, Ledwell et al., 2001; Hawaiian Ridge, Finnigan et al., 2002) have exhibited a modulation with the tidal cycle, which lead to the assumption that the most likely supply of energy for diapycnal mixing in the deep water are internal tides. Recent global estimates of dissipation of tidal energy based on satellite altimetry and modeling have shown that about one third of the total dissipation takes place in the deep ocean, mostly near rough topography (Egbert and Ray, 2000). Tides are therefore the likely source of energy for mixing, and will be the focus of the following discussion.

### *Internal Tides*

Tidal motions in the ocean can be divided into the barotropic tides, which result directly from the gravitational pull of the sun and the moon on the rotating earth, and baroclinic tides, which spring from the interaction of the barotropic tide with the underlying topography. The latter are also

| Mooring | Position                | Depth (m) |      | Tidal Constituent (cm/s) |       |       |       |
|---------|-------------------------|-----------|------|--------------------------|-------|-------|-------|
|         |                         | Water     | RCM  | $M_2$                    | $S_2$ | $K_1$ | $O_1$ |
| M250    | 73°21.5' N<br>0°48.0' W | 3008      | 371  | 1.3                      | 0.5   | 0.7   | 0.2   |
|         |                         |           | 825  | 1.1                      | 0.3   | 0.7   | 0.3   |
|         |                         |           | 1437 | 0.6                      | 0.3   | 0.7   | 0.2   |
|         |                         |           | 2440 | 0.4                      | 0.2   | 0.6   | 0.2   |
| M319    | 74°57.0' N<br>4°59.0' W | 3554      | 347  | 0.2                      | 0.2   | 0.7   | 0.3   |
|         |                         |           | 1345 | 0.2                      | 0.2   | 0.6   | 0.3   |

Tab. 5.1: Amplitudes of the major tidal components from harmonic analysis of current meters records from the central Greenland Sea (M319) and Mohns Ridge (M250); for details of the moorings see Section 3.3 and Table 3.1 (Moored timeseries courtesy of J. Fischer and F. Schott).

termed internal tides, because (in contrast to the barotropic tides) they do not exhibit an elevation at the sea surface, but cause a vertical displacement of density surfaces in the interior which can amount up to several tens of metres in amplitude. Internal tides travel as waves of tidal frequencies 3-dimensionally through the interior of the oceans. Thus, they radiate energy extracted from the barotropic tide into the ocean's interior, which is subsequently transferred via shear instability and wave breaking to turbulent motions and mixing.

Observations of tidal currents in the deep Greenland Sea are mainly restricted to moorings at the Greenland slope. At 75°N the dominant tidal constituent is the principle lunar ( $M_2$ ) with amplitudes around 4 cm s<sup>-1</sup> near the surface, decreasing with depth. The second most important constituents are the principle solar ( $S_2$ ) and, below 2500 m, the diurnal luni-solar declinational ( $K_1$ ), with amplitudes of around 1 cm s<sup>-1</sup>, respectively (Lam, 1999; Woodgate et al., 1999). Current meter timeseries from the open water above the flanks of Mohns Ridge (Table 5.1) show a similar pattern, but with a diminished amplitude of all components. The diurnal  $K_1$  shows no significant depth dependence at this location. In the upper central Greenland Sea,  $K_1$  is the dominant signal; all other components have amplitudes smaller than 0.5 cm s<sup>-1</sup>.

The topography of the Greenland Sea is highly variable on all scales (cf. Section 4.1 and Figure 4.1) and the scales of motion for the observed tides range from a few hundred metres to a few kilometres; since the generation of internal waves is most efficient where those two scales are in correspondence with each other (Bell, 1975), one can savely assume that large portions of the total area of the Greenland Sea are favourable of the excitation of internal baroclinic tides.

The environment of the Nordic Seas with its location at a high latitude and weak stratification poses some interesting constraints on the internal wave climate and the excitation of baroclinic tides. The dispersion relation for internal waves yields that an internal wave of frequency  $\omega$  can only exist

|       | Tide                       | Period (Frequency)                              | Turning Latitude |
|-------|----------------------------|---|------------------|
| $M_2$ | (Principal lunar)          | 12.42 h ( $1.41 \times 10^{-4} \text{s}^{-1}$ ) | 74.5°            |
| $S_2$ | (Principal solar)          | 12.00 h ( $1.45 \times 10^{-4} \text{s}^{-1}$ ) | 86°              |
| $N_2$ | (Longer lunar elliptic)    | 12.66 h ( $1.38 \times 10^{-4} \text{s}^{-1}$ ) | 71°              |
| $K_2$ | (Luni-solar declinational) | 11.97 h ( $1.46 \times 10^{-4} \text{s}^{-1}$ ) | 89°              |

Tab. 5.2: Semidiurnal tides and their turning latitudes (both hemispheres); diurnal tides cannot exist as free waves in high latitudes. Inertial frequency in the Greenland Sea for comparison:  $1.38 \leq f \leq 1.44 \times 10^{-4} \text{s}^{-1}$ .

if the condition

$$\frac{N^2(z) - \omega^2}{\omega^2 - f^2} > 0$$

is fulfilled (cf. Section 2.1, Equation 2.1), thus the intrinsic frequency of the wave has to fall in the range between the buoyancy and the inertial frequencies. Internal waves can therefore experience different types of boundaries. The vertical propagation can be restricted by the stratification, and the presence of a background shear flow can decrease the intrinsic frequency of a vertical propagating wave and thus lead to critical layer absorption where  $\omega$  approaches  $f$  (Booker and Bretherton, 1967). The limitation by the inertial frequency also poses a restriction on the poleward horizontal propagation of near-inertial waves. Specifically, the wave equation has a singularity at  $\omega = f$ ; for  $\omega > f$ , periodic solutions and thus freely propagating waves are possible, whereas for  $\omega < f$  only exponentially damped solutions in the form of trapped waves exist.

For tides, the latitudes where their respective frequencies equal the local inertial frequency are commonly termed critical or turning latitudes. The turning latitudes of most semi-diurnal tides (summarised in Table 5.2) can be found in or in the vicinity of the Greenland Sea. The excitation of internal tides in the vicinity of critical latitudes should be drastically suppressed according to linear theory. However, there is evidence from fully nonlinear models and observations from the Barents Sea that at critical latitudes nonlinear waves of short wavelengths and tidal frequencies are effectively generated. These nonlinear internal tides are able to freely propagate (Vlasenko et al., 2003). Even poleward of the inertial latitudes, some type of propagating mixed tidal-lee waves can be generated by oscillating tidal flows (Nakamura and Awaji, 2001).

These consideration suggest the existence of two types of internal waves of tidal origin with different propagation characteristics (Figure 5.5) in the Greenland Sea. Firstly the strongly nonlinear short waves excited at or in the vicinity of the critical latitudes of the individual tides. These are not able to travel far and will be dissipated close to their source region, thus contributing to strong turbulent mixing in the boundary layer. Secondly, there are linear internal tides originating farther south of the turning latitudes. Due to their lower wavenumbers, they can propagate through large parts of the Greenland Basin (which is only 400 km in diameter), and contribute to mixing in the

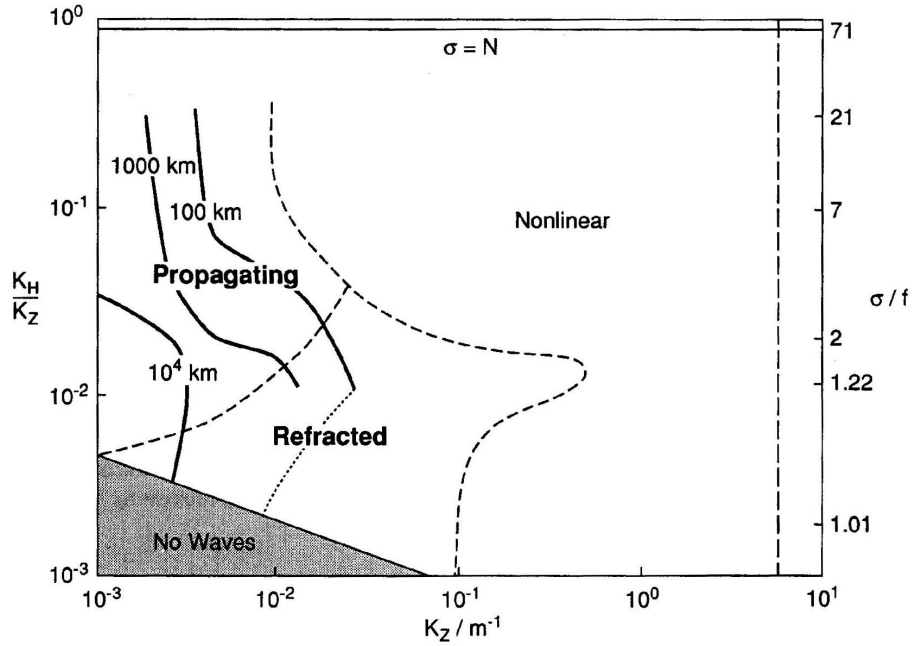


Fig. 5.5: Contour plot of the range of horizontal propagation of internal waves in dependence of vertical wavenumber (x-axis), ratio of horizontal and vertical wavenumber (left) and ratio of the intrinsic frequency of the wave to the local inertial frequency (right). Figure taken from D'Asaro (1991). There are four different domains to distinguish by the response of the waves: Nonlinear waves cannot propagate far because of their strong interaction. Near inertial waves are refracted by interaction with background currents and internal waves. Long distance propagation is limited to low-mode superinertial waves. Lastly, the  $\beta$ -effect prohibits the existence of low-mode inertial waves. Since  $N < 7f$  for most parts of the Greenland Sea, the range of possible waves is restricted to the lower half of the plot; internal waves in the near-inertial range are mostly nonlinear.

interior.

### Spreading and Reflection

The energy flux of internal waves is determined by the direction of the group velocity, which for linear waves can be expressed by the dispersion relation (Equation 2.1) as

$$c = \frac{\beta}{\alpha} = \left( \frac{\omega^2 - f^2}{N^2 - \omega^2} \right)^{1/2}$$

(e.g. Thorpe, 1975). A wave with the intrinsic frequency  $\omega$  will accordingly travel with an inclination  $c = \tan \phi$  (where  $\phi$  is the angle to the horizontal), depending on the local stratification and latitude. The ratio between the bottom slope  $bs$  and the slope of group velocity of an incoming wave determines the spreading direction of the reflected wave. If this ratio  $\gamma = bs/c$  is larger than unity, the reflection is supercritical and the waves are reflected towards deeper water. If the ratio is

smaller, subcritical reflection into shallower water occurs. At critical slopes, where  $\gamma$  equals one, nonlinear effects take over and the wave breaks down into turbulent motion.

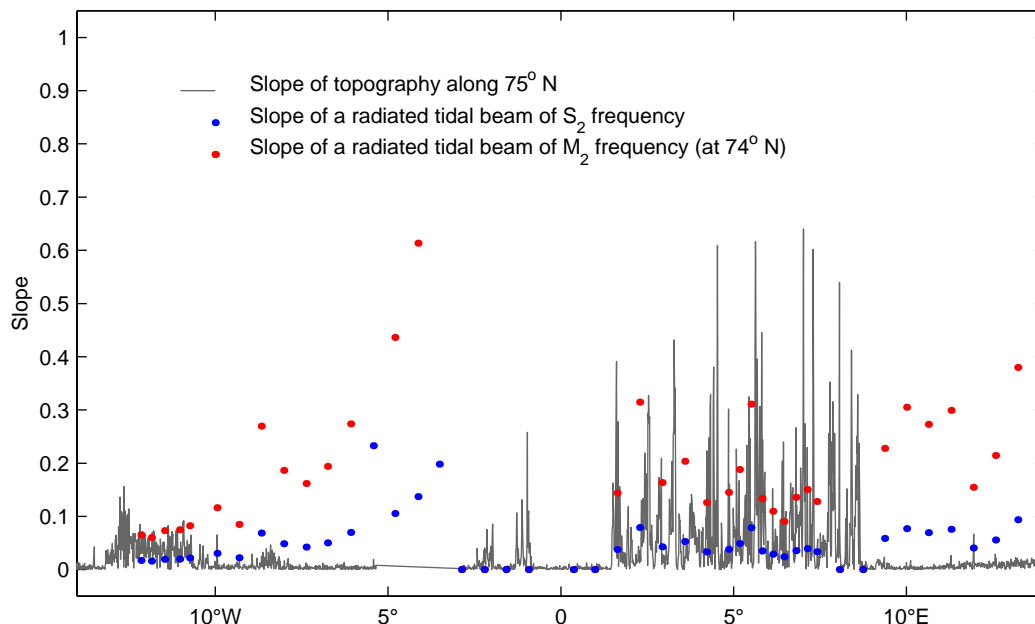


Fig. 5.6: Slope of the topography along 75°N compared to the slope of the radiated beam of the  $M_2$  (blue) and  $S_2$  (red) internal tides. The slope of the tidal beams was computed according to Equation 5.2, using the average stratification of the 150 m above the topography. The near-bottom buoyancy frequency between 3°W and 2°E is smaller than the inertial frequency, resulting in imaginary slopes. Note that 75°N is north of the critical latitude of the  $M_2$  tide; a latitude of 74°N was assumed for the computation. The maximum internal tide generation occurs where the two slopes (tide and topography) are resonant, i.e. where the ratio between them is unity.

As an arbitrary sample from the Greenland Sea, the slope of the topography along the 75°N transect is compared to the beam angles of the two major semidiurnal tides in Figure 5.6. As this transect only serves as an example for the steepness of the topography, the slope of the  $M_2$  tide is included (evaluated at 74°N). It is immediately visible that the ratio  $\gamma$  is supercritical for the large ridge system (2°–8°), and partly for the Greenland slope (west of 10°W). In the central Greenland Sea, the smooth bottom topography and the weak stratification result in subcritical ratios. Therefore, most of the internal tides excited at the ridge systems will travel downwards into the interior, and only a smaller portion will be reflected towards shallower water.

According to Equation 5.2 the spreading of a wave packet is determined by the proportion of its intrinsic frequency relative to the surrounding conditions. For near-inertial waves (as internal semidiurnal tides in the Greenland Sea), the propagation direction is almost horizontal. If a wave packet encounters regions on its path where the surrounding buoyancy frequency approaches their intrinsic frequency, their inclination gets steeper and steeper.

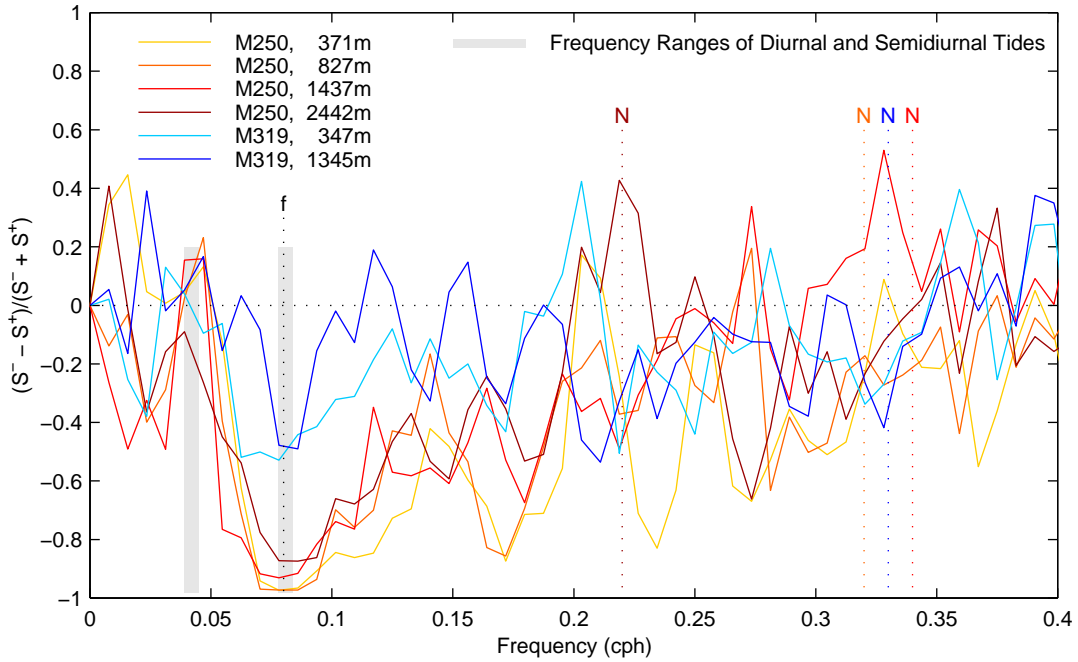


Fig. 5.7: Rotary coefficients from current time series of moorings M319 (blue, central Greenland Sea) and M250 (red, near Mohns Ridge). Also marked in the plot are the inertial frequency  $f$  for the Greenland Sea and the average buoyancy frequencies for the positions and depth range of the current meters (in the same colour as the respective instrument). In the internal wave range between  $f$  and  $N$ , the coefficients are predominantly negative, indicating an upward propagation of energy — noticeable especially in the measurements near the ridge system. (Moored timeseries courtesy of J. Fischer and F. Schott)

Since the weak abyssal stratification is not favourable for the efficient excitation of internal tides, the source regions for the tidal beams will be found at the Greenland slope and the peaks of the submarine ridges in shallow or mid-depth water. Starting with only a small inclination to the horizontal, the tidal beam will propagate into the interior of the basin, where the stratification gets gradually weaker. This in turn will cause it to bend towards the vertical until it reaches the bottom, where it will get either dissipated or reflected. The bottom reflection of internal waves cause a redistribution of spectral energy towards smaller wavelengths and subsequent wave breaking caused by shear instability. This transfer is most effective for sloping, rough bottom topography (Eriksen, 1985; Thorpe, 2001).

Observational evidence for wave spreading away from the boundaries towards the deep interior comes from a comparison of the timeseries from the two mooring locations M250 and M319 (Figure 3.1 and Chapter 3). Rotary spectral analysis was performed on the current meter records to examine whether traces of internal tides were visible in the records. Rotary spectral analysis is a technique invented by Gonella (1972) for the interpretation of vector quantities as e.g. ocean currents. It uses Fourier coefficients to divide a vector time series into a clockwise ( $S^-$ ) and a

counterclockwise ( $S^+$ ) portion. It is a useful tool to determine the sign of the energy flux, because the direction of the group velocity of internal waves determines the sign of the rotary coefficient (Leaman and Sanford, 1975), which is defined as  $rc = (S^- - S^+) / (S^- + S^+)$ . Negative values of  $rc$  denote upward, positive values downward propagation of energy.

Rotary coefficients derived from clockwise and counterclockwise rotary spectra from current meter time series at the two mooring locations M250 and M319 are shown in Figure 5.7. At the ridge (M250), considerable upward energy flux at semidiurnal frequencies ( $\approx 0.08$  cph) denotes the excitation and subsequent radiation of internal baroclinic tides at the local topography. In fact, the group velocity vector is directed upward for the whole internal wave range between  $f$  and  $N$  at this location at all depths, implying a wave generation at a subcritical slope. This is not the case for the mooring records from the centre of the Greenland Basin (M319), which only exhibits a comparatively weak upward flux at the semidiurnal tidal frequencies. Note that there are no instruments in the deep water range available at this position, therefore no statement about the flux in the interior can be made.

#### *Scattering and Dissipation of Wave Energy*

The degradation of the internal tide into turbulent mixing in the interior will be mainly caused by nonlinear interactions and shear instabilities. Shear instabilities preferentially occur at areas where the Richardson number falls below one (cf. Section 4.3); this is the case for large parts of the deep Greenland Sea below 2500 m (Figure 4.4), therefore most of the tidal energy will be dissipated in this depth range.

The proximity of the critical latitude for the semidiurnal tides is of twofold importance for the energy dissipation of internal tides: Firstly, it will contribute to enhanced boundary layer mixing by near-field dissipation of short nonlinear waves as described above. Secondly, there are several indications that the critical latitude in itself will act as an open water “boundary”, with amplified turbulent mixing in its vicinity. For example, there are observations from the Barents Sea, where the existence of a stability minimum and the nutrient distributions at the  $M_2$  critical latitude strongly point towards enhanced mixing (Furevik and Foldvik, 1996). Recent modeling studies from the Weddell Gyre in the Southern Ocean at a similar latitude as the Greenland Sea have shown turbulent diffusivities as high as  $K_\rho \approx 1 \times 10^{-1} \text{ m}^2 \text{ s}^{-1}$  linked to the critical latitudes of the dominant tides (Pereira, 2001). These resemblances suggest strongly that internal tides are the main source of energy for mixing in the polar regions, and that the proximity of critical latitudes may be as strong an agent to induce enhanced mixing as rough topography.



## 6. SUMMARY AND CONCLUSIONS

After the cessation of deep open ocean convection in the early 1980s, transient tracer measurements in the deep and bottom waters of the Greenland Sea have shown a slow but steady ventilation, accompanied with a warming of approximately  $0.1^{\circ}\text{C}$  per year and an increase in salinity. Visbeck and Rhein (2000) proposed that turbulent diapycnal mixing triggered by the rough topography in large parts of the Greenland Sea could be responsible for the observed trends in the deep water properties.

There were indirect indications that the diapycnal diffusivity in the Greenland Sea might be enhanced compared to typical open ocean values of  $K_{\rho} \approx 10^{-5} \text{ m}^2 \text{ s}^{-1}$  and could act as an agent in deep water ventilation. For example, below 2600 m water depth, the exchange with the adjacent basins is prevented by the bathymetry and therefore horizontal advection cannot be responsible for any changes in the lowermost 1000 m of the deep water. For the renewal of the upper layer of the Greenland Sea Gyre, Watson et al. (1999) concluded from their results of the  $SF_6$  release in the late 1990s “*that it may be the rapid year-round turbulent mixing, rather than convection, that dominates vertical mixing in the region as a whole*”.

The results of the present study confirm this view, and extends it towards the deeper layers, which were not affected by convection during the past decades at all. With the aid of two complementary methods, a direct estimate from overturns in density profiles (Thorpe, 1977), and a spectral estimate using the finescale variances of shear and strain as proxies for the energy content of the internal wave field (Gregg, 1989; Polzin et al., 1995), the rates of energy dissipation and subsequently the turbulent diffusivity are computed from temperature, salinity and current measurements. These two methods have different strengths and caveats. The direct estimate of Thorpe scales gives a good vertical resolution of mixing events, but, being a snapshot, only a rough estimate of the actual dissipation rate. Moreover, it hinges on the ratio of density disturbance to background stratification, and for this reason is not applicable for the deep water. The spectral method on the other hand is dependent on several assumptions on the nature of the internal wave field and the energy transfer, which are partially equivocal, the more so as in such a sort of extreme environment as polar seas. To gain reliable results, substantial pieces of shear and density profiles need to be analysed, which reduces the vertical resolution to a minimum. However, with this method it is possible to get full depth profiles of the desired quantities.

The determination of finescale shear with a Lowered ADCP is a relatively new method, that

involves the numerical correction of the attenuation with decreasing wavelengths which is caused by the inherent filtering due to the instrument configuration. The validity of such a correction and general applicability of LADCP data for mixing estimates is not yet widely tested. Therefore, the good agreement between the results from the LADCP and the density inversions in this study is encouraging. The good coverage of LADCP measurements of the world ocean may a good starting point for (albeit rough) diffusivity estimates from a large variety of locations. However, some conditions have to be kept for the successful use: The data quality has to be high; this requires in particular a high abundance of backscatterers (plankton) in the concerned depth range, which can be a serious problem in parts of the tropics and in the subtropics. The other important point is that the instrument settings and the methods of raw data processing have to be well known, and if possible adapted for this special application.

From the observations, there exists a clear distinction between two mixing regimes in the Greenland Sea Gyre: The convectively mixed layer and the deep water, with a comparatively slow exchange between the two in the vertical. The processes and distribution of the ventilation of the Greenland Sea are summarised in Figure 6.1.

In the convectively mixed layer, mid-depth convection in wintertime results in a pool of very cold, fresh water in the centre of the Greenland Sea Gyre. At the same time, instabilities at the front between this cold water pool and the Atlantic inflow on the one hand and the East Greenland Current on the other hand lead to year round mixing across the boundaries between warm saline and well ventilated water masses and the interior. The diapycnal diffusivities in this frontal zones fall between  $K_\rho = 1 - 5 \times 10^{-3} \text{ m}^2 \text{ s}^{-1}$ , while in the interior of the gyre they are smaller, with the minimum across the layer of the stability maximum. Only moderate diffusivities between  $10^{-5} \text{ m}^2 \text{ s}^{-1}$  and  $10^{-4} \text{ m}^2 \text{ s}^{-1}$  are found in the upper layer of the adjacent basin, belonging to the Norwegian Sea. The property transport in the Greenland Sea associated with the observed diapycnal mixing is a downward flux of heat, salinity and anthropogenic tracers like CFCs, which is consistent with observations. The strength of this downward mixing of Atlantic water masses is dependent on the kinetic energy of the flow fields of the East Greenland and the West Spitsbergen Currents, and therefore probably subject to interannual variability driven by the variability of the forcing.

A combination of boundary and interior mixing is found in the deep water domain. The diffusivities are generally elevated above  $K_\rho = 10^{-3} \text{ m}^2 \text{ s}^{-1}$ , with an increase towards the bottom. The average of the diffusivities of  $K_\rho = 1.2 \times 10^{-3} \text{ m}^2 \text{ s}^{-1}$  across the 2000 m isobath is sufficiently high to explain the observed trends in the deep water, if mixing in the bottom boundary layer and horizontal exchange is taken into account. The distribution of the observed eddy diffusivities differs from those found in other locations, where strong mixing was directly associated with rough topography. In this study, high diffusivities are found throughout the deep basin, with a moderate increase near the ridge systems. This is probably an effect of the unique environment of the

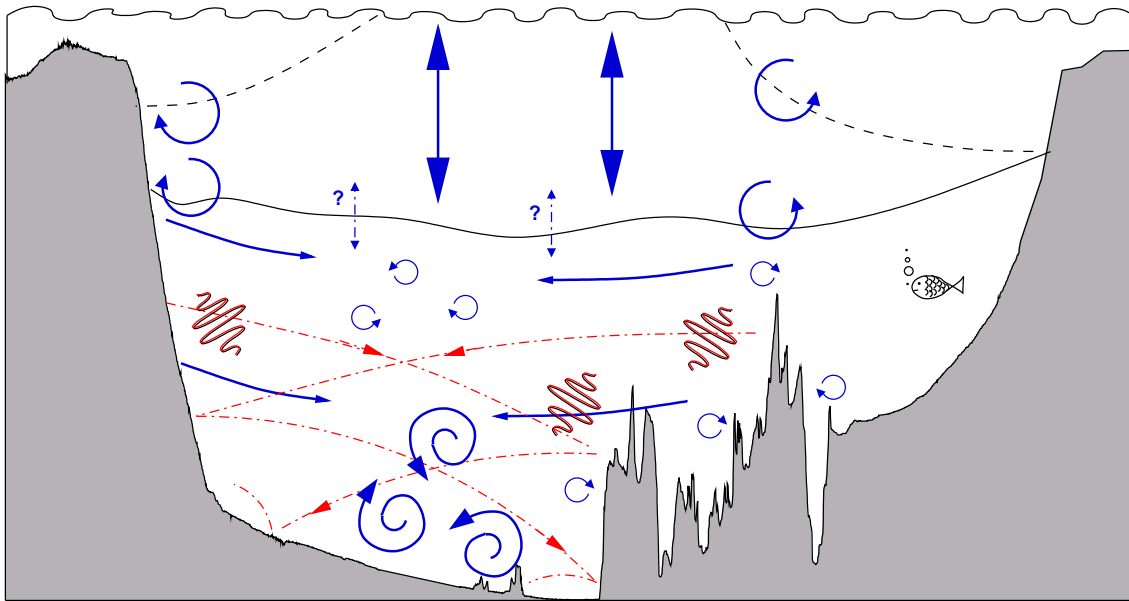


*Fig. 6.1:* Conceptual sketch of the mixing in the Greenland Sea. Blue arrows denote the motion of water parcels, red arrows indicate spreading rays of internal wave groups. Also indicated are the boundaries between the convectively ventilated layer and the deep water (black) and the interior of the gyre and the warm saline Atlantic Water (dashed black). See text for details.

Greenland Sea, and can be explained by the nature of the forcing and the local conditions.

The energy source for this deep mixing is likely provided by tidal currents. The geographical location of the Greenland Sea entails the critical latitudes of most semidiurnal tides, which has a twofold effect on the distribution of the mixing. Close to the respective critical latitude, nonlinear waves of short wavelength will be excited instead of a proper baroclinic tide. These are rapidly dissipated, and therefore contribute to the boundary mixing. On the other hand, freely propagating internal tides originating at the ridges farther south will experience the turning latitude as a boundary and contribute to the high mixing in the interior by locally occurring nonlinearities. The existence of propagating baroclinic tides in the interior is backed up by the high shear to strain ratios found in the interior of the basin, which indicate a dominance of near-inertial frequencies. The shape of the shear as well as of the strain spectra with their increases towards higher wavenumbers is pointing towards a high proportion of internal waves which were reflected after a contact with the bottom or a lateral boundary. This can be attributed to the bowl like shape of the Greenland Basin and its small horizontal extent, which makes it likely for a low mode wave to encounter a boundary.

The weak abyssal stratification in the centre of the Greenland Sea Gyre is also a trigger for the high mixing in this region. Together with the relatively strong current shear, it creates an environment with Richardson numbers which frequently fall below the critical value of 0.25, where

small perturbations can become turbulent.

The benthic storms observed in mooring records near the bottom of the Greenland Sea (Woodgate and Fahrback, 1999) represent an additional (localised) process which can promote the enhanced mixing rates in the abyss by triggering inertial oscillations, but their effect is difficult to quantify because of their intermittency in space and time. Theoretical considerations of the effect of critical layers in the vertical (Bell, 1975) predict that the existence of intense near-bottom currents may considerably increase abyssal mixing coefficients by generating internal waves which are effectively trapped and dissipated near the bottom.

Some of the results of this study challenge the universality of the commonly used parameterisations. The superproportional increase of the eddy diffusivities with depth compared to the dissipation rates strongly suggests that there is a dependency of the mixing efficiency on the initial stratification. If this is the case, it is of importance for large parts of the abyss of the world ocean. Monitoring the further development of the spreading of the dye from the Tracer Release Experiment into greater depth will shed light on the question whether the high abyssal diffusivities are for real or whether they are partly an artificial product of the parameterisation.

The main result of this study concerning the distribution of mixing in the ocean in general is that there is more to cause enhanced mixing than rough topography. It provides observational evidence for the notion that mixing can occur at different sorts of boundaries, in this case the critical latitudes of the semidiurnal tides. These particular sort of boundary may be of even greater global importance in the Southern Ocean, where the critical latitudes are found in the Ross and Weddell Seas. These are directly connected to the global overturning circulation, and therefore enhanced vertical mixing in these areas can add significantly to the total balance required to maintain the stratification in the world ocean.

## APPENDIX



## A. THE GARRETT AND MUNK SPECTRUM OF INTERNAL WAVES

### Shear

Garrett and Munk Spectrum for Internal Waves (Garrett and Munk, 1972, 1975) with the modifications of Cairns and Williams (1976) as in Gregg and Kunze (1991): To derive the shear spectrum  $\phi_s$ , one first has to compute the spectrum of horizontal velocity,  $\phi_u$ , depending on the vertical wavenumber

$$\beta = \frac{\pi j}{b} \left( \frac{N}{N_0} \right) \quad (\text{A.1})$$

$$\phi_u(\beta) = \frac{3Eb^3N_0^2}{2j_*\pi} \frac{1}{(1 + \beta/\beta_*)^2} \quad (\text{A.2})$$

With  $E = 6.3 \times 10^{-5}$  a dimensionless energy level,  $N_0 = 0.0054 \text{ rad s}^{-1}$  the buoyancy frequency,  $b = 1300 \text{ m}$  the scale depth of the stratification with  $N = N_0 e^{-\frac{|z|}{b}}$ ,  $j_* = 3$  reference mode number and  $\beta_* = \frac{\pi j_*}{b} \left( \frac{N}{N_0} \right)$  the reference wave number. Multiplication by  $\beta^2$  yields the spectrum of vertical shear.

$$\phi_s(\beta) = \beta^2 \phi_u \quad (\text{A.3})$$

To obtain the variance of the shear  $\langle S^2 \rangle$  over a certain range of wavenumber, the spectrum has to be integrated over the desired range, e.g. to an upper limit wavenumber  $\beta_u$ .

$$\langle S^2 \rangle = \frac{3Eb^3N_0^2}{2j_*\pi} \int_0^{\beta_u} \frac{\beta^2}{(1 + \beta/\beta_*)^2} d\beta \quad (\text{A.4})$$

with the integral

$$\int_0^{\beta_u} \frac{\beta^2}{(1 + \beta/\beta_*)^2} d\beta = \beta_*^3 \left[ 1 + \frac{\beta_u}{\beta_*} - 2 \ln \left( 1 + \frac{\beta_u}{\beta_*} \right) + \frac{1}{1 + \beta_u/\beta_*} \right]. \quad (\text{A.5})$$

For values  $\beta_u/\beta_* \geq 100$  the integral equals  $\beta_u \beta_*^2$  within 10%, and substituting  $\beta$  from Equation A.1 then yields the simplified expression

$$\langle S^2 \rangle = \frac{3EbN_0^2 j_* \pi \beta_u}{2} \left( \frac{N}{N_0} \right)^2. \quad (\text{A.6})$$

The criterion  $\beta_u/\beta_* \geq 100$  poses a strong restriction on the use of the above. The integration

of Lowered ADCP shear spectra is limited to an upper wavenumber boundary of  $\beta_u = 0.126 \text{ rad m}^{-1}$  (corresponding to 50 m wavelength); this implies for the buoyancy frequency extremely small values of  $N \leq 0.00091 \text{ rad s}^{-1}$  (or 0.52 cph) which are rarely met, even in such a weakly stratified environment as the Greenland Sea. Therefore, in this study Expression A.5 is employed.

### *Strain*

Same reasoning applied to strain spectra:

Spectrum of vertical displacement  $\zeta$  is

$$\phi_\zeta(\beta) = \frac{Eb^3}{2\pi j_*} \left( \frac{N_0}{N} \right)^2 \frac{1}{(1 + \beta/\beta_*)^2} \quad (\text{A.7})$$

and vertical strain (analogous to shear)

$$\phi_\lambda(\beta) = \beta^2 \phi_\zeta(\beta) \quad (\text{A.8})$$

and then,

$$\langle \lambda^2 \rangle = \frac{\pi Eb j_* \beta_u}{2} \quad (\text{A.9})$$

this leads to a shear to strain ratio of

$$\frac{\langle S^2 \rangle}{\langle \lambda^2 \rangle} = 3N^2 \quad (\text{A.10})$$

| Symbol            | Dimension                                      |   |
|-------------------|--|---|
| <i>Variables</i>  |  |   |
| $\beta$           | $\text{rad m}^{-1}$                            | Wave number                               |
| $k(= \beta/2\pi)$ | cpm  | Cyclic wave number                        |
| $N$               | $\text{rad s}^{-1}$                            | Buoyancy frequency                        |
| $j$               |  | Mode number                               |
| $\phi_s$          |  | Shear spectral density                    |
| $\phi_u$          |  | Spectral density of horizontal velocity   |
| $\phi_\lambda$    |  | Spectral density of vertical strain       |
| $\phi_\zeta$      |  | Spectral density of vertical displacement |
| $\omega$          | $\text{rad s}^{-1}$                            | Frequency                                 |
| $f$               | $2 \times 7.3 \times 10^{-5} \sin(\text{lat})$ | Coriolis parameter                        |
| <i>Parameters</i> |  |   |
| $N_0$             | $0.0054 \text{ rad s}^{-1}$                    |   |
| $b$               | 1300 m   |   |
| $j_*$             | 3  | Reference mode number                     |
| $\beta_*$         |  | Reference wave number                     |
| $\beta_u$         |  | wave number                               |
| $E$               | $6.3 \times 10^{-5}$                           | Dimensionless energy level                |
| $f_0$             | $2 \times 7.3 \times 10^{-5} \sin(32.5^\circ)$ | Reference coriolis parameter              |

Tab. A.1: Overview of Parameters and Variables used in the GM Internal Wave Model



## B. LIST OF ABBREVIATIONS

*ADCP* Acoustic Doppler Current Profiler

*AW* Atlantic Water

*BBL* Bottom Boundary Layer

*CFCs* Chlorofluorocarbons

*CTD* Conductivity Temperature Depth Probe

*EBDW* Eurasian Basin Deep Water

*EGC* East Greenland Current

*GSDW* Greenland Sea Deep Water

*GSP* Greenland Sea Project

*HRP* High Resolution Profiler

*LADCP* Lowered Acoustic Doppler Current Profiler

*MAR* Mid-Atlantic Ridge

*NAC* Norwegian Atlantic Current

*NADW* Nord Atlantic Deep Water

*NAO* North Atlantic Oscillation

*NSDW* Norwegian Sea Deep Water

*PW* Polar Water

*rAW* Return Atlantic Water

*Ri* Richardson Number

*SF<sub>6</sub>* Sulphur Hexafluoride

*SML* Surface Mixed Layer

*THC* Thermohaline Circulation

*TKE* Turbulent Kinetic Energy

*WSC* West Spitsbergen Current

*XCP* Expendable Current Profiler

## BIBLIOGRAPHY

- Aagaard, K. (1968). Temperature variations in the Greenland Sea Deep Water. *Deep-Sea Research*, 15:281–296.
- Aagaard, K., Fahrbach, E., Meincke, J., and Swift, J. (1991). Saline outflow from the Arctic Ocean: Its contribution to the deep waters of the Greenland, Norwegian, and Iceland Seas. *Journal of Geophysical Research*, 96(C11):20,433–20,441.
- Aagaard, K., Swift, J., and Carmack, E. (1985). Thermohaline circulation in the Arctic Mediterranean Seas. *Journal of Geophysical Research*, 90(C3):4833–4846.
- Bell, T. (1975). Topographically generated internal waves in the open ocean. *Journal of Geophysical Research*, 80(3):320–327.
- Bönisch, G., Blindheim, J., Bullister, J., Schlosser, P., and Wallace, D. (1997). Long-term trends of temperature, salinity, density, and transient tracers in the central Greenland Sea. *Journal of Geophysical Research*, 102(C8):18,553–18,571.
- Booker, J. and Bretherton, F. (1967). Critical layer for internal gravity waves in a shear flow. *Journal of Fluid Mechanics*, 27:513–539.
- Bray, N. and Fofonoff, N. (1981). Available potential energy for MODE eddies. *Journal of Physical Oceanography*, 11(1):30–46.
- Briscoe, M. (1975). Preliminary results from the trimoored internal wave experiment (IWEX). *Journal of Geophysical Research*, 80(27):3872–3884.
- Budéus, G., Maul, A.-A., and Krause, G. (1993). Variability in the Greenland Sea as revealed by a repeated high spatial resolution Conductivity–Temperature–Depth survey. *Journal of Geophysical Research*, 98(C6):9985–10,000.
- Budéus, G., Schneider, W., and Krause, G. (1998). Winter convective events and bottom water warming in the Greenland Sea. *Journal of Geophysical Research*, 103(C9):18,513–18,527.
- Bullister, J. and Weiss, R. (1983). Anthropogenic chlorofluoromethanes in the Greenland and Norwegian Seas. *Science*, 221:265–268.

- Cairns, J. and Williams, G. (1976). Internal wave observations from a midwater float, 2. *Journal of Geophysical Research*, 81(12):1943–1950.
- Carmack, E. and Aagaard, K. (1973). On the deep water of the Greenland Sea. *Deep-Sea Research*, 20:687–715.
- Carter, G. and Gregg, M. (2002). Intense, variable mixing near the head of Monterey submarine canyon. *Journal of Physical Oceanography*, 32(11):3145–3165.
- Clarke, R., Swift, J., Reid, J., and Koltermann, K. (1990). The formation of Greenland Sea Deep Water: Double diffusion or deep convection? *Deep-Sea Research*, 37(9):1385–1424.
- Crawford, W. (1986). A comparison of length scales and decay times of turbulence in stably stratified flows. *Journal of Physical Oceanography*, 16(11):1847–1854.
- D'Asaro, E. (1991). A strategy for investigating and modeling internal wave sources and sinks. In Müller, P. and Henderson, D., editors, *'Aha Huliko'a: Dynamics of Oceanic Internal Gravity Waves*. University of Hawaii at Manoa, SOEST Special Publications. Proceedings 'Aha Huliko'a Hawaiian Winter Workshop.
- Davis, R. (1994a). Diapycnal mixing in the ocean: Equations for large-scale budgets. *Journal of Physical Oceanography*, 24(4):777–800.
- Davis, R. (1994b). Diapycnal mixing in the ocean: The Osborn–Cox model. *Journal of Physical Oceanography*, 24(12):2560–2576.
- Delworth, T., Manabe, S., and Stouffer, R. (1993). Interdecadal variations of the thermohaline circulation in a coupled ocean-atmosphere model. *Journal of Climate*, 6(11):1993–2011.
- Delworth, T., Manabe, S., and Stouffer, R. (1997). Multidecadal climate variability in the Greenland Sea and surrounding regions: A coupled model simulation. *Geophysical Research Letters*, 24(3):257–260.
- Dengler, M. (2000). Über die Tiefenzirkulation und die vertikale Vermischung im nordwestlichen Indischen Ozean. Dissertation, Institut für Meereskunde, Hamburg.
- Dengler, M. and Quadfasel, D. (2002). Equatorial deep jets and abyssal mixing in the Indian Ocean. *Journal of Physical Oceanography*, 32(4):1165–1180.
- Dickson, R., Gmitrowicz, E., and Watson, A. (1990). Deep-water renewal in the northern North Atlantic. *Nature*, 344:848–850.

- Dickson, R., Lazier, J., Meincke, J., Rhines, P., and Swift, J. (1996). Long-term coordinated changes in the convective activity of the North Atlantic. *Progress in Oceanography*, 38:241–295.
- Dillon, T. (1982). Vertical overturns: A comparison of Thorpe and Ozmidov length scales. *Journal of Geophysical Research*, 87(C12):9601–9613.
- Duda, T. and Cox, C. (1989). Vertical wave number spectra of velocity and shear at small internal wave scales. *Journal of Geophysical Research*, 94(C2):939–950.
- Egbert, G. and Ray, R. (2000). Significant dissipation of tidal energy in the deep ocean inferred from satellite altimeter data. *Nature*, 405:775–778.
- Ellison, T. (1957). Turbulent transport of heat and momentum from an infinite rough plane. *Journal of Fluid Mechanics*, 2:456–466.
- Eriksen, C. (1981). Deep currents and their interpretation as equatorial waves in the western Pacific Ocean. *Journal of Physical Oceanography*, 11(1):48–70.
- Eriksen, C. (1982). Observations of internal wave reflection off sloping bottoms. *Journal of Geophysical Research*, 87:525–538.
- Eriksen, C. (1985). Implication of ocean bottom reflection for internal wave spectra and mixing. *Journal of Physical Oceanography*, 15(9):1145–1156.
- Fahrbach, E., editor (1999). *The Expedition ARKTIS XIV/2 of the Research Vessel "Polarstern" in 1998*. Alfred–Wegener–Institut für Polar- und Meeresforschung, Berichte zur Polarforschung 326.
- Fer, I. and Haugan, P. (2003). Mixing of the dense Storfjord plume inferred from Thorpe scale analysis. In *Geophysical Research Abstracts*, volume 5, page 03936. European Geophysical Society.
- Ferron, B., Mercier, H., Speer, K., Gargett, A., and Polzin, K. (1998). Mixing in the Romanche Fracture Zone. *Journal of Physical Oceanography*, 28(10):1929–1944.
- Finnigan, T., Luther, D., and Lukas, R. (2002). Observations of enhanced diapycnal mixing near the Hawaiian Ridge. *Journal of Physical Oceanography*, 32(11):2988–3002.
- Firing, E. (1998). Lowered ADCP development and use in WOCE. *WOCE Newsletter*, 30:10–14.
- Fischer, J. and Visbeck, M. (1993). Deep velocity profiling with self-containing ADCPs. *Journal of Atmospheric and Oceanic Technology*, 10:764–773.

- Fofonoff, N. (1969). Spectral characteristics of internal waves in the ocean. *Deep-Sea Research*, 16(suppl.):58–71.
- Fohrmann, H., Backhaus, J., Blaume, F., and Rumohr, J. (1998). Sediments in bottom-arrested gravity plumes: Numerical case studies. *Journal of Physical Oceanography*, 28(11):2250–2274.
- Foldvik, A., Aagaard, K., and Tørresen, T. (1988). On the velocity field of the East Greenland Current. *Deep-Sea Research*, 35:1335–1354.
- Foster, T. and Carmack, E. (1976). Temperature and salinity structure in the Weddell Sea. *Journal of Physical Oceanography*, 6:36–44.
- Furevik, T. and Foldvik, A. (1996). Stability at  $M_2$  critical latitude in Barents Sea. *Journal of Geophysical Research*, 101(C4):8823–8837.
- Gargett, A. (1990). Do we really know how to scale the turbulent kinetic energy dissipation rate  $\epsilon$  due to breaking of oceanic internal waves? *Journal of Geophysical Research*, 95(C9):15,971–15,974.
- Gargett, A., Hendricks, P., Sanford, T., Osborn, T., and Williams III, A. (1981). A composite spectrum of vertical shear in the upper ocean. *Journal of Physical Oceanography*, 11(9):1258–1271.
- Gargett, A. and Holloway, G. (1984). Dissipation and diffusion by internal wave breaking. *Journal of Marine Research*, 42:15–27.
- Gargett, A. and Moum, J. (1995). Mixing efficiencies in turbulent tidal fronts: Results from direct and indirect measurements of density flux. *Journal of Physical Oceanography*, 25(11):2583–2608.
- Garrett, C. and Munk, W. (1972). Space-time scales of internal waves. *Geophysical Fluid Dynamics*, 2:225–264.
- Garrett, C. and Munk, W. (1975). Space-time scales of internal waves: A progress report. *Journal of Geophysical Research*, 80(3):291–297.
- Garrett, C. and St.Laurent, L. (2002). Aspects of deep ocean mixing. *Journal of Oceanography*, 58:11–24.
- Gascard, J.-C., Watson, A., Messias, M.-J., Olsson, K., Johannessen, T., and Simonsen, K. (2002). Long-lived vortices as a mode of deep ventilation in the Greenland Sea. *Nature*, 416:525–527.
- Gonella, J. (1972). A rotary-component method for analysing meteorological and oceanographic vector time series. *Deep-Sea Research*, 19:833–846.

- Gregg, M. (1987). Diapycnal mixing in the thermocline: A review. *Journal of Geophysical Research*, 92(C5):5249–5286.
- Gregg, M. (1989). Scaling turbulent dissipation in the thermocline. *Journal of Geophysical Research*, 94(C7):9686–9698.
- Gregg, M. and Kunze, E. (1991). Shear and strain in Santa Monica basin. *Journal of Geophysical Research*, 96(C9):16,709–16,719.
- Gregg, M., Sanford, T., and Winkel, D. (2003). Reduced mixing from the breaking of internal waves in equatorial waters. *Nature*, 422:513–515.
- Gregg, M., Winkel, P., and Sanford, T. (1993). Varieties of fully resolved spectra of vertical shear. *Journal of Physical Oceanography*, 23(1):124–141.
- GSP Group (1990). A venture towards improved understanding of the ocean's role in climate. *EOS, Transactions, AGU*, 71(24):750–751, 754–755.
- Hansen, B. and Østerhus, S. (2000). North Atlantic—Nordic Seas exchanges. *Progress in Oceanography*, 45:109–208.
- Hasumi, H. and Sugimotohara, N. (1999). Effects of locally enhanced vertical diffusivity over rough bathymetry on the world ocean circulation. *Journal of Geophysical Research*, 104(C10):23,367–23,374.
- Helland-Hansen, B. and Nansen, F. (1909). The Norwegian Sea: Its physical oceanography based upon the Norwegian researches 1900—1904. *Report on Norwegian Fishery and Marine Investigations*, 2(2):390pp.
- Henye, F., Wright, J., and Flatté, S. (1986). Energy and action flow through the internal wave field: An eikonal approach. *Journal of Geophysical Research*, 91:8487–8495.
- Hurdle, B., editor (1986). *The Nordic Seas*. Springer Verlag, New York.
- Hurrell, J. (1995). Decadal trends in the North Atlantic Oscillation: Regional temperatures and precipitation. *Science*, 269:676–679.
- IBCAO (2000). International bathymetric chart of the Arctic Ocean .  
<http://www.ngdc.noaa.gov/mgg/bathymetry/arctic/arctic.html>.
- Jones, P., Jónsson, T., and Wheeler, D. (1997). Extension to the North Atlantic Oscillation using early instrument pressure observations from Gibraltar and south-west Iceland. *International Journal of Climatology*, 17:1433–1450.

- Jónsson, S. (1991). Seasonal and interannual variability of wind stress curl over the Nordic Seas. *Journal of Geophysical Research*, 96(C2):2649–2659.
- Kämpf, J., Backhaus, J., and Fohrmann, H. (1999). Sediment-induced slope convection: Two-dimensional numerical case studies. *Journal of Geophysical Research*, 104:20,509–20,522.
- Killworth, P. (1979). On “chimney” formation in the ocean. *Journal of Physical Oceanography*, 9(3):531–554.
- Kunze, E. (1985). Near-inertial wave propagation in geostrophic shear. *Journal of Physical Oceanography*, 15(5):544–565.
- Kunze, E., Rosenfeld, L., Carter, G., and Gregg, M. (2002). Internal waves in Monterey submarine canyon. *Journal of Physical Oceanography*, 32(6):1890–1913.
- Kunze, E. and Sanford, T. (1996). Abyssal mixing: Where it is not. *Journal of Physical Oceanography*, 26(10):2286–2296.
- Kunze, E. and Toole, J. (1997). Tidally driven vorticity, diurnal shear, and turbulence atop Fieberling Seamount. *Journal of Physical Oceanography*, 27(12):2663–2693.
- Kunze, E., Williams III, A., and Briscoe, M. (1990). Observations of shear and vertical stability from a neutrally buoyant float. *Journal of Geophysical Research*, 95(C10):18,127–18,142.
- Lam, F.-P. (1999). Shelf waves with diurnal tidal frequency at the Greenland shelf edge. *Deep-Sea Research*, I 46:895–923.
- Leaman, K. and Sanford, T. (1975). Vertical energy propagation of internal waves: A vector spectral analysis of velocity profiles. *Journal of Geophysical Research*, 80(15):1975–1978.
- Ledwell, J., Montgomery, E., Polzin, K., St. Laurent, L., Schmitt, R., and Toole, J. (2000). Evidence for enhanced mixing over rough topography in the abyssal ocean. *Nature*, 403:179–182.
- Ledwell, J., Watson, A., and Law, C. (1993). Evidence of slow mixing across the pycnocline from an open-ocean tracer-release experiment. *Nature*, 364:701–703.
- Ledwell, J., Watson, A., and Law, C. (1998). Mixing of a tracer in the pycnocline. *Journal of Geophysical Research*, 103(C10):21,499–21,529.
- Levine, M. (2002). A modification of the Garrett–Munk internal wave spectrum. *Journal of Physical Oceanography*, 32(11):3166–3181.
- Lilly, J. and Rhines, P. (2002). Coherent eddies in the Labrador Sea observed from a mooring. *Journal of Physical Oceanography*, 32:585–598.

- Marotzke, J. (1997). Boundary mixing and the dynamics of three-dimensional thermohaline circulation. *Journal of Physical Oceanography*, 27(8):1713–1728.
- Mauritzen, C. (1996a). Production of dense overflow waters feeding the North Atlantic across the Greenland–Scotland ridge. Part 1: Evidence for a revised circulation scheme. *Deep-Sea Research*, I 43(6):769–806.
- Mauritzen, C. (1996b). Production of dense overflow waters feeding the North Atlantic across the Greenland–Scotland ridge. Part 2: An inverse model. *Deep-Sea Research*, I 43(6):807–835.
- Mauritzen, C., Polzin, K., McCartney, M., Millard, R., and West-Mack, D. (2002). Evidence in hydrography and density fine structure for enhanced vertical mixing over the Mid-Atlantic Ridge in the western Atlantic. *Journal of Geophysical Research*, 107(C10):10.1029/2001JC001114.
- McComas, C. and Müller, P. (1981). The dynamic balance of internal waves. *Journal of Physical Oceanography*, 11(7):970–986.
- McDougall, T. (1983). Greenland Sea Bottom Water formation: A balance between advection and double-diffusion. *Deep-Sea Research*, 30(11A):1109–1117.
- Meincke, J. and Rudels, B. (1995). Greenland Sea Deep Water: A balance between convection and advection. In *Nordic Seas Symposium, Extended Abstracts*, pages 143–147. Arctic Ocean Sciences Board.
- Mertens, C. (2000). Open–ocean convection in the Labrador and Greenland Seas: Plume scales and interannual variability. Dissertation, Institut für Meereskunde, Kiel.
- Metcalf, W. (1955). On the formation of bottom water in the Norwegian Basin. *Transactions of the American Geophysical Union*, 36(4):595–600.
- Miles, J. (1961). On the stability of heterogeneous shear flows. *Journal of Fluid Mechanics*, 10:496–508.
- Millard, R., Owens, W., and Fofonoff, N. (1990). On the calculation of the Brunt–Väisälä frequency. *Deep-Sea Research*, 37(1):167–181.
- Mohn, H. (1887). Nordhavets dybder, temperatur og strømninger. *Den Norske Nordhavs-Expeditionen 1876—1878*, 18:212pp.
- Mork, K. and Blindheim, J. (2000). Variations in Atlantic inflow to the Nordic Seas 1955–1996. *Deep-Sea Research*, 47A(6):1035–1057.
- Morris, M., Hall, M., St. Laurent, L., and Hogg, N. (2001). Abyssal mixing in the Brasil Basin. *Journal of Physical Oceanography*, 31(11):3331–3348.

- Moum, J. (1990). The quest for  $K_\rho$  – preliminary results from direct measurements of turbulent fluxes in the ocean. *Journal of Physical Oceanography*, 20(12):1980–1984.
- Müller, P., Olbers, D., and Willebrand, J. (1978). The IWEX spectrum. *Journal of Geophysical Research*, 83(C1):479–500.
- Munk, W. (1966). Abyssal recipes. *Deep-Sea Research*, 13:707–730.
- Munk, W. (1981). Internal waves and small-scale processes. In Warren, B. and Wunsch, C., editors, *Evolution of Physical Oceanography*, pages 264–291. The MIT Press.
- Munk, W. and Wunsch, C. (1998). Abyssal recipes II: Energetics of tidal and wind mixing. *Deep-Sea Research*, 45:1977–2010.
- Nakamura, T. and Awaji, T. (2001). A growth mechanism for topographic internal waves generated by an oscillatory flow. *Journal of Physical Oceanography*, 31(8):2511–2524.
- Nansen, F. (1902). The oceanography of the North Polar Basin. *Norwegian Polar Expedition 1893–1896, Scientific Results*, 2(9):427pp.
- Nansen, F. (1906). Northern waters: Captain Roald Amundsen’s oceanographic observations in the Arctic Seas in 1901. With a discussion of the of the bottom waters of the northern seas. *Videnskabselskabets Skrifter, Matematisk–Naturvidenskabelig Klasse*, 1(3):145pp.
- National Geophysical Data Center (2001). ETOPO-2 global elevation and bathymetry .  
<ftp://dss.ucar.edu/datasets/ds759.3/>.
- Oakey, N. (1982). Determination of the rate of dissipation of turbulent energy from simultaneous temperature and velocity shear microstructure measurements. *Journal of Physical Oceanography*, 12(3):256–271.
- Olbers, D. (1983). Models of the oceanic internal wave field. *Reviews of Geophysics and Space Physics*, 21(7):1567–1606.
- Osborn, T. (1980). Estimates of the local rate of vertical diffusion from dissipation measurements. *Journal of Physical Oceanography*, 10(1):83–89.
- Østerhus, S. and Gammelsrød, T. (1999). The abyss of the Nordic Seas is warming. *Journal of Climate*.
- Otterå, O., Drange, H., Bentsen, M., Kvamstø, N., and Jiang, D. (2003). The sensitivity of the present-day Atlantic meridional overturning circulation to freshwater forcing. *Geophysical Research Letters*, 30(17):10.1029/2003GL017578.

- Ozmidov, R. (1965). On the turbulent exchange in a stably stratified ocean. *Atmos. Ocean. Phys.*, 8:853–860.
- Pawlowicz, R., Lynch, J., Owens, W., Worcester, P., Morawitz, W., and Sutton, P. (1995). Thermal evolution of the Greenland Sea gyre in 1988-1989. *Journal of Geophysical Research*, 100(C3):4727–4750.
- Pereira, A. (2001). Numerical investigation of tidal processes and phenomena in the Weddell Sea, Antarctica. Dissertation, Alfred-Wegener-Institut Bremerhaven, Bremen.
- Peters, H., Gregg, M., and Sandford, T. (1995). On the parameterization of equatorial turbulence: Effect of fine-scale variations below the range of the diurnal cycle. *Journal of Geophysical Research*, 100(C9):18.333–18.348.
- Peterson, W. and Rooth, C. (1976). Formation and exchange of deep water in the Greenland and Norwegian Seas. *Deep-Sea Research*, 23:273–283.
- Polzin, K. (1996). Statistics of the Richardson number: Mixing models and finestructure. *Journal of Physical Oceanography*, 26(8):1409–1425.
- Polzin, K. and Firing, E. (1997). Estimates of diapycnal mixing using LADCP and CTD data from I8S. *WOCE Newsletter*, 29:39–42.
- Polzin, K., Kunze, E., Hummon, J., and Firing, E. (2002). The finescale response of Lowered ADCP velocity profiles. *Journal of Atmospheric and Oceanic Technology*, 19(2):205–224.
- Polzin, K., Kunze, E., Toole, J., and Schmitt, R. (2003). The partition of finescale energy into internal waves and subinertial motions. *Journal of Physical Oceanography*, 33(1):234–248.
- Polzin, K., Speer, K., Toole, J., and Schmitt, R. (1996). Intense mixing of Antarctic Bottom Water in the equatorial Atlantic Ocean. *Nature*, 380:54–57.
- Polzin, K., Toole, J., Ledwell, J., and Schmitt, R. (1997). Spatial variability of turbulent mixing in the abyssal ocean. *Science*, 276:93–96.
- Polzin, K., Toole, J., and Schmitt, R. (1995). Finescale parameterizations of turbulent dissipation. *Journal of Physical Oceanography*, 25(3):306–328.
- Quadfasel, D., Rudels, B., and Kurz, K. (1988). Outflow of dense water from a Svalbard fjord into Fram Strait. *Deep-Sea Research*, 35(7):1143–1150.
- Rahmstorf, S. (2002). Ocean circulation and climate during the past 120.000 years. *Nature*, 419:207–214.

- RDI (1996). Acoustic Doppler Current Profiler—principles of operation: A practical primer. Technical report, RD Instruments.
- Rhein, M. (1991). Ventilation rates of the Greenland and Norwegian Seas derived from distributions of the chlorofluoromethanes F11 and F12. *Deep-Sea Research*, 38(4):485–503.
- Rhein, M. (1996). Convection in the Greenland Sea, 1982–1993. *Journal of Geophysical Research*, 101(C8):18,183–18,192.
- Richardson, L. (1923). The supply of energy from and to atmospheric eddies. *Philos. Trans. Roy. Soc. London*, A97:354–373.
- Ronski, S. (2002). Ventilation der Grönlandsee – Variabilität und ihre Ursachen 1994–2001. Dissertation, Alfred-Wegener-Institut Bremerhaven, Bremen.
- Rudels, B. (1990). Haline convection in the Greenland Sea. *Deep-Sea Research*, 37(9):1491–1511.
- Samelson, R. (1998). Large-scale circulation with locally enhanced vertical mixing. *Journal of Physical Oceanography*, 28(4):712–726.
- Schauer, U. (1995). The release of brine-enriched shelf water from Storfjord into the Norwegian Sea. *Journal of Geophysical Research*, 100(C8):16,015–16,028.
- Schlosser, P., Bönnisch, G., Rhein, M., and Bayer, R. (1991). Reduction of deepwater formation in the Greenland Sea during the 1980s: Evidence from tracer data. *Science*, 251:1054–1056.
- Schott, F., Visbeck, M., and Fischer, J. (1993). Observation of vertical currents and convection in the central Greenland Sea during the winter of 1988–1989. *Journal of Geophysical Research*, 98(C8):14,401–14,421.
- Smethie, Jr., W., Chipman, D., Swift, J., and Koltermann, K. (1988). Chlorofluoromethanes in the Arctic Mediterranean Seas: Evidence for formation of bottom water in the Eurasian Basin and deep-water exchange through Fram Strait. *Deep-Sea Research*, 35(3):347–369.
- Smethie, Jr., W., Ostlund, H., and Loosli, H. (1986). Ventilation of the deep Greenland and Norwegian Seas: Evidence from Krypton-85, Tritium, Carbon-14 and Argon-39. *Deep-Sea Research*, 33(5):675–703.
- Smyth, W., Moum, J., and Caldwell, D. (2001). The efficiency of mixing in turbulent patches: Inferences from direct simulations and microstructure observations. *Journal of Physical Oceanography*, 31(8):1969–1992.
- St. Laurent, L. and Garrett, C. (2002). The role of internal tides in mixing the deep ocean. *Journal of Physical Oceanography*, 32(10):2882–2899.

- St. Laurent, L., Toole, J., and Schmitt, R. (2001). Buoyancy forcing by turbulence above rough topography in the abyssal Brasil Basin. *Journal of Physical Oceanography*, 31(12):3476–3495.
- Stansfield, K., Garrett, C., and Dewey, R. (2001). The probability distribution of the Thorpe displacements within overturns in Juan de Fuca Strait. *Journal of Physical Oceanography*, 31(12):3421–3434.
- Stommel, H. and Arons, A. (1960). On the abyssal circulation of the world ocean. II. An idealized model of the circulation pattern and amplitude in ocean basins. *Deep-Sea Research*, 6:217–233.
- Strass, V., Fahrbach, E., Schauer, U., and Sellmann, L. (1993). Formation of Denmark Strait Overflow Water by mixing in the East Greenland Current. *Journal of Geophysical Research*, 98(C4):6907–6919.
- Sverdrup, H., Johnson, M., and Fleming, R. (1942). *The Oceans*, Chapter XV. The Water Masses and Currents of the Oceans. Prentice–Hall, Inc., Englewood Cliffs, N.J.
- Swift, J. and Aagaard, K. (1981). Seasonal transitions and water mass formation in the Iceland and Greenland Seas. *Deep-Sea Research*, 28A(10):1107–1129.
- Thompson, R. (1980). Efficiency of conversion of kinetic energy to potential energy by a breaking internal gravity wave. *Journal of Geophysical Research*, 85(C11):6631–6635.
- Thorpe, S. (1975). The excitation, dissipation, and interaction of internal waves in the deep ocean. *Journal of Geophysical Research*, 80(3):328–338.
- Thorpe, S. (1977). Turbulence and mixing in a Scottish loch. *Philos. Trans. Roy. Soc. London*, A286:125–181.
- Thorpe, S. (2001). Internal wave reflection and scatter from sloping rough topography. *Journal of Physical Oceanography*, 31(2):537–553.
- Thurnherr, A., Richards, K., German, C., Lane-Serff, G., and Speer, K. (2002). Flow and mixing in the rift valley of the Mid-Atlantic Ridge. *Journal of Physical Oceanography*, 32(6):1763–1778.
- Toole, J. (1996). New data on deep sea turbulence shed light on vertical mixing. *Oceanus*, 39:33–35.
- Toole, J., Ledwell, J., Polzin, K., Schmitt, R., Montgomery, E., St. Laurent, L., and Owens, W. (1997a). The Brasil Basin tracer release experiment. *WOCE Newsletter*, 28:25–28.
- Toole, J., Polzin, K., and Schmitt, R. (1994). Estimates of diapycnal mixing in the abyssal ocean. *Science*, 264:1120–1123.

- Toole, J., Schmitt, R., Polzin, K., and Kunze, E. (1997b). Near-boundary mixing above the flanks of a midlatitude seamount. *Journal of Geophysical Research*, 102(C1):947–959.
- University of Washington (2002). <http://oceanweb.ocean.washington.edu>.
- Visbeck, M., Fischer, J., and F. Schott (1995). Preconditioning the Greenland Sea for deep convection: Ice formation and ice drift. *Journal of Geophysical Research*, 100(C9):18,489–18,502.
- Visbeck, M. and Rhein, M. (2000). Is bottom boundary layer mixing slowly ventilating Greenland Sea Deep Water? *Journal of Physical Oceanography*, 30(1):215–224.
- Vlasenko, V., Stashchuk, N., Hutter, K., and Sabinin, K. (2003). Nonlinear internal waves forced by tides near the critical latitude. *Deep-Sea Research*, I 50:317–338.
- Wadhams, P., Holfort, J., Hansen, E., and Wilkinson, J. (2002). A deep convective chimney in the winter Greenland Sea. *Geophysical Research Letters*, 29(10):76–1–76–4.
- Walker, S., Weiss, R., and Salameh, P. (1999). Histories of the annual mean atmospheric mole fractions for the halocarbons CFC-11, CFC-12, CFC-113, and carbon tetrachloride. *Journal of Geophysical Research*, 105(C6):14,285–14,296.
- Watson, A., Messias, M.-J., Fogelqvist, E., Van Scoy, K., Johannessen, T., Oliver, K., Stevens, D., Rey, F., Tanhua, T., Olsson, K., Carse, F., Simonsen, K., Ledwell, J., Jansen, E., Cooper, D., Kruepke, J., and Guilyardi, E. (1999). Mixing and convection in the Greenland Sea from a tracer-release experiment. *Nature*, 401:902–904.
- Wijesekera, H., Padman, L., Dillon, T., Levine, M., Paulson, C., and Pinkel, R. (1993). The application of internal-wave dissipation models to a region of strong mixing. *Journal of Physical Oceanography*, 23(2):269–286.
- Woodgate, R. and Fahrbach, E. (1999). Benthic storms in the Greenland Sea. *Deep-Sea Research*, I 46(12):2109–2117.
- Woodgate, R., Fahrbach, E., and Rohardt, G. (1999). The structure and transports of the East Greenland Current at 75°N from moored current meters. *Journal of Geophysical Research*, 104(C8):18,059–10,072.
- Wunsch, C. (2002). Moon, tides and climate. *Nature*, 405:743–744.
- Yamazaki, H. and Osborn, T. (1993). Direct estimation of heat flux in a seasonal thermocline. *Journal of Physical Oceanography*, 23:503–516.

## *Acknowledgements*

This thesis was started at the Department of Regional Oceanography of the Institut für Meereskunde Kiel, and completed at the Department of Oceanography at the University Bremen. First of all, I want to thank my advisor, Monika Rhein, for the opportunity to work on such an interesting and challenging topic, and for her support and encouragement throughout all stages of this work. Thanks also to Dirk Olbers for accepting to co-evaluate this thesis.

I am indebted to Gereon Budéus and Eberhard Fahrbach (AWI) for sharing their CTD data from ARKXIV/2, without which this work would not have been possible. Fritz Schott and Jürgen Fischer (IFM Kiel) gave their permission to use their mooring data.

The captain, crew and the scientists on board the *FS Polarstern* created a productive and enjoyable working environment during the expedition ARKXIV/2, and made the extensive LADCP data set possible. Jens Langreder, Peter Roth, and Thomas Neumann provided invaluable technical support for the ADCPs during the expedition; Thomas successfully converted two instruments into one when things looked grim.

My colleagues from both departments supplied advice, discussion and distraction, whichever was needed at the time – thank you all. Marcus Dengler was always happy to discuss mixing matters with me. Special thanks go out to Eric Kunze, who gave valuable advice during a stay as a guest scientist, and encouraged me by his ongoing interest in my work.

Finally, I want to thank Christian Mertens for all his encouragement, scientific feedback, listening, and talking. He also proofread this manuscript; all remaining errors and typos are entirely my own.